

Low Energy Solar Neutrino Analysis of the Salt Phase of the Sudbury Neutrino Observatory

by

Mark Szymon Kos

A thesis submitted to the Department of Physics, Engineering Physics and

Astronomy

in conformity with the requirements for

the degree of Doctor of Philosophy

Queen's University

Kingston, Ontario, Canada

December, 2007

Copyright ©Mark S.Kos, 2007

Abstract

The neutrino fluxes from the neutral current (NC), charged current (CC), and elastic scattering (ES) neutrino interactions in the salt phase of SNO have been extracted. The signals were extracted above an energy threshold of 4MeV, which is the lowest energy threshold at which the neutrino signals have been extracted from SNO to date. To achieve this low energy threshold the internal and external radioactive background signals have also been measured. The ^8B neutrino fluxes for the 4MeV threshold were found to be

$$\begin{aligned}\Phi_{CC} &= 1.60^{+0.04}_{-0.04} \text{ (stat)}^{+0.06}_{-0.06} \text{ (syst)} \times 10^6 \text{ cm}^{-2} \text{ sec}^{-1}, \\ \Phi_{NC} &= 4.84^{+0.16}_{-0.16} \text{ (stat)}^{+0.29}_{-0.32} \text{ (syst)} \times 10^6 \text{ cm}^{-2} \text{ sec}^{-1}, \\ \Phi_{ES} &= 2.75^{+0.23}_{-0.23} \text{ (stat)}^{+0.25}_{-0.26} \text{ (syst)} \times 10^6 \text{ cm}^{-2} \text{ sec}^{-1}.\end{aligned}$$

These results are in agreement with the values published in [1] and the NC flux is in agreement with the standard solar model calculation from [2]. The published fluxes were

$$\begin{aligned}\Phi_{CC} &= 1.68^{+0.06}_{-0.06} \text{ (stat)}^{+0.08}_{-0.09} \text{ (syst)} \times 10^6 \text{ cm}^{-2} \text{ sec}^{-1}, \\ \Phi_{NC} &= 4.94^{+0.21}_{-0.21} \text{ (stat)}^{+0.38}_{-0.34} \text{ (syst)} \times 10^6 \text{ cm}^{-2} \text{ sec}^{-1}, \\ \Phi_{ES} &= 2.35^{+0.22}_{-0.22} \text{ (stat)}^{+0.15}_{-0.15} \text{ (syst)} \times 10^6 \text{ cm}^{-2} \text{ sec}^{-1}.\end{aligned}$$

The uncertainties on the extracted NC and CC fluxes are significantly smaller than on the published values. A comparison of the total uncertainty from flux measurements presented here and those published are given below.

The shape of the CC energy spectrum has also been extracted with the 4MeV energy threshold. The uncertainties on the extracted fluxes are smaller than what was previously published. The CC spectrum gives a measure of the neutrino energy

	uncertainties presented here (%)	uncertainties from [1] (%)
Φ_{CC}	+4.6 -4.4	+5.9 -6.4
Φ_{NC}	+6.8 -7.4	+8.9 -8.2
Φ_{ES}	+12.3 -12.6	+11.3 -11.3

shape distortion due to neutrino oscillations. The uncertainties on the lowest energy bins in the extracted CC spectrum are much larger than the predicted distortion. We are therefore not sensitive to the upturn in the neutrino survival probability at lower energies predicted by neutrino oscillations in the large mixing angle (LMA) region.

Statement of Originality

The work presented in this thesis is the original work of the author except as noted here and where the work of others has been cited in the text.

Chapters one and two are a review of past experimental results and the current status of neutrino oscillation theory.

Chapter three provides a description of the Sudbury Neutrino Observatory detector. The construction of the detector was completed before the author started his doctoral work. While the author did not take part in the development of the calibration sources he has been involved with the deployment of the energy, optical, and neutron calibration sources.

The author did not develop the data selection algorithms described in chapter four however they are used extensively in the author's analysis later in the thesis. The author has calculated the fraction of neutrino data lost due to the data selection routines.

Chapter six compares the radioactive background measurements made by the author with the work of others. The author did not take part in any of the *ex-situ* measurements.

The systematic uncertainties on energy, isotropy, radius, and solar direction described in chapter nine have been calculated by others. The author has used these uncertainties to perturb the signal and background distributions used in the signal extraction.

The rest of the thesis represents the original work of the author.

Acknowledgments

I would like first to thank my advisor, Aksel Hallin, for his patience and guidance over the course of my PhD work. His understanding of all aspects of the analysis is truly amazing. The success of a large part of the analysis described in this thesis is due to his help. The approach to physics analysis that I have learned from him will be valuable throughout my career.

I am also very grateful to Art McDonald. He was a tremendous help in making sure that this thesis was submitted when it was, and did not take any more time than it already has. The great success of the SNO collaboration owes a lot to the leadership that he has provided.

I would like to thank Mark Boulay. Many of the analysis techniques described in this thesis I have learned from him. The advice that he has offered me throughout my graduate work has always been valuable. It was also nice of him to let me stay at his house (for a very reasonable fee) during my time in Los Alamos.

I would also like to thank Kevin Graham, Jose Maneira, and Will Handler. They have helped in many areas of my work and provided many useful discussions. The success of the neutron analysis in salt benefited greatly from their help. Thanks to Peter Skensved, who has always been extremely helpful even when it didn't seem like it.

I would also like to thank my fellow graduate students: Bryan Fulsom for many interesting discussions in the office as well as at the pub, Ryan MacLellan for his help in understanding the energy response of SNO and for being an interesting travel partner to many SNO analysis meetings, Jeff Lidgard for many interesting discussions outside the office and not necessarily about physics, Ryan Martin for many valuable discussions in the office and on the ski slope and providing me with cheap accommo-

dition during the final few months of my thesis, and Alex Wright for always being more than happy to help and share his knowledge of physics.

I would also like to thank fellow collaboration members who have provided me with guidance and have made my time as a graduate student on SNO very enjoyable. I am grateful to Andrew Hime, Mark Chen, George Ewan, Hugh Evans, Joshua Klein, Hamish Leslie, Barry Roberston and many others.

Finally, I would like to thank my parents, Ella and Henry, and my sister Anna, for their love, patience and support. This thesis is dedicated to them.

Contents

Abstract	ii
Statement of Originality	iv
Acknowledgments	v
List of Figures	ix
List of Tables	xii
List of Acronyms and Abbreviations	xiv
Chapter 1 Introduction	1
Chapter 2 Neutrino Oscillation Physics	11
2.1 Neutrino Oscillations	12
2.1.1 Two Neutrino Mixing	13
2.1.2 Matter Oscillations and the MSW Effect	14
2.2 Other Neutrino Oscillation Theories	17
2.2.1 Sterile Neutrino Mixing	19
Chapter 3 The SNO Detector	22
3.1 SNO Detector Design	23
3.1.1 The Photomultiplier Tubes	25
3.2 Electronics and Data Acquisition	27
3.2.1 Generating an Event Trigger	30
3.3 Calibration of SNO	32
Chapter 4 Data Selection and SNO Observables	36
4.1 First Pass Data Selection	37
4.1.1 Flasher Events	37
4.1.2 Neck Events	37

4.1.3	Burst Events	38
4.1.4	Muons and muon followers	38
4.2	Second Pass Data Selection - Higher Order Cuts	39
4.2.1	In-Time Ratio	41
4.3	Results of Data Cleaning Cuts	42
Chapter 5 Neutron Calibration of SNO		46
5.1	The Calibration Sources	49
5.2	Burst Analysis Method for Selecting Neutron Events	53
5.3	Fitting to the Point Source Efficiency Measurements	57
5.4	Systematic Uncertainties and Corrections on the Calibration Data	58
5.5	Determining the Fission Gamma Fraction Above 6.5MeV	68
5.6	Final Neutron Detection Efficiency and Comparisons with Monte-carlo	72
5.7	Cf and AmBe Source Comparisons	74
Chapter 6 Radioactive Backgrounds		80
6.1	Background Measurement Techniques	87
6.2	Other Sources of Background	91
6.3	Fitting for External Backgrounds	95
Chapter 7 The Neutrino Signals in SNO		106
7.1	The Neutral Current Interaction in the Salt Phase of SNO	106
7.2	The Charged Current Interaction in the Salt Phase of SNO	108
7.3	The Elastic Scattering Interaction in the Salt Phase of SNO	112
7.4	Background Signals in the Salt Phase of SNO	112
7.5	Extracting the Neutrino Signals with the SNO Observables	113
7.5.1	Neutrino Signal Distributions	115
7.5.2	The Background Distributions	117
Chapter 8 Extracting the Neutrino Signals		121
8.1	Signal Extraction in the Salt Phase of SNO	123
Chapter 9 Systematic Uncertainties in the Flux Extraction		130
9.1	Energy Systematic Uncertainties	131
9.1.1	Energy Stability Uncertainty	131
9.1.2	Energy Uncertainty from Position Asymmetry	136
9.1.3	^{16}N Source Modeling	141
9.1.4	Other Sources of Energy Uncertainties	141
9.1.5	Summary of Energy Uncertainties	142
9.2	Systematic Uncertainties on the β_{14} Isotropy Parameter	143
9.3	Angular Resolution Systematic Uncertainty	146
9.4	Uncertainties on the Reconstructed Position	149

9.5	Uncertainties on the $\vec{U} \cdot \vec{R}$ Distribution	151
9.6	Monte Carlo Signal Extraction Studies	153
9.7	Extracted ES and CC Spectra	156
9.8	Extracted Neutral Current and Background Events	164
Chapter 10 Physics Interpretation		166
10.1	^8B Energy Shape Constrained Fits	166
10.2	^8B Energy Shape Unconstrained Fit Results	169
10.2.1	CC flux with an Energy Dependent Fiducial Volume	170
10.2.2	Comparison with the Standard Solar Model	172
10.3	The CC Energy Spectrum	173
10.3.1	Fit to the Charge Current Energy Spectrum	174
Chapter 11 Conclusion		178
References		181

List of Figures

1.1	Solar neutrino spectrum	4
2.1	Allowed regions in neutrino oscillation parameter space.	18
2.2	Neutrino survival probability predicted by the MSW effect.	20
2.3	Fit to SNO and Super-Kamiokande spectra with a sterile neutrino.	21
3.1	Acrylic sphere and suspension ropes.	24
3.2	Photomultiplier support structure and acrylic vessel	26
3.3	Phototube and reflector	28
3.4	SNO electronics	29
3.5	Timing cycle	31
3.6	Calibration source deployment	35
4.1	PMT time distribution	41
4.2	Results of data cleaning	43
4.3	Signal loss	44
5.1	Shown are neutron energy spectra for pure D_2O (red) and salt (blue) running periods. The vertical line represents the energy threshold for the published salt papers.	48
5.2	Drawing of the ^{252}Cf source geometry.	50
5.3	Diagram showing the neutron selection process of the 'Burst cut' used for the ^{252}Cf source in salt. The open circles labeled as events that are not tagged are due to random events from pileup of neutron bursts and from the decay of the fission daughter products.	54
5.4	Energy vs. reconstructed event radius for raw ^{252}Cf data (left panel) and the data after the 'burst cut' has been applied.	55
5.5	Shown are neutron capture efficiency vs radius curves for pure D_2O (red) and salt phase (blue) running periods.	58
5.6	Comparison of Cf monte-carlo, and the Cf data radial distributions. Included are the curves for radial shifts of $\pm 1\%$	61
5.7	Combined Cf data set fitted to the empirical model between 0 and 500cm, and to a 4^{th} order polynomial between 500 and 600cm.	62
5.8	Fit to the raw Cf energy spectrum	70
5.9	Components of the raw Cf energy spectrum	71

5.10	Comparison of neutron detection efficiency for Monte-carlo simulated NC events (data points) and that derived from ^{252}Cf calibration data (shaded band) as a function of volume weighted radius, ρ	73
5.11	Schematic of the burst timing cut used on AmBe data.	74
5.12	Energy versus radius for raw AmBe data	75
5.13	Energy versus radius for clean AmBe data	76
5.14	Neutron energy distributions from various calibration sources.	77
5.15	Comparison of AmBe, Cf, and Monte-carlo neutron distributions	78
5.16	Neutron radial distributions of Monte-carlo and data	79
6.1	Uranium and thorium levels in the the heavy water as a function of time for the salt phase running period	82
6.2	Radioactive chain of ^{238}U . The background that SNO is particularly sensitive to comes from the ^{214}Bi β decay.	85
6.3	Radioactive chain of ^{232}Th . The background that SNO is particularly sensitive to comes from the ^{208}Tl β decay.	86
6.4	Neutrino signals and external backgrounds	90
6.5	Comparison of the radial distribution (panel a) and energy distribution (panel b) of the AV neutrons to the neutrino signals and backgrounds.	97
6.6	Comparisons of energy and radial distributions between the AV neutron Monte-carlo and ^{252}Cf data	99
6.7	β_{14} distributions of the ^{214}Bi and ^{208}Tl H_2O backgrounds compared to the PMT $\beta - \gamma$ background.	101
6.8	Schematic of the Cherenkov light cone for a misreconstructed event.	102
6.9	The β_{14} tail distributions for the external backgrounds.	103
6.10	Radial distributions of the external backgrounds for events that have a high β_{14} value.	104
7.1	CC cross sections for 5, 10, and 15 MeV neutrinos	109
7.2	Energy spectrum of CC events in SNO for an undistorted ^8B spectrum and the spectrum with MSW oscillations.	111
7.3	Distributions of the neutrino signals.	116
7.4	Internal background distributions	117
7.5	External background distributions	118
7.6	The $\vec{U} \cdot \vec{R}$ distributions for the external backgrounds	120
8.1	Energy versus radius for neutrino data	122
8.2	Ratio of Cherenkov background uncertainty to CC signal.	123
8.3	Two-dimensional PDFs used in the signal extraction	124
9.1	Mean of the $N_{corrected}$ distributions for Monte-carlo and ^{16}N data as a function of date.	133
9.2	Mean energy of ^{16}N source calibration runs and ^{16}N source source Monte-carlo.	135
9.3	^{16}N source energy as a function of source radius.	137

9.4	Ratio of ^{16}N data to ^{16}N Monte-carlo energy.	138
9.5	The X and Z coordinates of ^{16}N source deployment positions.	139
9.6	Comparison of the β_{14} parameter between ^{252}Cf data and Monte-carlo.	144
9.7	Comparison of the β_{14} parameter between ^{16}N data and Monte-carlo.	145
9.8	Comparison of the angular resolution distributions for ^{16}N data and Monte-carlo.	147
9.9	Comparison of the reconstructed Monte-carlo and data x, y, and z positions	150
9.10	z position offsets as a function of run number.	152
9.11	Extracted ES and CC spectra from Monte carlo data sets	154
9.12	The fitted energy, β_{14} , and $\cos\theta_{sun}$ distributions to the Monte carlo data.	155
9.13	Extracted CC spectra for various fiducial radii	157
9.14	Extracted ES spectra for various fiducial radii	158
9.15	Data fitted to the neutrino and background signals	159
10.1	Electron neutrino survival probability with non standard interactions	174
10.2	CC energy spectrum down to 4MeV	177

List of Tables

1.1	Nuclear reactions in the proton-proton fusion chain	3
1.2	Nuclear reactions in the carbon-nitrogen-oxygen cycle	3
1.3	Results from neutrino experiments	6
3.1	Calibration sources used in SNO	34
4.1	Signal loss.	45
5.1	Results of the various methods for determining the ^{252}Cf source strength. The source strength is determined for June 12, 2001.	52
5.2	Corrections applied to the neutron efficiency measurement from the data.	64
5.3	Systematic uncertainties on the neutron efficiency measurement from the calibration data. The uncertainties are presented as relative un- certainties.	64
5.4	^{252}Cf run positions with their respective efficiencies for the first part of the salt phase. The source position uncertainty refers to the uncer- tainty on the neutron detection efficiency due to a shift in the source position. We notice from figure 5.5 that the detection efficiency changes very rapidly with radius for source positions near 600cm. This explains why the efficiency uncertainty due to source position uncertainty in- creases with radius.	65
5.5	^{252}Cf run positions with their respective efficiencies for the 28000 series of runs.	66
5.6	^{252}Cf run positions with their respective efficiencies for the 31000 series of runs.	67
5.7	Gamma fractions determined for various D_2O energy scale shifts. . .	69
5.8	Parameter correlation coefficients.	70
5.9	Monte-carlo and data efficiency results and comparisons.	72
6.1	Neutron capture efficiency at the AV.	94
6.2	Number of fitted external AV neutrons.	98
6.3	Extracted number of external background events after fitting in the β_{14} tail region.	105
7.1	γ -ray energies from the reaction $^{35}\text{Cl}(n,\gamma)$	108
9.1	Ratio of data to Monte-carlo energies for ^{16}N source runs at centre. .	135
9.2	Standard deviations of the ^{16}N source mean energies	140

9.3	Standard deviations of the ^{16}N source energy widths	140
9.4	Contributions to the total energy scale uncertainty.	142
9.5	Contributions to the total energy resolution uncertainty.	142
9.6	Systematic uncertainties on the β_{14} parameter.	145
9.7	Uncertainties on the angular resolution function parameters.	148
9.8	Extracted number of CC events for an ES and CC unconstrained fit out to 476cm.	160
9.9	Extracted number of ES events for an ES and CC unconstrained fit out to 476cm.	161
9.10	Extracted number of CC events for an ES and CC unconstrained fit out to 550cm.	162
9.11	Extracted number of ES events for an ES and CC unconstrained fit out to 550cm.	163
9.12	Extracted number of NC and background events for an ES and CC unconstrained fit out to 476cm.	164
9.13	Extracted number of NC and background events for an ES and CC unconstrained fit out to 550cm.	165
10.1	Extracted number of neutrino events from a constrained fit.	168
10.2	Extracted number of neutrino events from a constrained fit.	168
10.3	Absolute fluxes for the three neutrino signals.	168
10.4	Extracted number of neutrino events from an unconstrained fit.	169
10.5	Absolute fluxes for the three neutrino signals.	170
10.6	Absolute fluxes for the three neutrino signals.	170
10.7	Energy dependent fiducial volume regions.	171
10.8	Uncertainties on the neutrino fluxes.	172
10.9	Uncertainties on the CC/NC flux ratios.	172

List of Acryonyms and Abbreviations

ADC	Analog to digital converter
ASIC	Application specific integrated circuit
AV	Acrylic vessel containing the D ₂ O
bkg	background
BUTT	Berkeley underwater test photomultiplier tubes
CC	Charged current
CNO	Carbon-nitrogen-oxygen nuclear fusion cycle
DAMN	Data Analysis Mask Number used in SNOMAN data reduction
d.o.f.	degrees of freedom used in χ^2 calculation
EGS	Electron-gamma shower particle transport code
ES	Elastic scattering (of neutrinos from electrons)
FEC	Front-end card
FORTRAN	Formula translation programming language
GEANT	Geometry and tracking Monte-Carlo system
GTID	Global trigger identification number
INCO	International Nickel Company
MC	Monte-Carlo calculation
MSW	Mikheyev-Smirnov-Wolfenstein matter-enhanced ν oscillations
NC	Neutral current
NECK tubes	Four PMTs in the AV neck
NHITs	Number of hit phototubes
OWL	Outward looking phototube
PDF	Probability distribution function
p.e.	photo-electron
pp	proton-proton solar fusion chain
PMT	Photomultiplier tube
PMTIC	PMT interface card
PSUP	PMT support structure
QSNO	Queen's analysis package for SNO
QUSN7	SNO custom electronics chip
R_{fit}	Reconstructed event radius
RSP	Energy calibration processor in SNOMAN
SNO	Sudbury Neutrino Observatory
SNOD	SNO discriminator chip
SNOINT	SNO charge integrator chip
SNOMAN	SNO Monte-Carlo and analysis software

SNU	Solar neutrino unit (10^{-36} interactions per target per second)
SM	Standard particle physics model
SSM	Standard solar model
TAC	Time to amplitude converter
XSNOED	X-windows based SNO event display
ZDAB	ZEBRA formatted bank for raw SNO data
ZEBRA	CERN's memory management package for FORTRAN

Chapter 1

Introduction

The Sudbury Neutrino Observatory (SNO) is a heavy water (D_2O) Cherenkov detector built to detect solar neutrinos. SNO is located 6800ft below the ground in an active nickel mine in Sudbury Ontario, Canada. The detector consists of one kilotonne of heavy water in an acrylic sphere surrounded by light water (H_2O) which is instrumented by nearly 10000 photomultiplier tubes (PMTs) to detect the resulting light from the neutrino interactions. The light water shields against external neutrons, radioactivity in the PMTs and from the rest of the cavity. The deep underground location helps to shield against cosmic ray background, especially cosmic ray induced muons.

Only electron type neutrinos are generated in the sun. The neutrinos are produced in the fusion reactions in the sun or in the β^+ decay of the fusion daughter products. Table 1.1 shows the reactions in the proton-proton fusion chain in the sun that produce neutrinos and the corresponding neutrino energy. SNO is only sensitive to the 8B and hep neutrinos. Table 1.2 shows the reactions in the carbon-nitrogen-oxygen chain. The neutrino fluxes are calculated according to the standard solar

model (SSM). The SSM is a collection of models that describe how the sun works. The primary goal of the SSM is to model the energy generation and transport in the sun. The SSM should be a solution to an evolutionary equation that satisfies boundary conditions. Constraints on the SSM are a fixed mass, a total luminosity, a fixed outer radius, and an elapsed time that corresponds to the age of the sun, 4.6×10^9 yr. The initial chemical composition and entropy are put in and the SSM is applied numerically to return the conditions of the sun at the present time. The major input parameters and input functions to the SSM are nuclear parameters, solar luminosity, solar age, equation of state, elemental abundances, and radiative opacity. The nuclear parameters involve the fusion reactions in the sun. These are summarized in tables 1.1 and 1.2. The most important of the nuclear parameters are the fusion reaction cross-sections. The elemental abundances affect the radiative opacity which in turn affects the temperature-density profile of the sun. The energy transport due to photon radiation is dependent on the radiative opacity. Photon radiation is the primary mechanism for energy transport in the central regions of the sun. This is particularly important in determining the neutrino flux since neutrinos are generated in the central region of the sun. The equation of state gives a relation between the pressure and density. The values returned by the SSM are the mass fractions of hydrogen, helium and the heavier elements, the spectrum of acoustic oscillation frequencies at the surface of the sun, and most importantly, the neutrino fluxes. A strong test of the SSM is its ability to predict p and s-mode vibrations near the surface of the sun. The p and s-mode vibrations are sensitive to the input parameters and there is little room to adjust the input parameters while still agreeing with the p and s-mode observations [3].

The neutrino fluxes resulting from the various reactions are shown in figure 1.1

Reaction	ν energy (MeV)
$p + p \rightarrow {}^2\text{H} + e^+ + \nu_e$ (pp)	≤ 0.424
or	
$p + e^- + p \rightarrow {}^2\text{H} + \nu_e$ (pep)	1.422
${}^2\text{H} + p \rightarrow {}^3\text{He} + \gamma$	
${}^3\text{He} + {}^3\text{He} \rightarrow \alpha + 2p$	
or	
${}^3\text{He} + {}^4\text{He} \rightarrow {}^7\text{Be} + \gamma$	
${}^7\text{Be} + e^- \rightarrow {}^7\text{Li} + \nu_e$	(90%) 0.861 (10%) 0.383
${}^7\text{Li} + p \rightarrow 2\alpha$	
or	
${}^7\text{Be} + p \rightarrow {}^8\text{B} + \gamma$	
${}^8\text{B} \rightarrow {}^8\text{Be}^* + e^+ + \nu_e$	< 15
${}^8\text{Be}^* \rightarrow 2\alpha$	
or	
${}^3\text{He} + p \rightarrow {}^4\text{He} + e^+ + \nu_e$ (hep)	≤ 18.77

Table 1.1: Nuclear reactions in the proton-proton (pp) chain. The corresponding neutrino energies are also shown. Results are taken from [3].

Reaction	ν energy (MeV)
${}^{12}\text{C} + p \rightarrow {}^{13}\text{N} + \gamma$	
${}^{13}\text{N} \rightarrow {}^{13}\text{C} + e^+ + \nu_e$	≤ 1.199
${}^{13}\text{C} + p \rightarrow {}^{14}\text{N} + \gamma$	
${}^{14}\text{N} + p \rightarrow {}^{15}\text{O} + \gamma$	
${}^{15}\text{O} \rightarrow {}^{15}\text{N} + e^+ + \nu_e$	≤ 1.732
${}^{15}\text{N} + p \rightarrow {}^{12}\text{C} + \alpha$	

Table 1.2: Nuclear reactions in the carbon-nitrogen-oxygen (CNO) cycle. The corresponding neutrino energies are also shown. Results are taken from [3].

as calculated by the SSM. What are shown are the fluxes from the various reactions as a function of neutrino energy. It is evident that most of the neutrino flux from the sun is from the pp reaction. In fact, almost 91% of the neutrino flux is from the pp reaction and less than 0.01% is from the ^8B reaction that SNO is sensitive to.

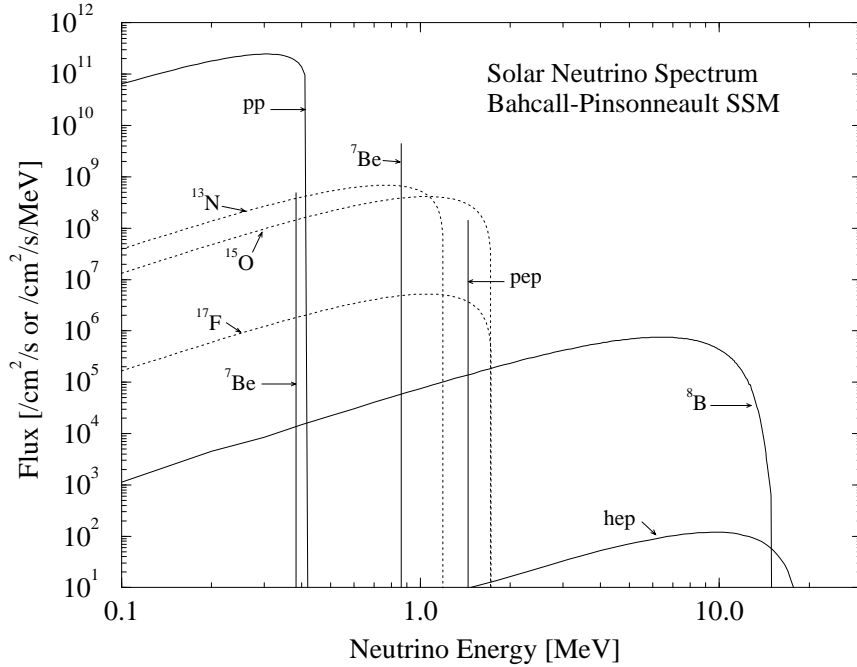


Figure 1.1: Solar neutrino spectra predicted by the Bahcall-Pinsonneault standard solar model. The fluxes from the continuum sources like pp for example are in units of cm^2 per s per MeV, while the line sources are in units of cm^2 per s. The dashed curves are for the CNO reactions. Figure taken from [3].

SNO was built to solve two long standing problems in neutrino and solar physics. In the earlier solar neutrino experiments the number of detected neutrinos was much smaller than the number expected from the sun. The issue then arose whether the solar model that predicts the number of neutrinos from the sun was wrong, or if neutrinos experience a flavour change as they travel from the sun to the earth. Since earlier neutrino experiments only detected electron type neutrinos flavour change could explain the observed deficit.

The earliest solar neutrino experiments detected neutrinos through radiochemical processes. The first and probably most important of the initial experiments is the ^{37}Cl experiment conceived by Ray Davis Jr. which was located deep underground in Homestake gold mine in South Dakota. The ^{37}Cl experiment detected neutrinos through the reaction



The Homestake experiment, which began taking data in 1968, consisted of a 10000 gallon tank of C_2Cl_4 . The ^{37}Ar was extracted chemically from C_2Cl_4 . The extraction process was done every few months for a period of about 15 years. The typical number of extracted ^{37}Ar atoms was 15, an amazing achievement considering there were about 10^{30} atoms in the tank. After subtracting the predicted background due to cosmic rays the measured solar neutrino flux from the ^{37}Cl experiment is $(2.56 \pm 0.16)\text{SNU}$ [4]. The SNU (Solar Neutrino Unit) is a unit of neutrino flux defined as the product of the neutrino flux with a theoretical cross section for neutrino absorption. A SNU is then defined to be 10^{-36}s^{-1} . The total predicted neutrino flux that the ^{37}Cl experiment should observe, which cannot detect neutrinos from the pp reaction since $\nu_e + {}^{37}\text{Cl} \rightarrow e^- + {}^{37}\text{Ar}$ has a threshold of 0.814MeV, is 7.9SNU [3]. This discrepancy is the beginning of the solar neutrino problem. Experiments that followed the Homestake experiment also saw similar deficits in the observed number of neutrinos compared to the SSM prediction. Table 1.3 compares the various solar neutrino experiments to the SSM prediction. For all the experiments the results differ from the SSM prediction to a very high degree of statistical significance.

As one can imagine, a substantial effort has gone into explaining the deficit in the observed number of solar neutrinos. If it is assumed that the SSM prediction is correct, then the cause of the deficit has to be in the nature of neutrinos themselves.

Experiment	Reaction	SSM	measured/SSM
Homestake	$\nu_e + {}^{37}\text{Cl} \rightarrow e^- + {}^{37}\text{Ar}$	$7.6^{+1.3}_{-1.1}$	0.34 ± 0.06
GALLEX + GNO	$\nu_e + {}^{71}\text{Ga} \rightarrow e^+ + {}^{71}\text{Ge}$	128^{+9}_{-7}	0.58 ± 0.07
SAGE	$\nu_e + {}^{71}\text{Ga} \rightarrow e^+ + {}^{71}\text{Ge}$	128^{+9}_{-7}	0.59 ± 0.07
Kamiokande	$\nu_e + e \rightarrow \nu_e + e$	$5.05^{+1.01}_{-0.81}$	0.55 ± 0.13
Super-Kamiokande	$\nu_e + e \rightarrow \nu_e + e$	$5.05^{+1.01}_{-0.81}$	0.48 ± 0.09

Table 1.3: Summary of neutrino experiments and their comparisons to the SSM. Also shown are the SSM predictions for the various experiments. The values quoted are in terms of solar neutrino units (SNU). This table is adapted from [5].

The most widely accepted theory is that of neutrino flavour oscillations. Neutrino oscillations were first proposed by Bruno Pontecorvo in 1957 [6] and developed further by Bilenky and Pontecorvo [7]. The oscillation theory was developed further to include oscillations in matter by Wolfenstein [8] and then by Mikheyev and Smirnov [9]. Neutrino flavour oscillations arise from the assumption that the neutrino flavour states are different than the neutrino mass eigenstates. In general we can then write

$$|\nu_e\rangle = \cos\theta|\nu_1\rangle + \sin\theta|\nu_2\rangle \quad (1-2.a)$$

$$|\nu_f\rangle = -\sin\theta|\nu_1\rangle + \cos\theta|\nu_2\rangle \quad (1-2.b)$$

where

$|\nu_e\rangle$ is the electron neutrino flavour eigenstate,

$|\nu_f\rangle$ is a different flavour eigenstate,

$|\nu_1\rangle, |\nu_2\rangle$ are mass eigenstates with masses m_1 & m_2 , and

θ is the mixing angle.

Since the flavour eigenstates are not eigenstates of the Hamiltonian, \mathcal{H} , the neutrino flavour states will go through quantum mechanical oscillations. At some later time t

the neutrino flavour eigenstate will be

$$|\nu(t)\rangle = e^{-iE_1 t} \cos \theta |\nu_1\rangle + e^{-iE_2 t} \sin \theta |\nu_2\rangle \quad (1-3.a)$$

$$= c_e(t) |\nu_e\rangle + c_f(t) |\nu_f\rangle, \quad (1-3.b)$$

where

E_1, E_2 are the energies of the mass eigenstates, and

$c_e(t), c_f(t)$ are the probability amplitudes of the electron and non-electron flavour eigenstates respectively at some later time t .

Since the solar neutrino detectors prior to SNO were only sensitive to electron type neutrinos at the solar neutrino energies, an oscillation of the electron flavour neutrino into a different flavour would result in an observed deficit in the neutrino flux. The neutrino oscillation theory is developed in more detail in chapter 2.

The Super-Kamiokande experiment, located in Kamioka, Japan, is the most recent Cherenkov detector before SNO. It consists of a large cylinder of light water surrounded by PMTs. It has about 50 times the volume of SNO. While Super-Kamiokande also sees a deficit in the expected number of solar neutrino, they also see evidence that neutrinos oscillate from one flavour to another from their atmospheric neutrino measurement. The Super-Kamiokande collaboration have measured the atmospheric neutrino flux as a function of zenith angle and has found a deficit in the muon type neutrino flux for the zenith angle region corresponding to events that are going through the earth. Their result is inconsistent with the no neutrino oscillation hypothesis to a very high degree of confidence [10].

The use of heavy water has allowed SNO to directly measure neutrino flavour transformation in solar neutrinos. Through the use of heavy water SNO is able to

both detect electron type neutrinos exclusively and also to measure the total flux of all flavours of neutrinos. The three neutrino interactions that take place in SNO are,

$$\nu_e + {}^2\text{H} \longrightarrow p + p + e^- \quad (1-4)$$

$$\nu_x + {}^2\text{H} \longrightarrow \nu_x + p + n \quad (1-5)$$

$$\nu_x + e^- \longrightarrow \nu_x + e^- \quad (1-6)$$

where ν_x refers to any of the active neutrino flavours. The threshold of equation 1-4, the charged current (CC) neutrino interaction is 1.4MeV, and the threshold for the neutral current (NC) interaction (equation 1-5) is 2.2MeV. The threshold for these reactions means that SNO is only sensitive to the ${}^8\text{B}$ and the hep neutrinos. The elastic scattering (ES) interaction (equation 1-6) is sensitive to all neutrino flavours but with a ~ 7 times greater sensitivity to electron type neutrinos over the other flavours. The Super Kamiokande experiment has also measured the ES interaction and their result is much more statistically precise than the SNO ES result due to their much larger volume. For the first results published by the SNO collaboration [11] the SNO CC neutrino flux was compared with Super Kamiokande ES measurement. This comparison resulted in the first measurement of solar neutrino flavour change. Since the CC interaction is only sensitive to electron flavour neutrinos and the NC interaction is sensitive to all flavours, a comparison of the fluxes measured through the CC and NC interactions would give direct evidence for neutrino flavour transformation. The later SNO results ([12], [13], and [1]) of the CC and NC neutrino fluxes have confirmed both the SSM prediction for the ${}^8\text{B}$ neutrino flux and that neutrino flavour change occurs.

There are three phases to the SNO experiment. The first phase was the pure D_2O phase where nothing was added to the D_2O volume. The pure D_2O phase started

taking data in November of 1999. Although the CC flux was measured with good sensitivity in the pure D₂O phase, the neutron capture efficiency with D₂O alone above the analysis threshold is only 14%. Therefore the number of detected NC events measured in the pure D₂O phase was about a third of the measured number of CC events. In the next phase of SNO salt (NaCl) was dissolved into the D₂O. While the salt concentration was only 0.2% by weight, ³⁵Cl has a much higher neutron capture cross section than ²H. Therefore the sensitivity to the NC interaction was actually increased by a factor of three in the salt phase. The neutron detection efficiency measurement for the salt phase is largely my work and is described in detail in this thesis. In the third phase the salt was removed and neutral current detectors (NCDs) were put in the D₂O. These consist of forty tubes filled with ³He that run from the bottom to the top of the D₂O volume. The NCDs are only sensitive to the NC interaction and offer a NC measurement that is independent of the CC and ES data. The analysis of the NCD phase data is still in progress.

The work presented in this thesis is on the analysis of the salt phase data. The results from the salt phase data have already been published with a neutrino energy threshold of 5.5MeV [13], [1]. The flux results for the three neutrino interactions in SNO were,

$$\begin{aligned}\Phi_{CC} &= 1.68^{+0.06}_{-0.06} \text{ (stat)}^{+0.08}_{-0.09} \text{ (syst)} \times 10^6 \text{cm}^{-2} \text{sec}^{-1}, \\ \Phi_{ES} &= 2.35^{+0.22}_{-0.22} \text{ (stat)}^{+0.15}_{-0.15} \text{ (syst)} \times 10^6 \text{cm}^{-2} \text{sec}^{-1}, \\ \Phi_{NC} &= 4.94^{+0.21}_{-0.21} \text{ (stat)}^{+0.38}_{-0.34} \text{ (syst)} \times 10^6 \text{cm}^{-2} \text{sec}^{-1}.\end{aligned}$$

These CC and ES results are in agreement with previous solar neutrino experiments, and the NC result is in agreement with the SSM calculation for the total ⁸B neutrino

flux.

Chapter 2

Neutrino Oscillation Physics

The interaction of neutrinos with matter is well understood and is explained by the weak interaction in the standard electroweak model. Through the exchange of W or Z bosons neutrinos can interact with other particles, primarily electrons and quarks, in what is described as a vector – axial vector interaction. The standard electroweak model has been confirmed by experimental data. In the standard electroweak model there are three flavours of neutrinos, ν_e , ν_μ , and ν_τ . These correspond to the three charged leptons e , μ , and τ . The sun can only produce electron flavour neutrinos. Since SNO confirms the SSM prediction of the ^8B neutrino flux with its NC measurement (which is sensitive to all neutrino flavours) and sees about a third of the expected neutrino flux with the CC measurement (which is only sensitive to electron type neutrinos) the solar neutrinos must be going through a flavour change on the way to the earth.

2.1 Neutrino Oscillations

The agreed upon theory for neutrino flavour change is that neutrinos oscillate from one flavour state to another. In neutrino oscillation theory neutrino oscillations can occur in a vacuum and in matter. Matter oscillations, explained by the MSW effect, will be described later in this chapter. We will begin by looking at neutrino vacuum oscillations. Following the description outlined in [3], we will denote the flavour eigenstates corresponding to ν_e , ν_μ , and ν_τ with Greek subscripts, $|\nu_\alpha\rangle$ for example. The mass eigenstates will be denoted with numerical subscripts, $|\nu_1\rangle$, $|\nu_2\rangle$, and so on. At any time we assume that the neutrino is in a superposition of the three flavour eigenstates,

$$|\nu\rangle = A_e|\nu_e\rangle + A_\mu|\nu_\mu\rangle + A_\tau|\nu_\tau\rangle. \quad (2-1)$$

The neutrino mass eigenstates satisfy the Schroedinger equation

$$\mathcal{H}|\nu_j\rangle = E_j|\nu_j\rangle_{j=1,2,3} \quad (2-2)$$

where E_j are the energies of the mass eigenstates. In general, the mass eigenstates of the Hamiltonian, $|\nu_j\rangle$, are not the same as the flavour eigenstates, $|\nu_\alpha\rangle$. There must then be some linear unitary transformation matrix, U , that relates the flavour basis to the mass basis. The neutrino state at some future time t can thus be expressed in terms of the mass eigenstates,

$$|\nu_\alpha\rangle_t = U_{\alpha j}e^{-iE_j t}|\nu_j\rangle \quad (2-3)$$

where $e^{-iE_j t}$ is the time varying Hamiltonian.

2.1.1 Two Neutrino Mixing

The simplest way to understand neutrino oscillations is through the case of the solution of two neutrino mixing. Also, for solar neutrinos most of the mixing is assumed to be between ν_1 and ν_2 . For the two neutrino case the transformation matrix U is

$$U = \begin{pmatrix} \cos \theta_v & \sin \theta_v \\ -\sin \theta_v & \cos \theta_v \end{pmatrix} \quad (2-4)$$

with θ_v being the vacuum mixing angle. We can then express the time evolution of the ν_e state as:

$$|\nu_e\rangle_t = \cos \theta_v e^{-iE_1 t} |\nu_1\rangle + \sin \theta_v e^{-iE_2 t} |\nu_2\rangle. \quad (2-5)$$

The probability for a ν_e to remain a ν_e is

$$|\langle \nu_e | \nu_e \rangle_t|^2 = 1 - \sin^2(2\theta_v) \sin^2\left(\frac{(E_2 - E_1)t}{2}\right). \quad (2-6)$$

For relativistic neutrinos we have that the square of the energy is equal to the sum of the square of the momentum and the square of the mass,

$$E^2 = p^2 + m^2, \quad (2-7)$$

$$E = p \sqrt{1 + \frac{m^2}{p^2}}. \quad (2-8)$$

Since the neutrino momentum is much larger than the neutrino mass we use the Taylor expansion to get

$$E \cong p + \frac{m^2}{2p} \quad (2-9)$$

If momentum is conserved, and the momentum of both the neutrino mass eigenstates are the same, then we have,

$$E_2 - E_1 = \frac{m_2^2 - m_1^2}{2E}. \quad (2-10)$$

The neutrino survival probability is then

$$P(\nu_e \rightarrow \nu_e, t) = |\langle \nu_e | \nu_e \rangle|^2 \quad (2-11.a)$$

$$= 1 - \sin^2(2\theta) \sin^2\left(\frac{\Delta m^2 t}{4E}\right), \quad (2-11.b)$$

with

$$\Delta m^2 = m_2^2 - m_1^2, \quad (2-12.a)$$

$$E = \text{neutrino energy}. \quad (2-12.b)$$

Determining the parameters Δm^2 and $\sin^2(2\theta)$ determines the neutrino survival probability. The parameter $\sin^2(2\theta)$ gives the neutrino oscillation amplitude and is determined by measuring the difference between the total solar neutrino flux as given by the SNO NC measurement and the electron type neutrino flux as given by the CC measurement. The Δm^2 parameter changes the neutrino oscillation frequency. Measuring the energy dependence of the CC flux provides a constraint on the Δm^2 parameter.

2.1.2 Matter Oscillations and the MSW Effect

Electron type neutrinos passing through the sun and the earth can interact with matter via the weak interaction. This interaction effectively changes the potential energy in the Hamiltonian which in turn changes the oscillation amplitude and frequency. The agreed upon theory for neutrino oscillations in matter is known as the MSW effect after its discoverers Mikheyev, Smirnov, and Wolfenstein [9, 8]. Good descriptions of the MSW effect can also be found in [14] and [15]. In the MSW effect a potential energy term that represents the potential from electron type neutrinos

interacting with electrons is added to the Hamiltonian,

$$V = \sqrt{2}G_f N_e, \quad (2-13)$$

where G_f is the Fermi coupling constant and N_e is the local electron number density.

The Hamiltonian for neutrinos passing through matter is given by

$$\mathcal{H} = \begin{pmatrix} \frac{m_1^2 \cos^2 \theta + m_2^2 \sin^2 \theta}{2E} + \sqrt{2}G_F N_e & \frac{\Delta m^2}{2E} \cos \theta \sin \theta \\ \frac{\Delta m^2}{2E} \cos \theta \sin \theta & \frac{m_1^2 \sin^2 \theta + m_2^2 \cos^2 \theta}{2E} \end{pmatrix}, \quad (2-14)$$

where θ is the still the vacuum mixing angle and the subscript v has been dropped.

Maximal mixing occurs when the diagonal elements of the Hamiltonian are degenerate.

It is obvious that with the right choice of electron number density, N_e , this can

occur. If we choose N_e such that

$$\frac{m_1^2 - m_2^2}{2E} \cos 2\theta = -\sqrt{2}G_F N_e \quad (2-15)$$

then the resonance condition is reached. The mixing angle in matter is related to the

vacuum mixing angle by

$$\sin^2 2\theta_m = \frac{\sin^2 2\theta}{\sin^2 2\theta + (l/l_e - \cos^2 \theta)^2} \quad (2-16)$$

where the vacuum oscillation length is

$$l = \frac{4\pi E}{\Delta m^2} \quad (2-17)$$

and the neutrino-electron interaction length is

$$l_e = \frac{2\pi}{\sqrt{2}G_F N_e}. \quad (2-18)$$

We notice that $\sin^2 \theta_m$ has a maximum at $l/l_e = \cos 2\theta$, which corresponds exactly

to the MSW resonance condition found above. The maximal mixing angle is then

obviously $\pi/4$. It is interesting to note that the MSW resonance depends on the energy of the neutrinos. Therefore neutrinos of different energy can have varying degrees of matter oscillation. In the analysis presented in this thesis the CC energy spectrum is measured down to an energy of 4MeV and compared to the spectrum expected from MSW spectral distortion.

Although we now know that the vacuum mixing angle is large, even if the vacuum mixing angle were small the matter mixing angle can still be at a maximum, $\pi/4$, if the neutrino passes through the necessary electron density. From SNO's salt phase neutrino flux measurements [1] the mixing angle is determined to be 33.9 degrees. While this is not maximal mixing, it lies in the large mixing angle (LMA) solution region for neutrino oscillations. The LMA region refers to neutrino oscillation solutions which have a mixing angle θ of around $\pi/6$ up to the maximal mixing angle of $\pi/4$. Different values of $\sin^2 \theta$ and Δm^2 will give different measured flux rates for various neutrino experiments. Therefore by doing a combined fit to various neutrino experiments the allowed solutions for $\sin^2 2\theta$ and Δm^2 can be constrained. Figure 2.1 shows the allowed regions of $\tan^2 \theta$ and Δm^2 space derived from various experiments. Figure 2.1 is taken from [1] and uses the standard convention of plotting $\tan^2 \theta$ instead of $\sin^2 2\theta$. What is shown in panel (a) of figure 2.1 is the allowed region from a combined fit to the SNO salt and pure D₂O phase data, and the other solar neutrino experiments including Homestake, GALLEX, SAGE, and Super-Kamiokande. The bottom panel, panel (b), shows the combined fit when the KamLAND result is included. KamLAND is a reactor anti-neutrino experiment in Japan. It consists of 1 kilotonne of liquid scintillator and detects anti-neutrinos from 53 nuclear reactors in the surrounding area. KamLAND is much more sensitive to Δm^2 than the solar neutrino experiments. We can see this by rewriting equation 2-11 in terms of the

distance the neutrinos travel, L :

$$|\langle \nu_e | \nu_e \rangle|^2 = 1 - \sin^2(2\theta) \sin^2\left(\frac{\Delta m^2 L}{4E}\right). \quad (2-19)$$

The $\sin^2(\frac{\Delta m^2 L}{4E})$ term introduces an overall phase to the oscillation. Since the distance L is fixed for KamLAND the only parameters that can effect the phase are Δm^2 and the energy E . The solar neutrino experiments detect neutrinos after they have gone through matter enhanced oscillations so they are not so sensitive to Δm^2 .

2.2 Other Neutrino Oscillation Theories

Although the MSW effect and in general three neutrino mixing is generally assumed to be the mechanism for neutrino flavour change other theories do exist. Such as mixing with a sterile neutrino [16], or non-standard neutrino interactions [17]. It should also be noted that the MSW effect predicts an upturn in the neutrino survival probability at energies below the SNO published threshold. This upturn has not yet been observed. However, SNO and Super-Kamiokande are the only solar neutrino detectors that are currently able to measure neutrino energy and with their energy thresholds and uncertainties the predicted upturn would be hard to detect. Figure 2.2 shows the electron neutrino survival probability as a function of neutrino energy as predicted by the LMA solution to the MSW effect. The SNO energy response is included in the calculation. Since the threshold for the CC interaction to proceed (Q-value) is 1.4MeV, a neutrino energy of 6.9MeV corresponds to the published salt phase data threshold of 5.5MeV. The uncertainty at the published analysis threshold is around 11%. It would be difficult then to observe the predicted upturn in the MSW survival probability at the published energy threshold.

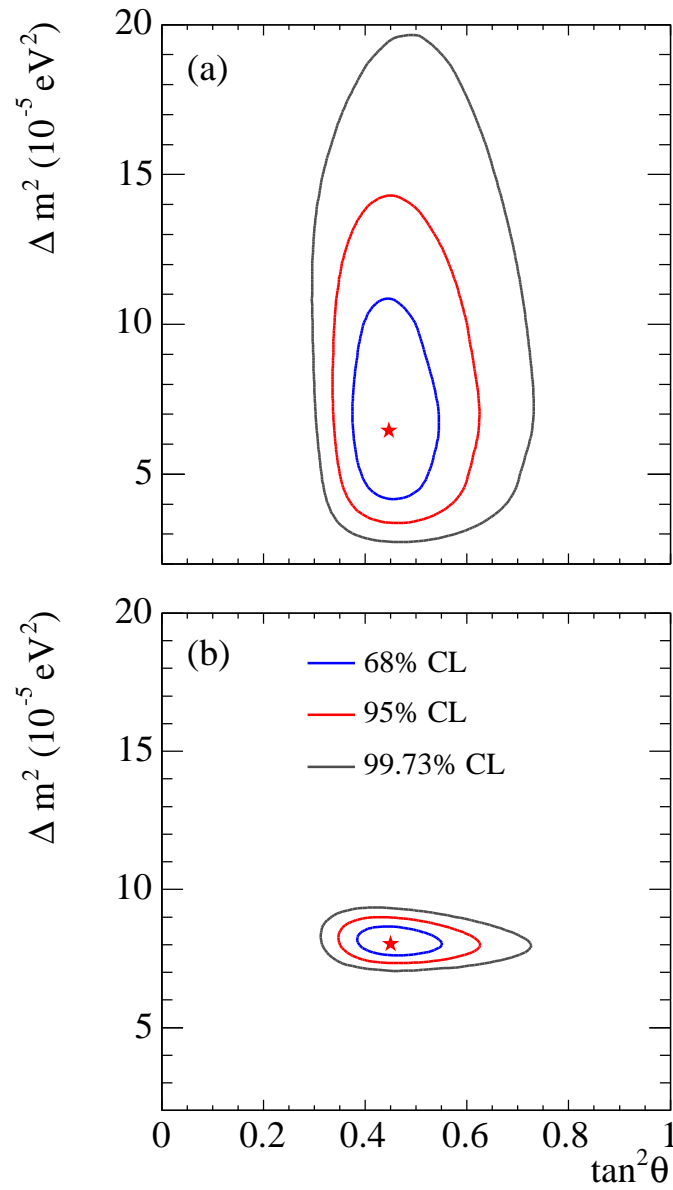


Figure 2.1: Allowed regions in $\tan^2 \theta_m$ and Δm^2 space from a combined fit to all solar neutrino (a) and to the solar data + KamLAND reactor data (b).

2.2.1 Sterile Neutrino Mixing

Several theories attempt to give a mechanism that would suppress the predicted upturn in the survival probability. One possibility is that the active neutrinos can mix to one or more sterile neutrinos. Since the sterile neutrinos do not interact with matter, oscillations of active neutrinos into sterile neutrinos would be seen as a decrease in the survival probability. A possible way to add in sterile neutrinos is to add a second mixing angle, α , that allows the active neutrinos to mix with a sterile neutrino. Adding in a third mass eigenstate, ν_0 , sterile mixing can be described by

$$|\nu_0\rangle = \cos\alpha|\nu_s\rangle + \sin\alpha(\cos\theta|\nu_e\rangle - \sin\theta|\nu_a\rangle), \quad (2-20.a)$$

$$|\nu_1\rangle = \cos\alpha(\cos\theta|\nu_e\rangle - \sin\theta|\nu_a\rangle) - \sin\alpha|\nu_s\rangle, \quad (2-20.b)$$

$$|\nu_2\rangle = \sin\theta|\nu_e\rangle + \cos\theta|\nu_a\rangle \quad (2-20.c)$$

where ν_a represents either ν_μ or ν_τ . It is proposed by [16] that no observed upturn in the ^8B neutrino energy spectrum can be explained by a small mixing angle, $\sin 2\alpha = 10^{-5} - 10^{-3}$, with a light sterile neutrino, $\Delta m_{01}^2 = 0.2 - 2 \times 10^{-5} eV^2$. Figure 2.3 shows a fit to the Super-Kamiokande and SNO spectra using the predicted energy spectrum after introducing a sterile neutrino with a small mixing angle [16]. It is hard to notice any substantial difference in the quality of the fits. The lowest energy bin for the SNO spectrum is 5.5MeV in outgoing electron energy. In the analysis presented in this thesis the SNO energy threshold is extended down to 4MeV in recoil electron energy. The predicted MSW and sterile mixing spectra are then fit to the lower energy threshold data.

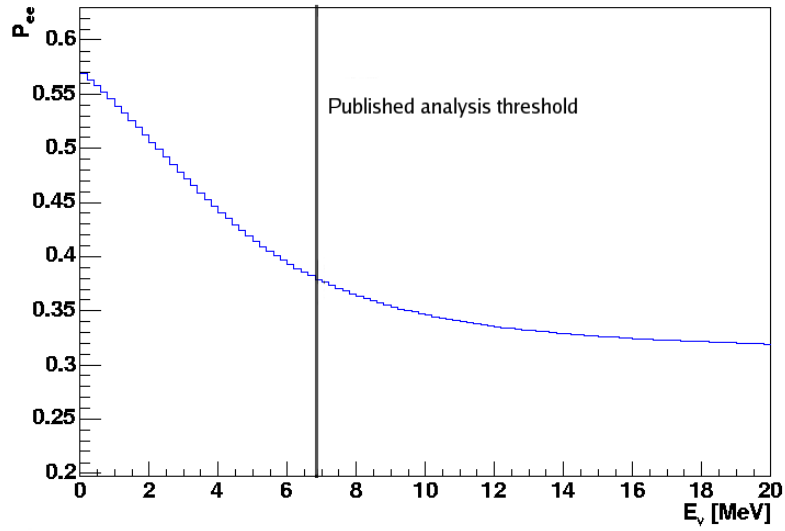


Figure 2.2: Electron neutrino survival probability as a function of neutrino energy as predicted by the MSW effect. An outgoing electron kinetic energy of 5.5MeV (the current published threshold [1]) corresponds to the neutrino energy of 6.9MeV which is indicated in the figure.

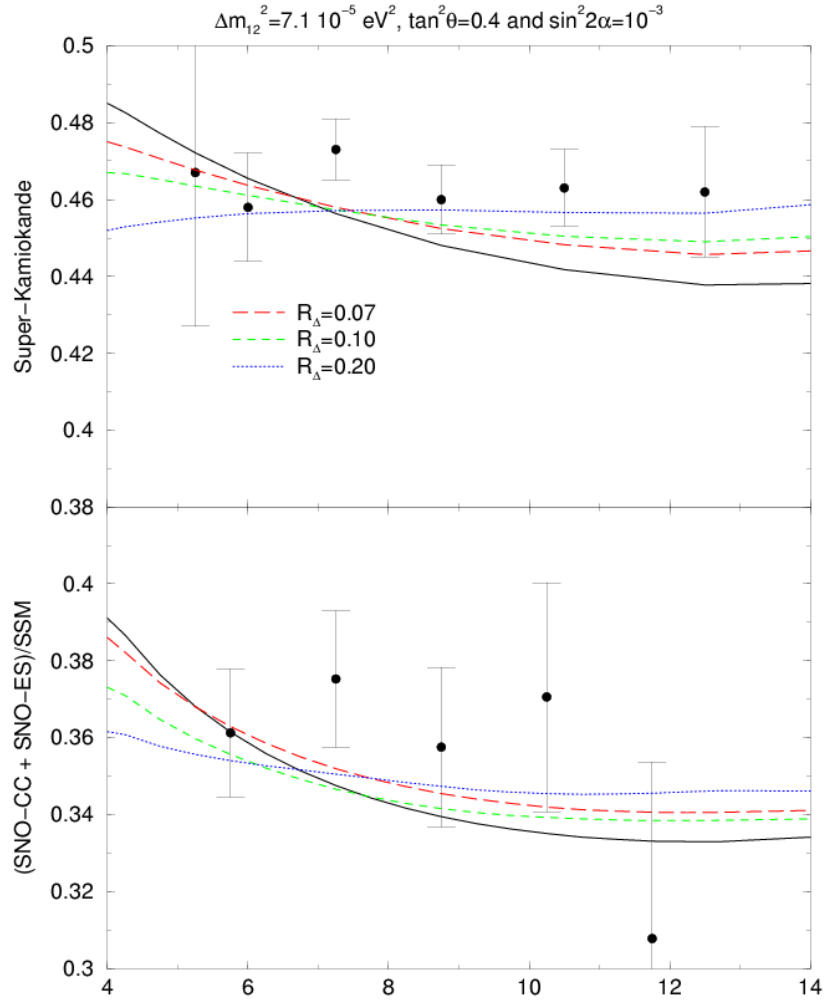


Figure 2.3: Fit to the Super-Kamiokande and SNO energy spectra with the predicted energy spectrum after introducing a small mixing angle with a sterile neutrino. Also shown are fits to the data with the energy spectrum predicted from the MSW effect and with no spectral distortions. $R_{\Delta} = \Delta m_{01}^2 / \Delta m_{21}^2$ is the ratio of the sterile mass squared difference to the active neutrino mass squared difference. The x-axis is outgoing electron kinetic energy in MeV. The figure is taken from [16].

Chapter 3

The SNO Detector

The Sudbury Neutrino Observatory observes all flavours of neutrinos through the detection of the Cherenkov light produced in the charged current (CC), elastic scattering (ES) and neutral current (NC) interactions. These interactions are described by equations 1-4, 1-5, and 1-6. For the CC and ES interactions the outgoing electrons will emit Cherenkov light as they slow down (if they have enough energy). In the NC interaction, the outgoing neutron will most likely capture on ^{35}Cl in the salt phase. The resultant ^{36}Cl is usually produced in an excited state which then de-excites with the emission of γ -rays. These γ -rays can then Compton scatter electrons and the Cherenkov light from these electrons are then detected. The Cherenkov light is detected through the use of an array of 9456 20cm diameter Hamamatsu photomultiplier tubes (PMTs) that look inward on the heavy water volume.

The centre of the SNO detector is at a depth of 2092 meters. Since other underground neutrino detectors have different composition of their rock overburden it is useful to express the depth in terms of meters of water shielding. The SNO depth is estimated then to be at 6000 meters water equivalent. At this depth most of the cos-

mic ray background is eliminated. The only cosmic ray induced particles that make it through are muons and neutrinos. SNO only sees about three muons per hour.

Access to the SNO detector area is done through an elevator car down the main mine shaft with the mining personnel. The detector area is located about two kilometers from the exit point of the shaft. This distance is typically walked. The limited access to the SNO lab area presented a challenge during the construction phase since all material used for construction had to be taken in by elevator car. Heavy equipment and heavy water were transported into the lab area by rail car.

3.1 SNO Detector Design

The SNO heavy water is contained in a spherical volume inside an acrylic vessel (AV). The diameter of the sphere is 12 meters. The acrylic sphere was constructed by bonding together 122 panels of ultraviolet transmitting acrylic. The thickness of the acrylic sphere is 5.5cm in most places. A full technical description of the detector can be found in [18]. To deploy calibration sources, there is an opening at the top of the acrylic which resembles a chimney. The chimney or neck, as it is called by the collaboration, is 1.5 meters in diameter and 6.8 meters high. It is also constructed of acrylic. The acrylic sphere is suspended by ten ropes to the deck. The ropes are connected to the acrylic at the belly of the sphere to rope groove panels that are 11.4cm thick. A diagram of the acrylic sphere and the suspension ropes is shown in figure 3.1.

Since SNO was designed to detect a relatively rare low energy process, the interaction of solar neutrinos, it is important that the radioactive backgrounds be minimized. The acrylic chosen for the AV was measured to contain low concentrations of radioac-

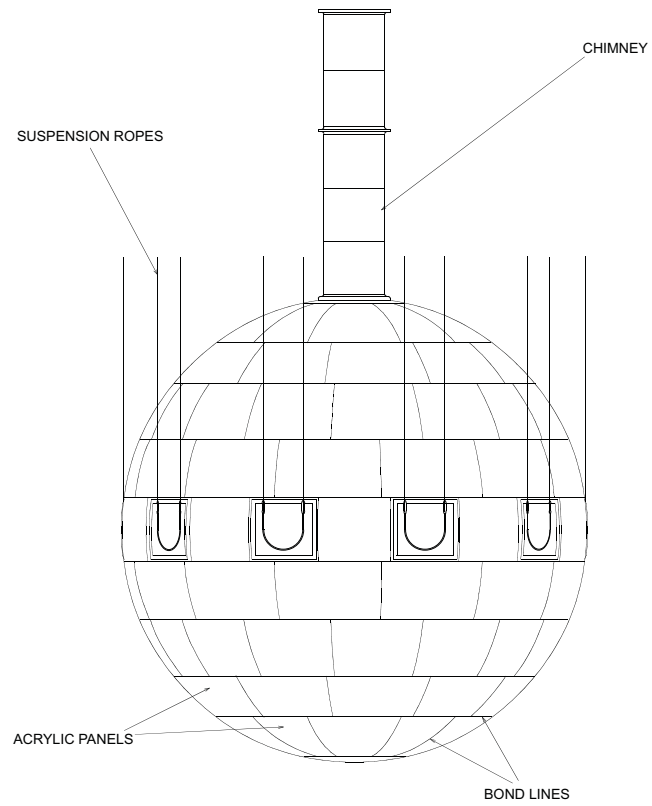


Figure 3.1: Diagram of the acrylic sphere containing the heavy water. The suspension ropes and rope groove panels are also shown.

tivity. The U and Th concentrations were measured to be less than $1.1 \times 10^{-12} \text{g/g}$ in the acrylic. Monte-carlo simulations showed that this was acceptable. The radioactivity limits are set by the requirement that the total neutron background from photo-disintegration is less than one tenth of the SSM prediction.

Surrounding the acrylic sphere there are 9456 PMTs mounted on a stainless steel geodesic sphere. The diameter of the geodesic sphere is 18 meters. The face of the PMTs is at a diameter of 17 meters. Therefore the spacing between the AV wall and the PMTs is 2.5 meters. This geodesic sphere is known as the PMT support structure (PSUP). For radioactive shielding the AV and PSUP are immersed in ultra pure light water. The entire height of the cavity is about 30 meters. To prevent any material from the surrounding rock from entering the ultra pure water the walls of the cavity are covered with a layer of sprayed-on-concrete (Shotcrete) and a urylon plastic liner. Figure 3.2 shows a schematic of the AV surrounded by the PSUP.

3.1.1 The Photomultiplier Tubes

As mentioned previously, there are 9456 inward looking PMTs attached to the PSUP. To veto external background events like muons, there are 91 PMTs facing outwards on the PSUP and 23 PMTs suspended in the external light water (outside the PSUP) looking inward. The radius of PMTs at their widest point is a little over 10cm. The PMTs have to adhere to strict specifications of maximum radioactivity levels. Specifically, the uranium concentration was less than 120ng/g, the thorium concentration was less than 90ng/g, and the potassium concentration was less than 0.2mg/g in the glass. The glass was assayed before the manufacture of the PMTs to ensure that these radioactivity levels were met. Besides low radioactivity, other important properties for the PMTS are that they have a narrow spread in the photo-electron transit time,

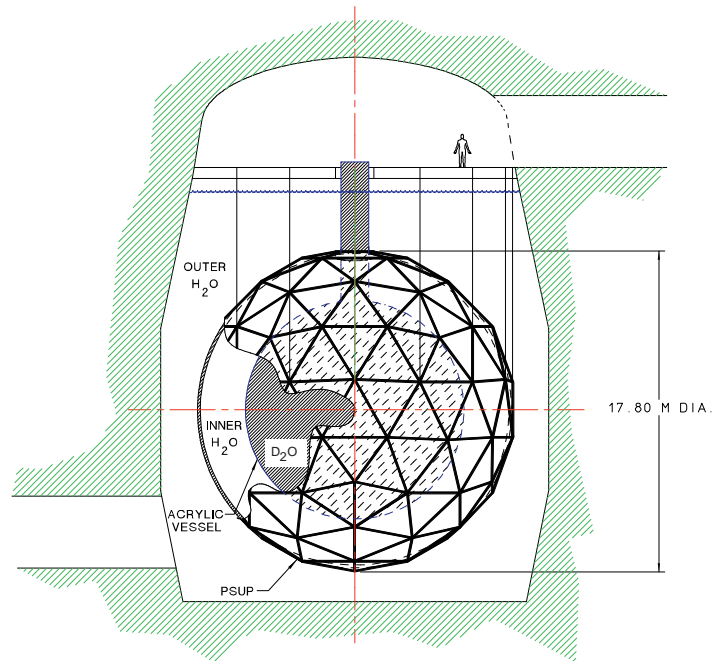


Figure 3.2: PMT support structure surrounding the acrylic vessel. Also shown is the surrounding ultra-pure light water shielding and rock wall of the cavity.

a high photon detection efficiency, and a low noise rate. The spread in the transit time is less than 1.7ns and the noise rate is less than 8kHz at a charge gain of 10^7 . While PMTs are rejected if they have a noise rate over 8kHz, the typical noise rate for a PMT in SNO is a few hundred Hz. The energy resolution and the position resolution of the reconstructed event positions are largely dependent on the spread in the transit time, the photon efficiency, and the noise rate.

By themselves the 9456 PMTs would have about a 35% photocathode coverage. To increase this, reflectors are placed around the PMT to concentrate light back into the PMT. This increases the effective coverage to 54%. Figure 3.3 shows a schematic of the PMT with the surrounding concentrator. Another important constraint on the PMT characteristics is that they must have a low failure rate since they cannot be replaced during operation.

3.2 Electronics and Data Acquisition

For the neutrino events detected by SNO there at most will be on average one photon hitting any given PMT. Therefore the PMTs must be operated in a mode in which they are sensitive to single photoelectrons. Some fraction of the time a photon that strikes a PMT will generate an electrical pulse. PMTs that generate an electrical pulse are said to be hit PMTs. For each hit PMT, the PMT is identified, and the time and charge of the electrical pulses are measured and recorded. The SNO electronics must be able to handle background rates of more than 1kHz and a possible supernova rate of 1MHz without introducing too much dead time. Figure 3.4 shows the path the PMT pulses take through the SNO electronics chain. The signal processing is divided up into 19 crates which each process signals from 512 PMTs. A waterproof

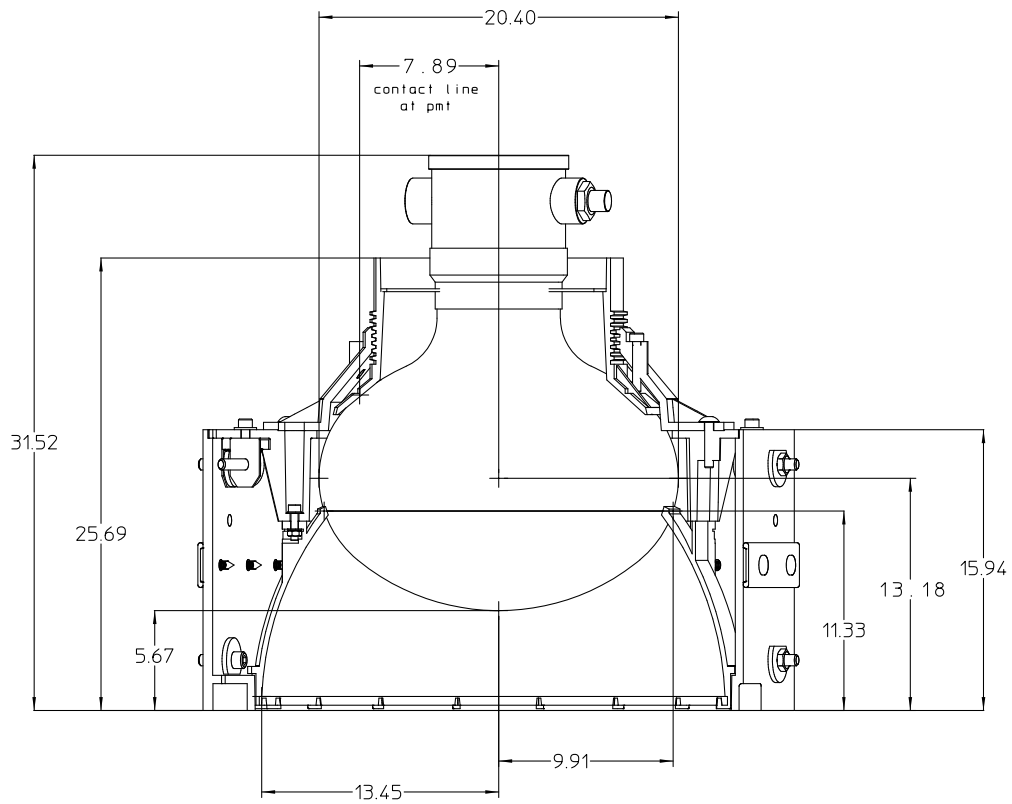


Figure 3.3: The Hamamatsu R1408 Phototube and the surrounding light concentrator.

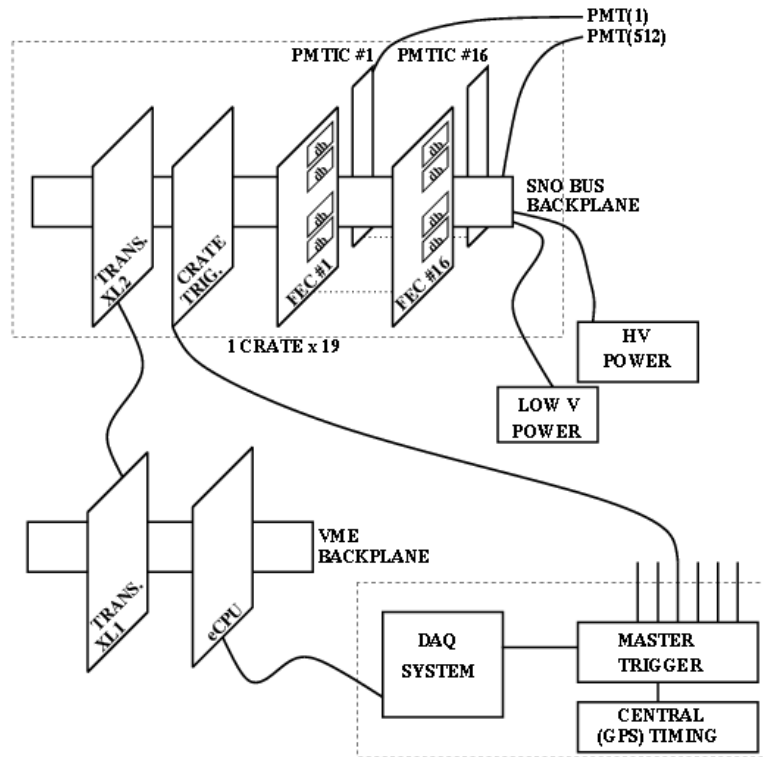


Figure 3.4: The SNO data acquisition electronics. Taken from [18].

coaxial cable carries the signal and voltage from each PMT in groups of 8 to a PMT interface card (PMTIC) at the rear of the crate. There are 16 PMTICS per crate. The signal from the PMTICs then enters one of sixteen front end cards (FECs) where it is processed by custom application specific integrated circuits (ASICs). One FEC digitizes the signals from 32 channels, or PMTs, and the digital results are stored in 4MB of onboard memory. The analog signal is then passed into a four channel discriminator chip (SNOD) where any leading edge is observed by a fast discriminator to determine when the PMT fired. Charge information is passed to an eight channel charge integrator (SNOINT). Another chip set (QUSN7) provides analog memory, a time to amplitude converter (TAC), and channel and trigger logic for the SNO detector. The QUSN7 chip also receives the information from SNOD to start the time measurement cycle which is used to generate a trigger for the event.

3.2.1 Generating an Event Trigger

The number of PMTs hit for a given event is defined as NHIT and is a function of the energy of the event. Low NHIT events correspond to low energy events. These low energy events are dominated by radioactive background. The radioactive backgrounds occur at a rate too large for the SNO data acquisition to handle. Therefore a simple hardware trigger is employed where only events that have more than 13 PMT hits are recorded. For analysis we set a higher threshold and require 20 hits for an event, or roughly 2MeV. Figure 3.5 shows a schematic representing the single channel timing cycle. Since the diameter of the PSUP is 18 meters, the time that it takes photons from a single Cherenkov event to reach different PMTs can differ by as much as 66ns. The time spread could be even longer due to multiple reflections. The time window then for the primary trigger was therefore set to 100ns. If 17 hits are detected within

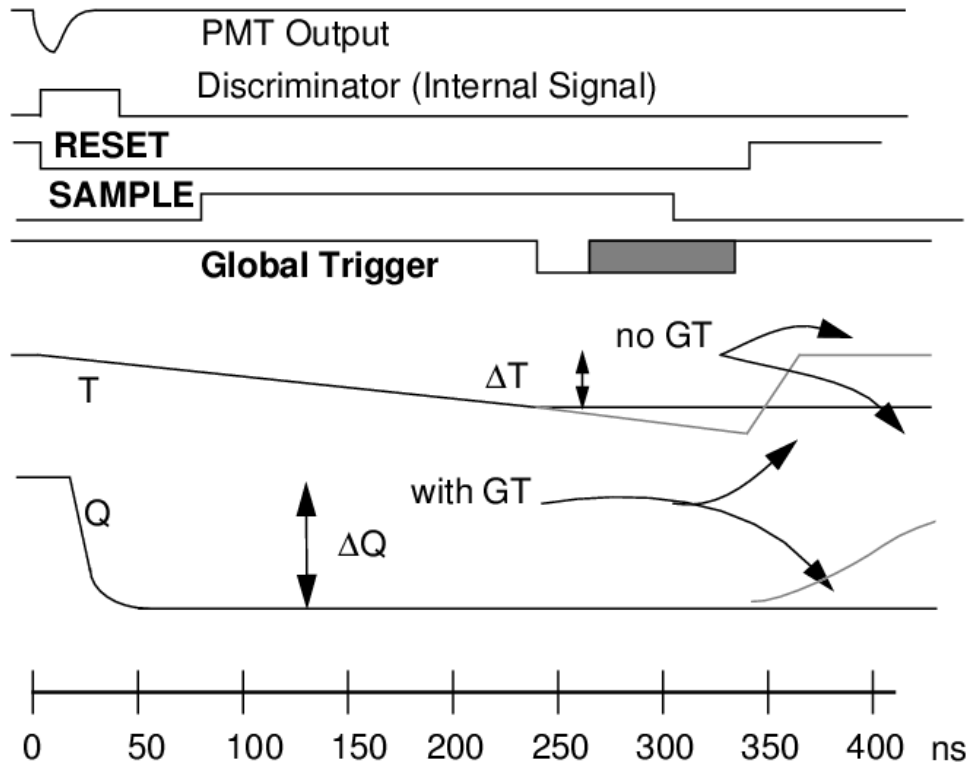


Figure 3.5: Single channel timing cycle. Taken from [18].

a 100ns window a global trigger (GT) signal is sent back through the electronics system. This trigger threshold can be adjusted by the software and is higher than the 13 hit hardware trigger so as not to overwhelm the data readout. The timing sequence shown in figure 3.5 and TAC are initiated for each channel on the leading edge of the signal from the SNOD. The TAC is stopped when a GT is detected in the electronics system or after 400ns from the start time. The dead-time introduced by the 400ns time out is negligible.

For each GT event, a global trigger identification number (GTID), the time of the trigger as recorded by a 10 and 50MHz clock, and the identification number of each PMT are stored. From the identification of each PMT the position of the hit PMTs for a given event are known. The digitized charges and their times from each PMT are also stored. All this information is used to reconstruct the event position, determine the energy, and generally determine all the required observables to extract neutrino events.

3.3 Calibration of SNO

The calibration of the SNO detector is essential in understanding and testing the response of the detector. Various algorithms are used to determine the best measurement of various observables, including energy, position, direction, and time of the event. The calibration program determines and tests the relationship between each actual and measured observable. All calibration sources used in the heavy water are deployed through the neck of the AV. Sources can also be deployed in light water between the AV wall and the PSUP. Sources that go into the light water are deployed through guide tubes that are accessible from the deck above the detector.

A list of the calibration sources used by SNO are given in table 3.1. The most often used calibration sources are the pulsed nitrogen laser (Laserball), the ^{16}N γ -ray source, and the ^{252}Cf fission neutron source. The Laserball is used for optical calibration and calibration of the PMT timing. The Laserball works by transmitting light produced by a pulsed nitrogen laser through fibre optics into a light diffusing sphere. The nitrogen laser is located on the deck, while the Laserball is deployed in the detector. The dependence of the energy response on event position and direction is also calibrated with the Laserball source. The ^{16}N source is the primary energy and position calibration source used by SNO. The ^{16}N is generated by passing CO_2 gas near a fast neutron generator. The (n,p) reaction on ^{16}O produces ^{16}N , which is then transported to a source deployed in the detector through an umbilical tube. The rate of the source can be varied by adjusting the CO_2 flow rate or the neutron output rate. The life-time of ^{16}N is 7.13sec. This is long enough such that a sufficient amount of ^{16}N decays within the source geometry. Inside the source chamber there is a PMT that detects β -particles from the decay of ^{16}N . This allows one to identify ^{16}N events that decay in the source chamber, and not in the umbilical. The ^{16}N is therefore a tagged source. The most important neutron calibration source used in SNO is the ^{252}Cf fission neutron source. The neutron calibration is described in detail in chapter 5.

As mentioned above, the sources are deployed through the neck of the AV. The calibration sources are either deployed in single or multi-axis mode. In single axis a single rope is attached to the source and the source can only move up or down (in the z direction). In multi-axis operation two more ropes are attached to the source which can pull the source off the z axis in the x or y direction. The source position is most accurately known during single axis deployment. Figure 3.6 shows a schematic of a

Source	Emitted particle	Calibration
Pulsed nitrogen laser	337,369,385, 429,505,619nm light	optical, PMT timing
^{16}N	6.13MeV γ -rays	energy, position reconstruction
^{252}Cf	fission neutrons	neutron efficiency
^8Li	β spectrum	energy non-linearity, position reconstruction as a function of energy
Am-Be	(α ,n) neutrons	neutron efficiency
U, Th	$\beta - \gamma$ decay	backgrounds
Dissolved Rn spike	$\beta - \gamma$	backgrounds

Table 3.1: The primary calibration sources used by SNO. The particles that each source emits and the calibration purpose of each source are also listed. Table has been adapted from [1].

source deployed in multi-axis mode. The design of the source deployment system only allows the source to be deployed at positions far from the central axis in the bottom half of the detector. In the upper half only limited movement from the central axis is allowed. The total coverage of the source deployment system is about 65%.

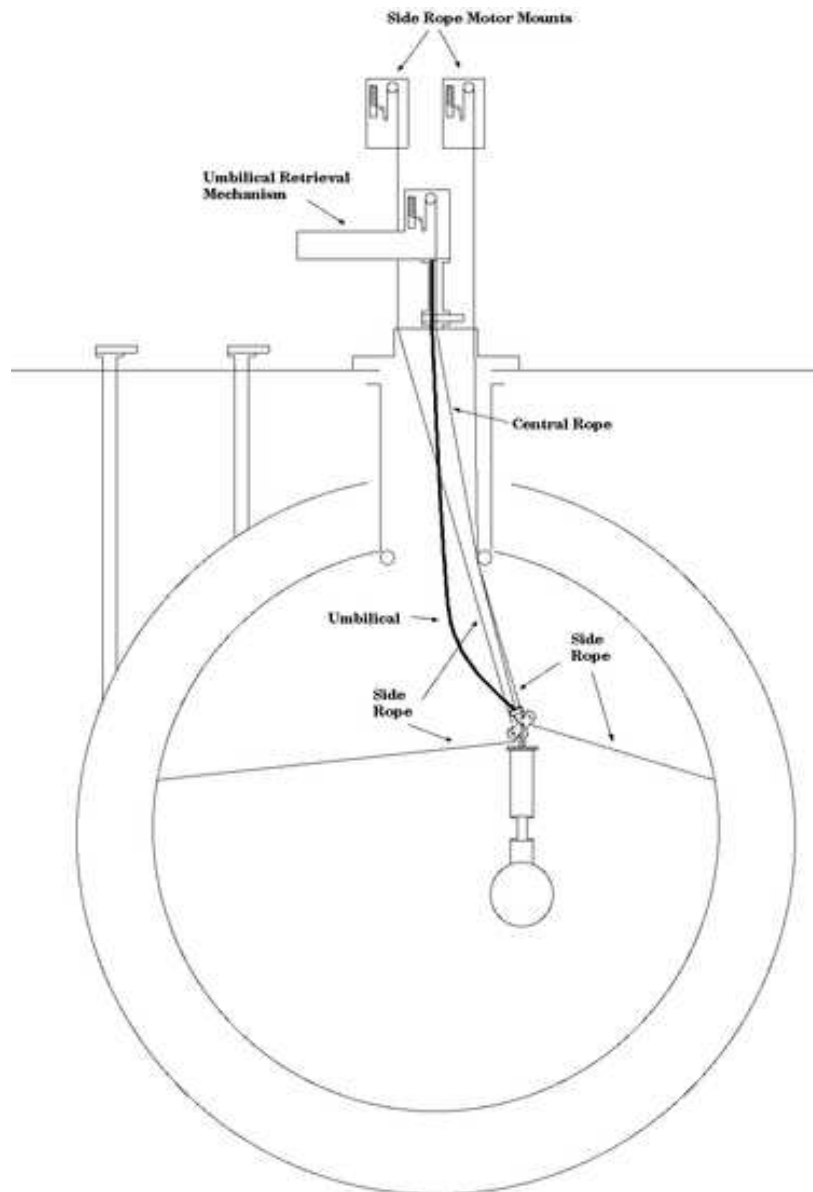


Figure 3.6: Schematic of the deployment of a calibration into the heavy water in multi-axis mode. Shown also are the sideropes that are necessary to move the source in the x and y planes. If the source needs to be deployed in the light water then one of the guide tubes can be used.

Chapter 4

Data Selection and SNO

Observables

The neutrino candidate events in SNO make up a small fraction of the total number of events detected. The radioactive background events in SNO cannot be separated from the neutrino signal on an event-by-event basis. They can only be separated statistically through a signal extraction. However there are a large fraction of background events that can be removed from the neutrino data through data selection. Instrumental backgrounds and muon events can be easily removed from the data by simple data cleaning cuts. These cuts are known as first order data cleaning cuts since they can be applied before the vertex and energy information of the event is reconstructed. The total event rate above the neutrino analysis energy threshold from electronic noise is about one event per minute. This is much higher than the neutrino rate. Without the first pass data selection cuts it would therefore be impossible to extract a neutrino signal. After the event vertex is reconstructed the second pass data selection can be applied. In the second pass data selection events can be re-

moved based on whether or not they reconstruct within a certain volume region, if their energy is above a chosen threshold, or simply if the event has a bad fit and the reconstruction algorithm does not converge.

4.1 First Pass Data Selection

The primary events that are removed through the first pass data selection are instrumental background events, electronic pickup events, AV neck events, muons, and the spallation neutrons that follow the muon events. The first pass data selection tags candidate events such as these so that they can be easily removed before data analysis.

4.1.1 Flasher Events

Flashers are events caused by discharge in the PMT dynode chain or base that produces a large flash of light and electrical charge that is seen in the PMT and pickup in the surrounding channels. They are categorized as instrumental background events. The distinguishing feature of a flasher event are a large number of registered hits in adjacent channels and a large number of hit PMTs on the other side of the detector.

4.1.2 Neck Events

These events are removed from the neutrino data. There are four PMTs in the neck that are used to detect light in the neck. If at least two of those PMTs register a hit then the event is flagged as neck event.

4.1.3 Burst Events

The solar neutrino rate in SNO is about 15 detected neutrino events per day. Therefore the probability that two or more events occur within a few seconds of each other is extremely low. Potential background events are therefore removed by flagging events that occur within a short a time of each other. There are three categories of events that are flagged by the burst cuts. These types are classified according to the time window used to search for event coincidences, the number of events inside the coincidence window, and the number of PMTs hit for the events (N_{hit}). The first category of burst events are tagged by the re-trigger cut. This cut requires that two or more events occur within a 1000nsec window. There is no N_{hit} threshold for this cut. The re-trigger cut removes all events occurring within 100msec of the first event. The second class of burst events are tagged under the high N_{hit} cut. To trigger this cut 40 or more events must occur within a 1sec window with a minimum N_{hit} of 20. If this happens then all data within 1sec is removed. Finally there is the high rate cut. For this cut to apply two or more events must occur within a 100msec window with a minimum N_{hit} of 60. The dead time for this cut is 1sec. Since most of the calibration data is taken at a very high rate the burst cuts are not applied to calibration data events.

4.1.4 Muons and muon followers

Muons and neutrinos are the only cosmic ray induced particles that make it to the depth of the SNO detector. The muon rate in SNO is about three per hour, considerably higher than the neutrino rate. The muon events themselves can be easily tagged since they deposit a lot more energy in the detector than the neutrino events.

A typical muon event generates enough light so that photons strike most of the PMTs in the detector compared to about 50 PMTs for a typical neutrino event. Spallation events that follow a muon generate a background to neutrino events that is much more difficult to identify. To eliminate the possibility of these muon follower events from entering the data set a dead time is introduced after a muon event of twenty seconds. Muon events are tagged if five or more outward looking tubes are hit and if 150 or more PMTs are hit. The N_{hit} criteria of 150 PMTs corresponds to roughly 20MeV of energy, considerably higher than the 8B neutrino energy spectrum. There is also another tag that is applied to events that occur within 250 msec of an event that has 150 PMT hits. This tags spallation neutrons that might follow a muon event that was missed or an atmospheric neutrino event.

4.2 Second Pass Data Selection - Higher Order Cuts

Most of the higher order cuts are implemented to reduce the background contamination in the neutrino signal region. The second pass data selection is applied after the energy and position of the events have been reconstructed. This data selection is applied while analyzing the data and is dependent on the analysis one wants to perform. Examples of higher order data cleaning cuts are an energy threshold cut or a radial (fiducial volume) cut. For the analysis presented in this thesis an energy threshold cut of 4MeV was used and the data were analyzed up to a radius of 576cm. The total D_2O volume extends to 600.5cm but the external radioactive backgrounds dominate the signal near the acrylic vessel (AV). Cuts are also made on the event isotropy to eliminate background and misreconstructed events. The isotropy of an

event refers to the PMT hit pattern of an event relative to the reconstructed position of the event. The isotropy is defined as the mean angle between any two hit PMTs for a given event. For the analysis of the salt phase data the isotropy parameter used was a function of the Legendre polynomials of the pair angles between the PMTs. This parameter, designated β_{14} , is defined as

$$\beta_{14} = \beta_1 + 4\beta_4, \quad (4-1.a)$$

$$\beta_1 = \frac{2}{N(N-1)} \sum_{i=1}^{N-1} \sum_{j=i+1}^N \cos\theta_{ij}, \quad (4-1.b)$$

$$\beta_4 = \frac{2}{N(N-1)} \sum_{i=1}^{N-1} \sum_{j=i+1}^N \frac{1}{64} (9 + 20\cos 2\theta_{ij} + 35\cos 4\theta_{ij}) \quad (4-1.c)$$

where

θ_{ij} is the angle between PMT i and j for a given event,

β_1 is the first order Legendre polynomial of the pair angle,

β_4 is the fourth order Legendre polynomial of the pair angle.

The CC and ES neutrino events produce single Cherenkov ring events that have a different distribution in the β_{14} parameter than the multi-Cherenkov ring NC events. For the salt phase analysis the neutrino data was analyzed in the β_{14} parameter range between -0.12 and 0.95. Almost the entire neutrino signal falls within this region. A large fraction of external background events that mis-reconstruct inside the heavy water will have a β_{14} value above this range and therefore will be excluded by the β_{14} cut. Also, this cut excludes events that are very isotropic that are probably non-Cherenkov events which have a β_{14} value below -0.12.

4.2.1 In-Time Ratio

The light that reaches the PMTs may go through multiple reflections off the AV, the PMT glass, or the PMT reflectors. The reflected light reaches the PMTs later in time than the direct, prompt, light. For most of the neutrino signal events the Cherenkov light occurs within a prompt time window of the reconstructed time of the event. The prompt time window is defined to be 10ns around the peak of the prompt light. Figure 4.1 shows the number of PMT hits as function of the PMT hit time relative to the time of the event for an ^{16}N source calibration run.

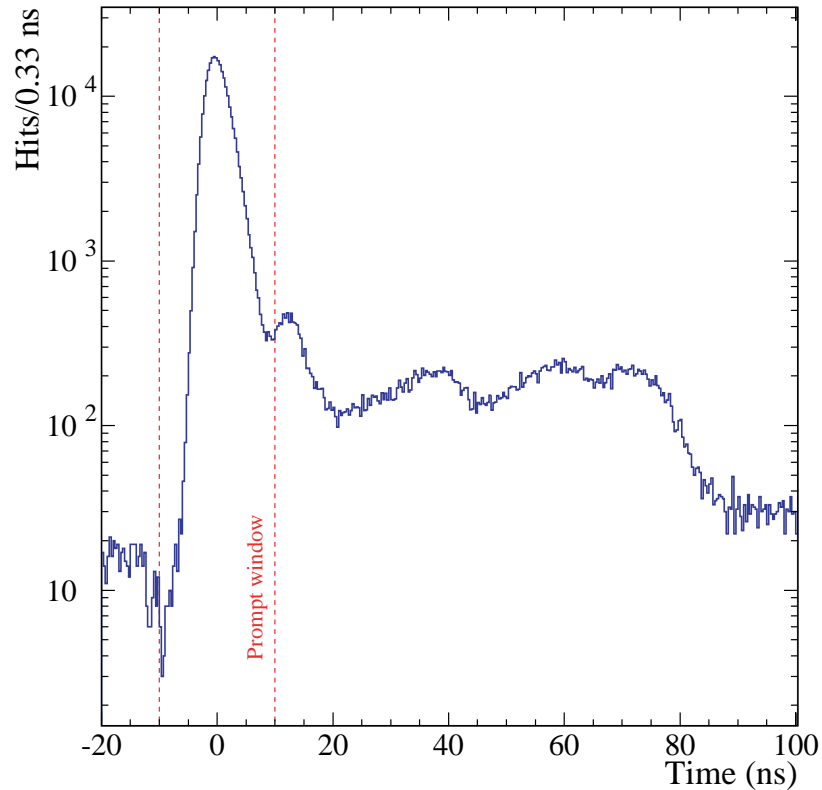


Figure 4.1: The number of hit PMTs as a function of the PMT hit time relative to the calibrated event time for an ^{16}N source . Most of the light falls within the prompt peak. Taken from [1]

For the neutrino data analysis an in-time ratio (ITR) cut is applied. ITR is the ratio of the number of hit PMTs in the prompt time window of $\pm 10\text{ns}$ compared to the number of hit PMTs outside the window. For the salt analysis the ITR cut used is

$$ITR > 0.55$$

The ITR cut removes many of the flasher events described in section 4.1.1. The flasher events have a flat PMT time distribution, presumably because of the light generation mechanism during the discharge in the PMT base. This means that the PMT hits for a flasher event are spread out in time with no real distinct peak corresponding to prompt or late light. Therefore the ITR value for flashers falls outside the cutoff of 0.55. The ITR cut may also remove some background events that originate near the PMTs or even within the PMTs themselves. The light produced by outward going events near the PMTs could have a shallow angle of incidence upon the PMTs and therefore could be almost fully reflected. For these events the late light reflection peaks could be substantial compared to the prompt peak and therefore the ITR condition would fail for these events.

4.3 Results of Data Cleaning Cuts

The number of events removed by the data cleaning is more than a hundred times larger than the expected neutrino signal. Figure 4.2 shows the N_{hit} (number of hit PMTs) spectra after applying the various first order and high level data cleaning cuts. The flasher event cuts are part of the cuts labeled as the PMT instrumental cuts. It is evident that a large amount of the data cleaning is done by these cuts. The upper limit on the number of instrumental background events left in the neutrino data set after the low level cuts were applied is 3. Therefore the efficiency of the low

level cleaning cuts is very nearly 100%. The high level cleaning cuts are less efficient however this efficiency is included in the neutrino flux determination.

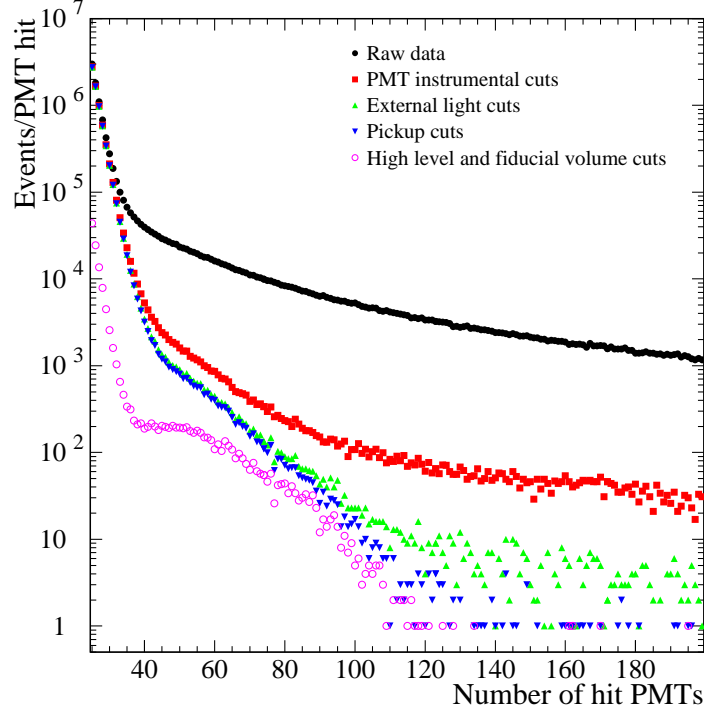


Figure 4.2: The number of hit PMTs (NHits) distribution after applying the first and higher order data cleaning cuts. The fiducial volume cut used for the higher order cuts was 550cm. This means that events that reconstructed outside 550cm were removed. Taken from [1]

As demonstrated in figure 4.2 the data cleaning cuts are very effective at removing background events. The number of neutrino signal events that are removed by the data cleaning cuts are correspondingly very small. Figure 4.3 shows the signal loss for the three neutrino signals as a function of reconstructed detector energy due to the second order cuts. The highest signal loss occurs in the lowest energy bins. The overall integrated signal loss is very small. The plots have been generated from Monte-carlo

calculations of the three neutrino signals.

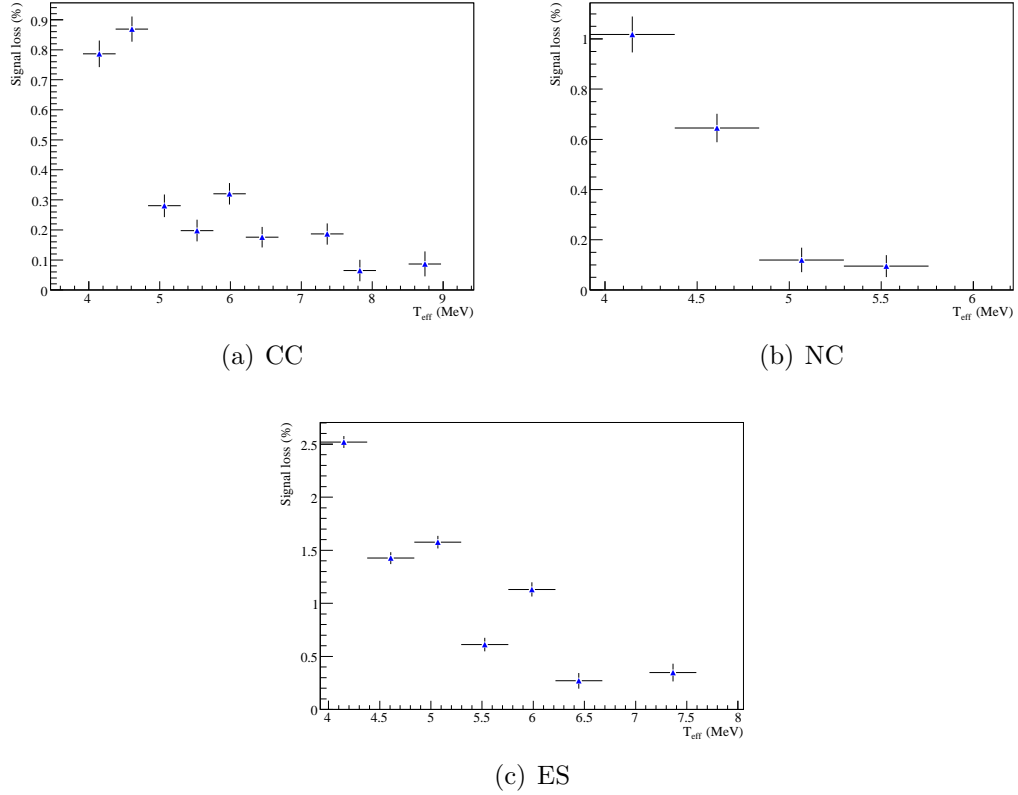


Figure 4.3: Signal loss for the three neutrino signals as a function of energy from the higher order cuts. The bins with no value are the energy bins in which no signal loss was measured.

The total integrated signal loss in the energy range of 4MeV to 20MeV for the three neutrino signals are summarized in table 4.1.

Signal	Signal loss (%)
CC	0.26%
NC	0.13%
ES	0.68%

Table 4.1: The integrated signal loss from 4MeV to 20MeV for the three neutrino signals. The neutrino analysis in this thesis is for an energy threshold of 4MeV

Chapter 5

Neutron Calibration of SNO

The neutron detection efficiency is a critical parameter needed to determine the number of neutrons generated from the number of neutrons detected. This parameter is a critical element of the calibration of each of the phases of the SNO experiment. In the pure D_2O phase most of the NC neutrons that captured within the D_2O volume captured on deuterium. However, a little over 50% of neutrons did not capture within the D_2O and were capture in the AV and light water. With the addition of salt most captures are on ^{35}Cl and the detection efficiency is approximately 3 times higher compared to the pure D_2O phase. Natural chlorine contains 24.2% ^{37}Cl however neutron captures are dominated by captures on ^{35}Cl since the cross-section is much higher for ^{35}Cl , 43.6b compared to 0.05b. The neutron Monte-carlo contains the proper abundances of chlorine and the other elements in SNO.

The neutron capture reaction on ^{35}Cl produces ^{36}Cl in an excited state. The ^{36}Cl then de-excites with a cascade of γ -rays with a total possible energy of 8.6MeV. These γ -rays then Compton scatter electrons. The Cherenkov light of the electrons that are above the Cherenkov energy threshold are then detected by the PMTs.

As shown in Figure 5.1, the peak of the energy response in the salt phase is higher than in the pure D_2O phase so for a given energy threshold more neutrons are accepted. Neutron detection efficiency is defined as the efficiency for detecting a neutron produced anywhere within the 600cm radius of the acrylic vessel (AV) after all the analysis cuts have been applied

$$\epsilon = \frac{N_{R,cuts}}{N} \quad (5-1)$$

where

ϵ is the neutron detection efficiency,

$N_{R,cuts}$ is the number of detected neutrons inside a radial region R and with all the analysis cuts applied, and

N is the total number of neutrons generated inside the 600cm volume.

The analysis cuts include all the first and higher order cuts described in chapter 4 and any energy threshold applied. For a neutron calibration source, the total number of neutrons N is defined as

$$N = R_s l \quad (5-2)$$

where

R_s is the neutron source rate in neutrons per second, and

l is the length of the calibration run.

To determine the neutron detection efficiency from calibration data it is therefore important to know the source rate. The primary neutron calibration source used in

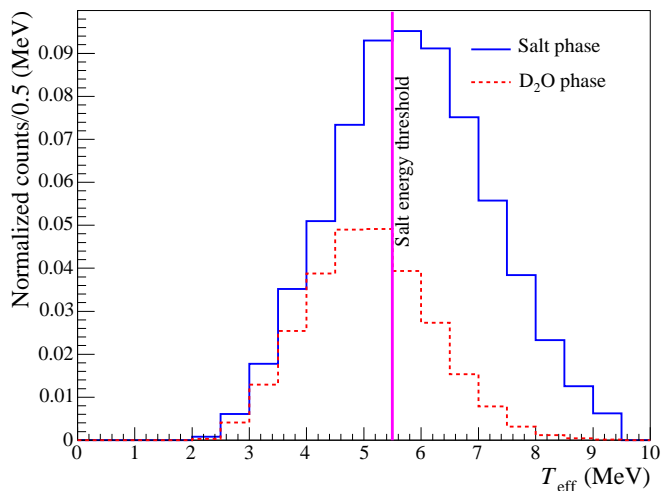


Figure 5.1: Shown are neutron energy spectra for pure D_2O (red) and salt (blue) running periods. The vertical line represents the energy threshold for the published salt papers.

SNO is a ^{252}Cf spontaneous fission source. An $^{241}\text{Am-}^9\text{Be}$ (α, n) source is also used to check the ^{252}Cf calibration. Since the NC neutrons are generated uniformly inside the heavy water volume the ^{252}Cf calibration source is deployed at different radial positions in the detector to get a volume weighted efficiency and to test how well the Monte-carlo simulates the geometrical differences of neutron capture at known locations. The point source efficiencies are fitted to an empirical function that agrees well with the data. The neutron diffusion model [19] that had been used to model neutron transport during the pure D_2O phase was found to be insufficient for the salt data. The neutrons produced in NC reactions have energies peaking at 100KeV compared to energies peaking at 2MeV for ^{252}Cf fission neutrons. Monte carlo studies have been carried out to determine the neutron detection efficiency correction due to this energy difference. Other corrections are also applied to the detection efficiency measurement to account for source geometry and the non-uniform source sampling

of the heavy water.

5.1 The Calibration Sources

Neutron response is calibrated primarily with neutrons produced by a ^{252}Cf source with secondary checks made by analysis of neutrons generated by an $^{241}\text{Am-}^9\text{Be}$ source. To determine the neutron detection efficiency using the ^{252}Cf fission source, the absolute neutron production rate (source strength) had to be determined. Shown in Table 5.1 are the results of four different techniques used in evaluating the source strength. The ^{252}Cf activity decays away with a half-life of 2.64 years, and the reference date for the source is taken as June 12, 2001. The decay constant of the source is taken into account in evaluating the source strength at the time of a given calibration run. The ^{252}Cf source contains a small fraction of ^{250}Cf which also emits neutrons but with a different multiplicity, and it has a longer life-time than ^{252}Cf . This is taken account in the source strength calculation. The ^{252}Cf source decays by α -emission and via spontaneous fission with the emission of a burst of neutrons. The branching ratio for spontaneous fission is only 3.1% with rest being α decays. Along with the neutrons, γ -rays are also emitted in the fission. The daughter products of the fission can also β decay and emit β -delayed γ -rays.

The ^{252}Cf source is encapsulated in an acrylic cylinder measuring about 5cm in diameter and height. Right above the cylinder is an acrylic or Teflon stem approximately 30cm in length that attaches to a stainless steel weight cylinder. A drawing of the source geometry is shown in Figure 5.2.

The Frish Grid and triggered Si(Li) methods both use an array of calibrated ^3He detectors to detect neutrons with the Si(Li) method being triggered on the fission

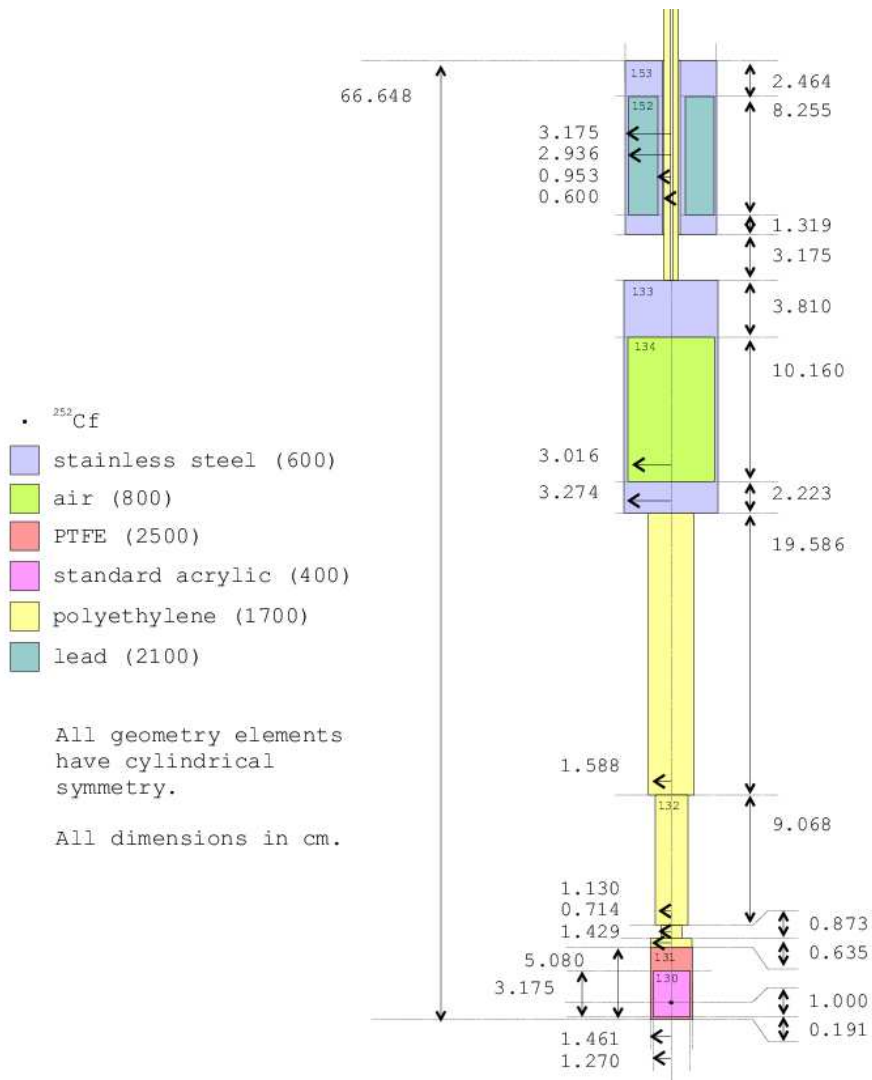


Figure 5.2: Drawing of the ^{252}Cf source geometry.

daughter products of ^{252}Cf . These two methods provide independent measures of the source strength prior to source deployment in the SNO detector. In-situ measurements of the source strength and efficiency have also been made from calibration data during the pure D_2O and dissolved-salt phases of the experiment. The D_2O multiplicity method is an in-situ method used in the initial D_2O phase of SNO running to determine the detection efficiency and fission rate. In this method the distribution of the number of neutrons detected in 2 second windows is plotted and then fit to the multiplicity function. The probability for the ^{252}Cf source to generate r neutrons is given by a Gaussian

$$P(r) = \frac{e^{-\frac{(r-\mu)^2}{2\sigma^2}}}{(2\pi\sigma^2)^{0.5}} \quad (5-3)$$

where the parameters have been measured to be

$$\begin{aligned} \mu &= 3.767 \text{ is the neutron multiplicity for } ^{252}\text{Cf}, \text{ and} \\ \sigma &= 1.57 \text{ is the width of the neutron multiplicity.} \end{aligned}$$

The above measurements are taken from [20]. The neutron multiplicity measurements described in [20] were done by looking at the number of neutrons that capture on Gd in a Gd-doped scintillator. The γ -rays that are produced in the de-excitation of Gd stimulate light in the scintillator which is then detected by PMTs. The scintillator output is triggered on the detection of the fission fragments from ^{252}Cf . When the neutron detection efficiency, ϵ , and fission rate, λ , are taken in to account the probability for detecting d neutrons in a given time window is then

$$P(d) = \sum_{r=d}^{\infty} \epsilon^d (1-\epsilon)^{r-d} \sum_{N=1}^{\infty} \frac{e^{-\frac{(r-N\mu)^2}{2N\sigma^2}}}{(2\pi N\sigma^2)^{0.5}} e^{\lambda T} \frac{(\lambda T)^N}{N!}, \quad (5-4)$$

where T is the time window. The detection efficiency, ϵ , and the fission rate, λ , are the free parameters in the fit. Another technique, the time-series method, has

been used in the salt phase to extract the neutron detection efficiency and the fission rate by using the time separation between γ -rays and neutrons. As can be seen, the various techniques are in good agreement and we employ a weighted mean as our best estimate of the neutron source strength.

Table 5.1: Results of the various methods for determining the ^{252}Cf source strength. The source strength is determined for June 12, 2001.

Method	Source strength (neutrons per second)
LANL Frisch Grid	16.75 ± 0.14
LANL Triggered Si(Li)	17.08 ± 0.43
D_2O Multiplicity	16.33 ± 0.18
Salt Time-Series	16.46 ± 0.18
Weighted Mean	16.55 ± 0.08
χ^2 Renormalized	16.55 ± 0.12

The other neutron source, $^{241}\text{Am}-^9\text{Be}$, produces neutrons through the $^9\text{Be}(\alpha, n)^{12}\text{C}^*$ reaction with the α particles from the ^{241}Am . The ^{12}C de-excites with the emission of a 4.4MeV γ -ray which can be used as a neutron tag.

5.2 Burst Analysis Method for Selecting Neutron Events

The ^{252}Cf source emits γ -rays in coincidence with neutrons from spontaneous fission. Also, β -delayed γ -rays are also emitted from the fission daughter products. To determine the neutron detection efficiency, neutron events have to be selected from the rest of the source background. Since neutrons always come in coincidence with the fission gammas, a ‘burst cut’ has been developed to select neutron events from calibration data using the coincidence between fission γ -rays and neutrons. In salt, the mean capture time for neutrons is 5.3 msec and all neutrons are captured after approximately 40 ms. The mean time between fissions for the ^{252}Cf source used in SNO is about 250 ms. A fission γ candidate event is then selected by choosing events with no events prior to it in a 50 ms window, and events in a window of 40 ms after the selected first event are tagged as neutrons. Figure 5.3 shows how the neutrons are selected. The selection efficiency for the burst method is defined as

$$\epsilon_{sel} = \frac{N_{burst}}{N} \quad (5-5)$$

where

N_{burst} is the number of neutron events selected from the burst method, and

N is the number of neutrons generated defined by equation 5-2.

The contamination of the selected neutron events by γ -rays from the source is defined as

$$f_{\gamma} = \frac{N_{\gamma}}{N_{burst}} \quad (5-6)$$

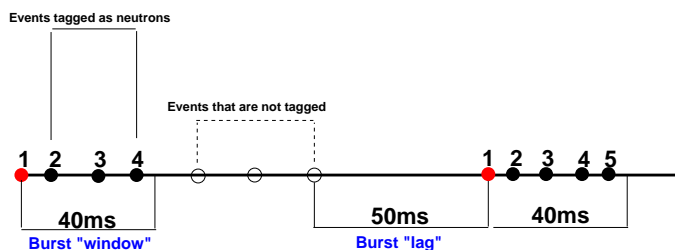


Figure 5.3: Diagram showing the neutron selection process of the 'Burst cut' used for the ^{252}Cf source in salt. The open circles labeled as events that are not tagged are due to random events from pileup of neutron bursts and from the decay of the fission daughter products.

where N_γ are the number of γ -ray events in the selected neutron events. For the burst analysis method applied to the ^{252}Cf data we get

$$\epsilon_{sel} = 0.4, \text{ and}$$

$$f_\gamma < 0.001.$$

So while we lose a substantial number of neutron events the source background contamination is almost eliminated. Figure 5.4 shows the energy as a function of radius from the source distribution for events reconstructing around the ^{252}Cf source at centre. The left panel is the raw ^{252}Cf data and the right panel is the data after the 'burst cut' has been applied.

The efficiency of the burst cut algorithm can only be determined by knowing the neutron detection efficiency. Therefore the selected neutron events from the burst cut cannot be used to determine the neutron detection efficiency. However, the raw ^{252}Cf calibration data is known to have a very small source γ -ray contribution above a

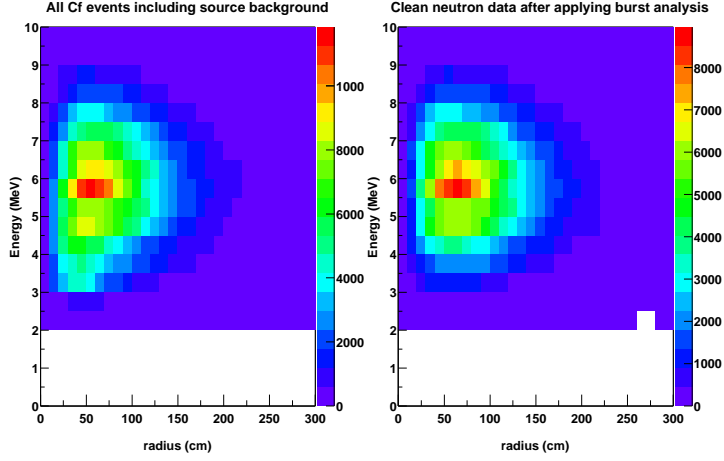


Figure 5.4: Energy vs. reconstructed event radius for raw ^{252}Cf data (left panel) and the data after the 'burst cut' has been applied.

threshold of $T = 6.5\text{MeV}$, therefore the selected neutron capture energy distribution provided by the burst cut is used to extrapolate the total number of neutrons above $T = 6.5\text{MeV}$ to the total number of neutrons above the required energy threshold. What is required then is the ratio of the number of events above the analysis threshold to the number of events above 6.5MeV

$$k = \frac{N_{burst}^{T_{eff}}}{N_{burst}^{6.5}} \quad (5-7)$$

where

$N_{burst}^{T_{eff}}$ is the number of neutron events selected from the burst method above the analysis energy threshold, and

$N_{burst}^{6.5}$ is the number of neutron events selected from the burst method above 6.5MeV.

The neutron detection efficiency is then [21]

$$\epsilon = \frac{kN_{6.5}}{lR_s} \quad (5-8)$$

where $N_{6.5}$ is the number of events above 6.5MeV in the raw ^{252}Cf data and l and R_s are the length of the run and source rate as previously defined.

5.3 Fitting to the Point Source Efficiency Measurements

The ^{252}Cf source was deployed in many positions to test our understanding of neutron capture in the detector as extensively as possible. From measuring the detection efficiency at all the source positions a volume weighted neutron detection efficiency can be determined. The source was deployed all the way out to 600cm (the AV position) in radius. However, due to limitations of the source deployment mechanism most of these positions are in the bottom half of the detector ($z < 0$). Corrections to a true uniform distribution of neutrons are described later. At every ^{252}Cf position a neutron detection efficiency is measured. The neutron detection efficiency is defined as the probability that a neutron produced at a given source position will be detected after all analysis cuts and is determined using equation 5-11. The point source efficiency results are fitted to an empirical model,

$$\epsilon(s) = A(\text{Tanh}(B(s - C)) - 1) \quad (5-9)$$

where $\epsilon(s)$ gives the neutron capture efficiency at source position s . There is no physical motivation for this form and was chosen since the hyperbolic tan function resembles the radial dependence of the neutron detection efficiency. The volume weighted efficiency is then obtained from the ratio of integrals

$$\epsilon = \frac{\int_0^{600.5} s^2 \epsilon(s) ds}{\int_0^{600.5} s^2 ds} \quad (5-10)$$

The AV can be thought of as a neutron sink since it has such a high cross-section for capturing neutrons and the resulting γ -rays are below the threshold. Therefore as the source is deployed further from the centre (closer to the AV) the neutron detection

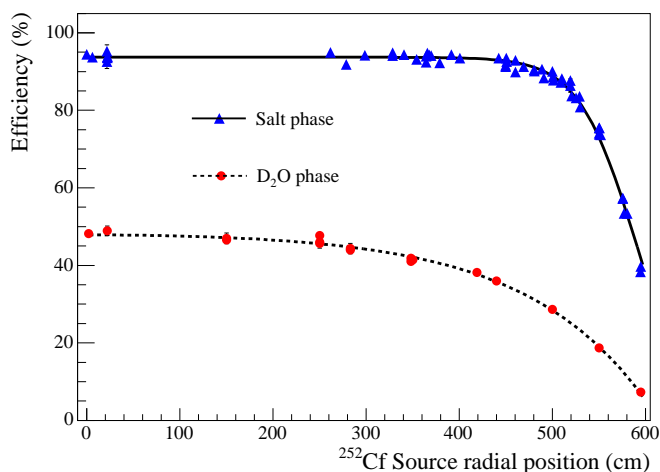


Figure 5.5: Shown are neutron capture efficiency vs radius curves for pure D_2O (red) and salt phase (blue) running periods.

efficiency decreases. Figure 5.5 shows the pure D_2O and salt phase phase ^{252}Cf point source efficiency measurements fitted to the empirical model.

5.4 Systematic Uncertainties and Corrections on the Calibration Data

The neutron detection efficiency relates the number of neutrons produced by the NC reaction inside the full heavy water volume to the number of neutrons detected inside the fiducial volume by

$$R_D = \epsilon R_{NC} \quad (5-11)$$

where ϵ is the neutron detection efficiency measured using equation 5-10 and R_D and R_{NC} are the detected and generated NC neutron rates respectively. The predicted

flux of neutrons from the NC reaction is

$$R_{NC} = \int_{E_{min,NC}}^{\infty} \frac{dN}{dE_{\nu}}(E_{\nu})\sigma_{NC}(E_{\nu})dE_{\nu} \quad (5-12)$$

where

- $E_{min,NC}$ is the threshold for the NC interaction on deuterium (2.23MeV), and
- $\frac{dN}{dE_{\nu}}$ is the neutrino energy spectrum, and
- σ_{NC} is the NC cross-section on deuterium.

The neutron detection efficiency derived from ^{252}Cf data therefore must be corrected so that it reproduces the NC detection efficiency. These corrections have uncertainties that need to be included in the overall neutron detection efficiency uncertainty. Other uncertainties associated with the ^{252}Cf source have to be taken account of in the detection efficiency measurement. The uncertainty on the source strength is 0.5%, as summarized in table 5.1. Systematics uncertainties from the 'Burst Cut' method have also been checked. The timing windows of the burst cut have been varied and no significant change in the neutron detection efficiency was seen. In terms of the source deployment there is a 2cm uncertainty for single axis source deployment and as much as a 10cm uncertainty for multi-axis deployment. This uncertainty is determined from the uncertainties on the rope lengths and rope tensions as measured by the manipulator system. The resulting uncertainty on the neutron detection efficiency is $^{+1.7\%}_{-1.0\%}$. Figure 5.6 shows comparisons with the ^{252}Cf source Monte-carlo and the radial distributions from the data shifted by $\pm 1\%$. The Monte-carlo is in agreement with data within the source position uncertainty. During the salt phase the position of the AV was determined to be 5.5cm below the centre of the PSUP. The position was determined using single axis calibration runs where the source touched the bottom

of the AV. The uncertainty on the AV position was estimated to be 6cm in the z direction. This translates into an uncertainty of 0.3% for a 550cm fiducial volume. This uncertainty was estimated by shifting the reconstructed z position of the events and the location of the 550cm fiducial volume relative to the detector centre by 6cm. These two effects almost entirely cancel each other out and that is why the uncertainty due to the AV position is relatively small. Another systematic uncertainty arises from how well the empirical fit matches the point source calibration data. A test of this was done by fitting the point source efficiency distribution to a high order polynomial and then comparing that efficiency result to the empirical model fit. The difference between the neutron detection efficiency calculated from the empirical fit and the efficiency from the polynomial fit is 0.4%. This is added as an uncertainty to the neutron detection efficiency measurement. Figure 5.7 shows the point source ^{252}Cf efficiency measurements fitted to the empirical fit + a polynomial.

Corrections also have to be applied to the point source efficiency measurement to convert it to a NC neutron efficiency. The most obvious difference between source neutrons and NC neutrons is the neutron energy. NC neutrons have energies of about 100KeV compared to above 2MeV for ^{252}Cf fission neutrons. This could be significant since only thermalized neutrons are captured. The ^{252}Cf neutrons would therefore need a longer distance to thermalize and capture than NC neutrons. A comparison has been made between Monte-carlo of uniformly distributed NC energy neutrons and ^{252}Cf neutrons. There is a $<0.1\%$ change in the determined detection efficiency. As mentioned before the source deployment positions are predominantly in the bottom half of the detector ($z < 0$). A Monte-carlo comparison has been done between ^{252}Cf energy neutrons at the same positions as the data and a uniform distribution of ^{252}Cf energy neutrons throughout the whole detector. The difference between point source

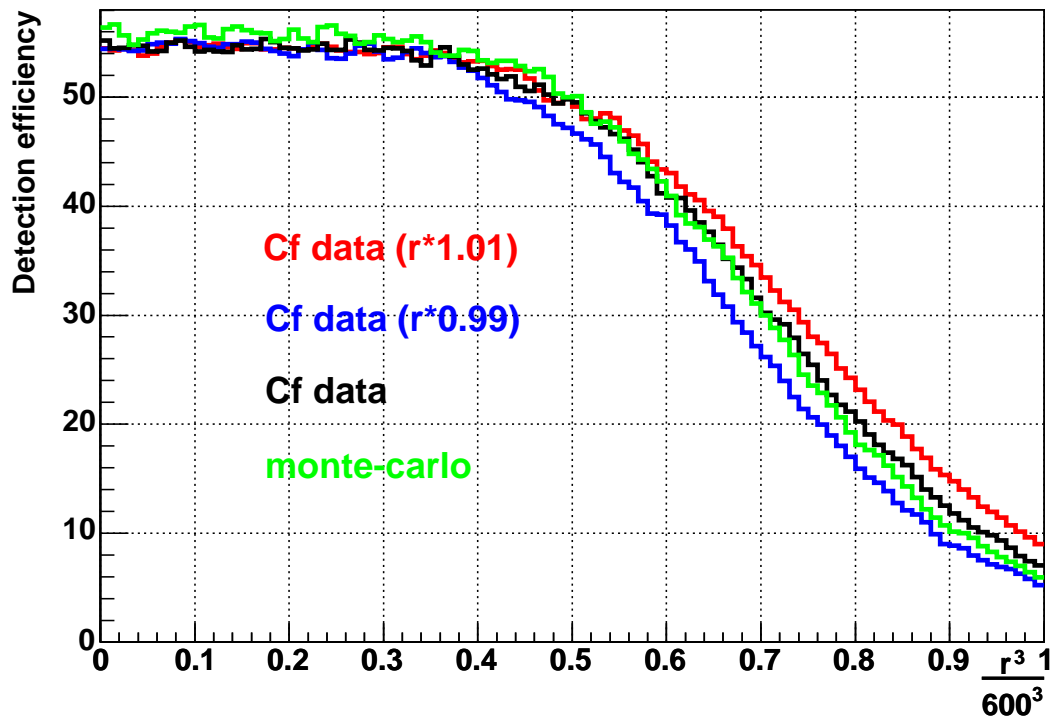


Figure 5.6: Comparison of Cf monte-carlo, and the Cf data radial distributions. Included are the curves for radial shifts of $\pm 1\%$

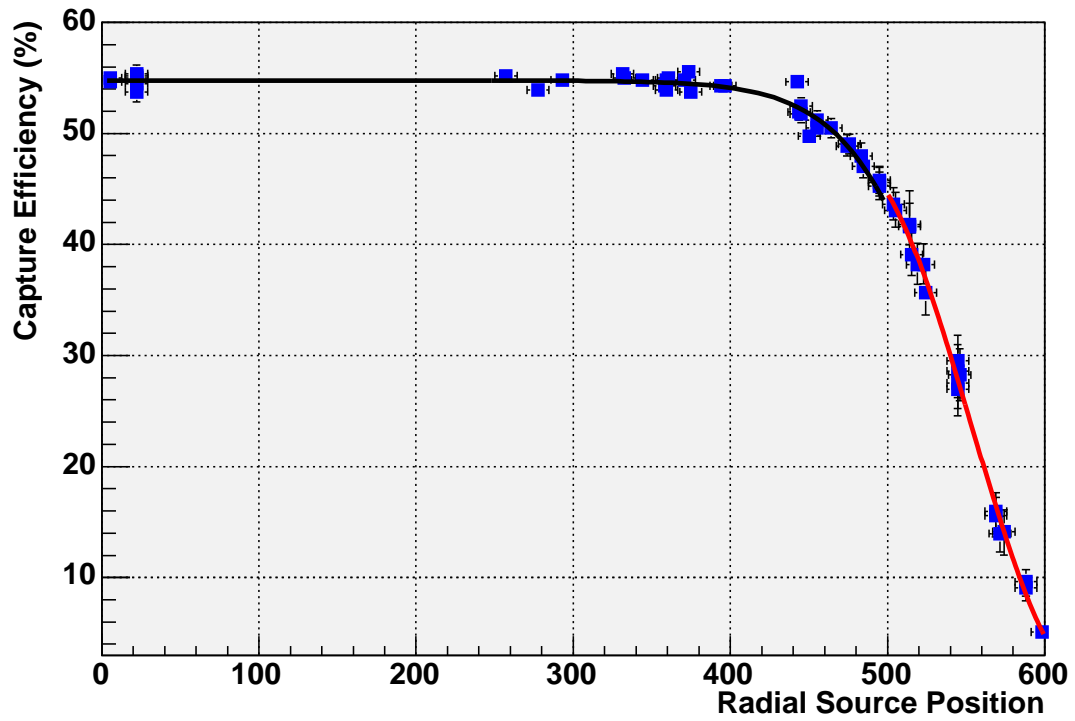


Figure 5.7: Combined Cf data set fitted to the empirical model between 0 and 500cm, and to a 4th order polynomial between 500 and 600cm.

Monte-carlo without any source geometry effects and uniform Monte-carlo was found to be $(2.45 \pm 1.04)\%$. This is applied as a sampling correction to the ^{252}Cf volume weighted data efficiency.

A small percentage of the ^{252}Cf neutrons capture on the stem or the weight cylinder and are not detected. A Monte-carlo study was done comparing ^{252}Cf runs with and without the source geometry. It was found that the correction that needs to be applied to the neutron detection efficiency measured from the ^{252}Cf data to compensate for neutron captures on the source is $(2.03 \pm 0.53)\%$. Cf fission neutrons have a significant cross section for $^2\text{H}(n, 2n)^1\text{H}$ and $^{16}\text{O}(n, \alpha)^{13}\text{C}$ reactions. For NC neutrons, these cross sections are negligible. Therefore the $^2\text{H}(n, 2n)^1\text{H}$ reaction would increase the efficiency determined from Cf data compared to NC neutrons, and the $^{16}\text{O}(n, \alpha)^{13}\text{C}$ would act like a neutron sink and decrease the determined efficiency from Cf data. Corrections due to these reactions are made to the detection efficiency determined from ^{252}Cf data and the size of the corrections are determined by comparing NC Monte-carlo with Monte-carlo of Cf energy neutrons. By chance these corrections almost fully cancel each other. Another correction that has not been mentioned above is the Gamma fraction correction which deals with the fraction of γ -rays in the calibration data above 7MeV. This correction is described in detail in the next section. A summary of the corrections and systematic uncertainties are shown in tables 5.2 and 5.3 respectively.

A full list of ^{252}Cf run positions and uncertainties is given in tables 5.4, 5.5, and 5.6.

Table 5.2: Corrections applied to the neutron efficiency measurement from the data.

Source	Correction
Source sampling	$-(2.45 \pm 1.04)\%$
(n,2n)	$-(0.58 \pm 0.10)\%$
(n, α)	$+(0.66 \pm 0.13)\%$
Source geometry	$+(2.03 \pm 0.53)\%$
Gamma fraction	$-(1.34^{+0.56}_{-1.05})\%$
Total size of correction	-1.73%

Table 5.3: Systematic uncertainties on the neutron efficiency measurement from the calibration data. The uncertainties are presented as relative uncertainties.

Source	Uncertainty
Source strength	$\pm 0.7\%$
Source position	$+1.7\%$ -1.0%
Gamma fraction	$+0.56\%$ -1.05%
AV position	$\pm 0.3\%$
(n,2n)	$\pm 0.10\%$
(n, α)	$\pm 0.13\%$
Source geometry	$\pm 0.53\%$
Empirical fit - polynomial fit	$+0.4\%$
Source sampling	$\pm 1.04\%$
Total uncertainty	$+2.31\%$ -2.02%

Table 5.4: ^{252}Cf run positions with their respective efficiencies for the first part of the salt phase. The source position uncertainty refers to the uncertainty on the neutron detection efficiency due to a shift in the source position. We notice from figure 5.5 that the detection efficiency changes very rapidly with radius for source positions near 600cm. This explains why the efficiency uncertainty due to source position uncertainty increases with radius.

Radial Position	Run	Eff.	Stat. error	Source Position Uncertainty
569.9	21010	15.5	$\pm 0.7 \%$	$+10.7 \%$ -12.5%
569.9	21015	15.9	$\pm 0.8 \%$	$+10.7 \%$ -12.5%
544.9	21017	27.4	$\pm 0.6 \%$	$+8.3 \%$ -8.3%
520.0	21019	38.2	$\pm 0.5 \%$	$+5.0 \%$ -4.7%
22.7	21023	55.1	$\pm 0.7 \%$	$+0.0 \%$ -0.0%
278.0	22334	53.8	$\pm 1.1 \%$	$+0.0 \%$ -0.0%
544.9	22338	28.5	$\pm 0.9 \%$	$+8.3 \%$ -8.3%
495.0	22342	45.7	$\pm 0.5 \%$	$+2.7 \%$ -2.5%
395.1	22344	54.2	$\pm 0.5 \%$	$+0.2 \%$ -0.2%
574.9	22346	14.1	$\pm 0.7 \%$	$+14.0 \%$ -15.0%
22.7	22348	54.3	$\pm 0.4 \%$	$+0.0 \%$ -0.0%
397.1	22351	54.3	$\pm 0.9 \%$	$+0.2 \%$ -0.2%
344.7	25710	54.8	$\pm 0.7 \%$	$+0.1 \%$ -0.1%
360.3	25712	53.8	$\pm 0.7 \%$	$+0.1 \%$ -0.1%
360.3	25714	54.8	$\pm 0.7 \%$	$+0.1 \%$ -0.1%
375.1	25721	53.7	$\pm 0.8 \%$	$+0.1 \%$ -0.1%
361.7	25723	55.0	$\pm 0.7 \%$	$+0.1 \%$ -0.1%
371.6	25725	54.7	$\pm 0.7 \%$	$+0.1 \%$ -0.0%

Table 5.5: ^{252}Cf run positions with their respective efficiencies for the 28000 series of runs.

455.3	28472	50.5	$\pm 1.2 \%$	$+0.8 \%$ -0.9%
524.0	28475	38.1	$\pm 1.0 \%$	$+4.9 \%$ -4.5%
546.6	28477	28.2	$\pm 1.4 \%$	$+8.3 \%$ -8.1%
544.8	28479	29.3	$\pm 0.8 \%$	$+7.9 \%$ -7.3%
514.3	28481	41.7	$\pm 1.1 \%$	$+7.2 \%$ -7.0%
514.3	28488	41.5	$\pm 1.9 \%$	$+4.6 \%$ -3.5%
504.2	28490	43.5	$\pm 1.0 \%$	$+3.3 \%$ -3.1%
475.8	28492	48.9	$\pm 1.1 \%$	$+1.5 \%$ -1.4%
464.3	28494	50.5	$\pm 1.2 \%$	$+1.1 \%$ -1.2%
485.9	28512	46.9	$\pm 1.2 \%$	$+2.0 \%$ -1.8%
445.6	28515	52.4	$\pm 1.2 \%$	$+0.8 \%$ -0.8%
589.4	28517	9.5	$\pm 1.3 \%$	$+11.3 \%$ -13.4%
589.1	28521	9.0	$\pm 1.7 \%$	$+11.9 \%$ -12.8%
495.8	28523	45.2	$\pm 1.0 \%$	$+2.7 \%$ -2.4%
294.0	28525	54.8	$\pm 1.1 \%$	$+0.0 \%$ -0.0%
332.6	28527	55.2	$\pm 1.1 \%$	$+0.0 \%$ -0.0%
332.6	28529	55.0	$\pm 1.1 \%$	$+0.0 \%$ -0.0%
5.9	28535	54.6	$\pm 0.6 \%$	$+0.0 \%$ -0.0%

Table 5.6: ^{252}Cf run positions with their respective efficiencies for the 31000 series of runs.

5.5	31137	54.8	$\pm 1.2 \%$	$\begin{smallmatrix} +0.0 \\ -0.0 \end{smallmatrix} \%$
445.9	31139	51.6	$\pm 1.2 \%$	$\begin{smallmatrix} +1.1 \\ -1.0 \end{smallmatrix} \%$
257.5	31141	55.1	$\pm 1.2 \%$	$\begin{smallmatrix} +0.0 \\ -0.0 \end{smallmatrix} \%$
444.9	31143	51.9	$\pm 1.2 \%$	$\begin{smallmatrix} +0.9 \\ -0.8 \end{smallmatrix} \%$
544.8	31145	27.0	$\pm 0.9 \%$	$\begin{smallmatrix} +8.7 \\ -8.9 \end{smallmatrix} \%$
524.7	31148	35.6	$\pm 1.1 \%$	$\begin{smallmatrix} +5.9 \\ -5.5 \end{smallmatrix} \%$
515.5	31150	39.0	$\pm 1.1 \%$	$\begin{smallmatrix} +4.9 \\ -4.8 \end{smallmatrix} \%$
505.2	31152	43.1	$\pm 1.0 \%$	$\begin{smallmatrix} +3.7 \\ -3.4 \end{smallmatrix} \%$
495.1	31154	45.5	$\pm 1.0 \%$	$\begin{smallmatrix} +2.8 \\ -2.5 \end{smallmatrix} \%$
483.9	31156	47.9	$\pm 1.2 \%$	$\begin{smallmatrix} +2.1 \\ -1.9 \end{smallmatrix} \%$
475.5	31158	48.8	$\pm 1.2 \%$	$\begin{smallmatrix} +1.7 \\ -1.4 \end{smallmatrix} \%$
455.3	31162	51.1	$\pm 1.2 \%$	$\begin{smallmatrix} +1.1 \\ -0.9 \end{smallmatrix} \%$
571.7	31164	13.9	$\pm 1.1 \%$	$\begin{smallmatrix} +11.2 \\ -11.9 \end{smallmatrix} \%$
374.6	31166	55.4	$\pm 0.9 \%$	$\begin{smallmatrix} +0.1 \\ -0.0 \end{smallmatrix} \%$
451.3	31168	49.6	$\pm 1.1 \%$	$\begin{smallmatrix} +0.9 \\ -0.7 \end{smallmatrix} \%$
443.7	31170	54.6	$\pm 0.9 \%$	$\begin{smallmatrix} +0.7 \\ -0.7 \end{smallmatrix} \%$
358.8	31173	54.1	$\pm 1.0 \%$	$\begin{smallmatrix} +0.1 \\ -0.0 \end{smallmatrix} \%$
22.3	32344	55.3	$\pm 1.5 \%$	$\begin{smallmatrix} +0.0 \\ -0.0 \end{smallmatrix} \%$
22.3	32519	53.6	$\pm 1.7 \%$	$\begin{smallmatrix} +0.0 \\ -0.0 \end{smallmatrix} \%$
22.3	33737	54.9	$\pm 0.7 \%$	$\begin{smallmatrix} +0.0 \\ -0.0 \end{smallmatrix} \%$
598.9	33739	4.9	$\pm 2.2 \%$	$\begin{smallmatrix} +11.7 \\ -12.8 \end{smallmatrix} \%$

5.5 Determining the Fission Gamma Fraction Above 6.5MeV

As mentioned previously, calculating the neutron detection efficiency requires extrapolating the number of events in the raw ^{252}Cf data above 6.5MeV to the number of events above the required energy threshold using the burst selected neutron energy distribution. There is however a small fraction of events above 6.5MeV that are fission γ -rays that have to be taken into account. In equation 5-8 the term $N_{6.5}$ is assumed to represent only the number of neutrons above 6.5MeV in the raw ^{252}Cf data. However it is known that there is a small contamination of source γ -rays in the ^{252}Cf data above 6.5MeV. It is therefore necessary to determine the γ fraction above 6.5MeV in the raw ^{252}Cf data so that the $N_{6.5}$ term in equation 5-8 can be adjusted to represent only the number of neutron events. In pure D_2O clean neutron events can be easily selected from fission γ -rays by taking events that reconstruct more than 150cm from the source since in pure D_2O the path length for neutrons is much longer than γ -rays. To get the γ fraction in the salt phase the ^{252}Cf data in the interim pure D_2O phase will be used in a combined fit with the salt phase data. The interim D_2O phase occurred after salt was removed in preparation for neutral current detector (NCD) deployment. To start with, the γ -ray energy spectrum in pure D_2O can be determined by

$$\frac{dN}{dE_\gamma} = \frac{dN}{dE_{r<150}} - \alpha \frac{dN}{dE_{nd}} \quad (5-13)$$

where $\frac{dN}{dE_{r<150}}$ is the energy spectrum of the events that reconstruct inside 150cm from the source in D_2O , and $\frac{dN}{dE_{nd}}$ is the neutron capture energy spectrum in D_2O . The raw ^{252}Cf energy spectrum in salt is then

$$\frac{dN}{dE_{Cf}} = \beta \frac{dN}{dE_{\gamma}} + \delta \frac{dN}{dE_{ns}}, \quad (5-14)$$

where $\frac{dN}{dE_{ns}}$ is the neutron capture energy spectrum in salt. By fitting to the raw Cf energy spectrum in salt, shown in figures 5.8 and 5.9, the parameters α , β , and δ can be determined. The γ -fraction above 6.5MeV calculated using the method described above is $(1.39^{+1.26}_{-0.56})\%$. This result relies on the energy spectra of the salt phase γ -rays to be the same as the pure D_2O phase γ -rays. To evaluate the sensitivity of the analysis to the uncertainty due to changes in the energy calibration between the phases the fits have been done with various relative energy scalings. The results are summarized in table 5.7. The γ fraction for the ^{252}Cf source was also estimated by comparing it to the $^{241}\text{Am}-^9\text{Be}$ (α, n) source [22]. The γ fraction obtained from the $^{241}\text{Am}-^9\text{Be}$ comparison was $(0.9^{+1.4}_{-0.9})\%$. The weighted average of the two methods gives a fraction of $(1.20^{+0.94}_{-0.48})\%$. This number still has to be corrected up by $(12^{+0}_{-12})\%$ to account for the change in γ fraction as a function of radial source position. After that correction is applied the γ fraction is $(1.34^{+1.05}_{-0.56})\%$.

Table 5.7: Gamma fractions determined for various D_2O energy scale shifts.

Energy Scale	Gamma fraction above 6.5MeV	Chi^2 / dof
+0%	$(1.39 \pm 0.12)\%$	24.6
+1%	$(1.44 \pm 0.13)\%$	28.8
+2%	$(1.56 \pm 0.15)\%$	32.9
-1%	$(1.26 \pm 0.10)\%$	18.2
-2%	$(1.33 \pm 0.09)\%$	68.8
+5%	$(2.50 \pm 0.23)\%$	37.9
-5%	$(1.04 \pm 0.15)\%$	77.4

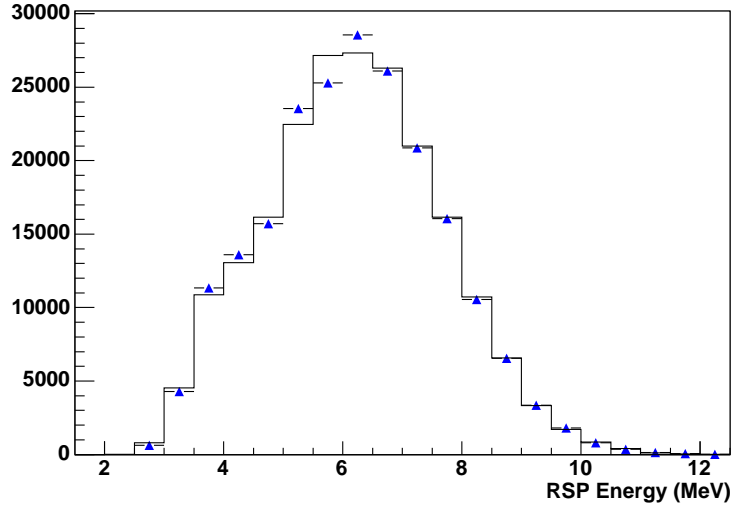


Figure 5.8: Fit to the raw Cf energy spectrum in salt. The points are the Cf data and fit curve is the sum of the neutron energy spectrum, $\frac{dN}{dE_{ns}}$, and the γ energy spectrum, $\frac{dN}{dE_{\gamma}}$, as outlined by equation 5-14. The fit gives a poor χ^2 value which is reflected in the large uncertainty assigned to the derived γ fraction. The fit is poor since it assumes a certain energy scale difference between the interim D_2O phase and the salt phase. This scale is varied and is included in the uncertainty on the γ -fraction. The x-axis label of RSP Energy refers to the total reconstructed energy of the event.

	α	δ
β	0.448	0.182
α		0.869

Table 5.8: Parameter correlation coefficients.

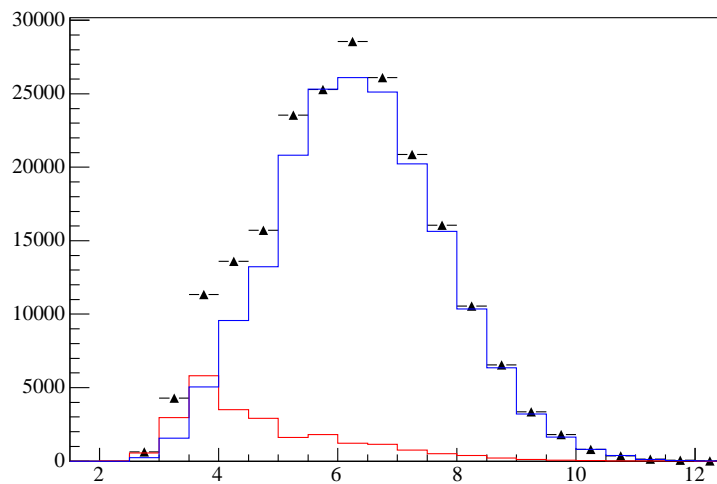


Figure 5.9: The fitted γ energy spectrum, $\frac{dN}{dE_\gamma}$ (red curve), and the fitted neutron energy spectrum, $\frac{dN}{dE_{n.s}}$ (blue curve), that contribute to the fit shown in figure 5.8. The sum of the neutron and γ energy spectra is shown in figure 5.8. The x-axis is the total reconstructed energy of the event and the y-axis are the number of events per 0.5MeV energy bin.

5.6 Final Neutron Detection Efficiency and Comparisons with Monte-carlo

A summary of the final neutron detection efficiency results and a comparison with ^{252}Cf Monte-carlo is shown in table 5.9. The neutron detection efficiency derived from the ^{252}Cf data is in agreement with the Monte-carlo within the uncertainty assigned. Figure 5.10 shows the ^{252}Cf radial efficiency distribution compared to the Monte-carlo of NC neutrons. The shaded region in the figure is the uncertainty on the ^{252}Cf detection efficiency measurement with an additional 1% radial reconstruction uncertainty. The radial reconstruction uncertainty is incorporated in the neutrino flux extraction. It was specifically left out of the neutron detection efficiency measurement to avoid double counting of uncertainties.

	Efficiency
Cf data all corrections	$(40.7 \pm 0.5 \text{ }^{+0.9}_{-0.8})\%$
Cf source at centre (run 21023)	$(55.7 \pm 1.3)\%$
Cf MC at centre (run 21023)	$(55.6 \pm 0.1)\%$
NC MC	$(39.8 \pm 0.1)\%$
Cf data - Cf MC (volume weighted)	-0.2%
Cf data (all corrections) - NC MC	$+2.21\%$

Table 5.9: Monte-carlo and data efficiency results and comparisons. The term 'Cf data (all corrections)' in the last row refers to the volume weighted neutron detection efficiency derived from Cf data after all the corrections listed in table 5.2 have been applied.

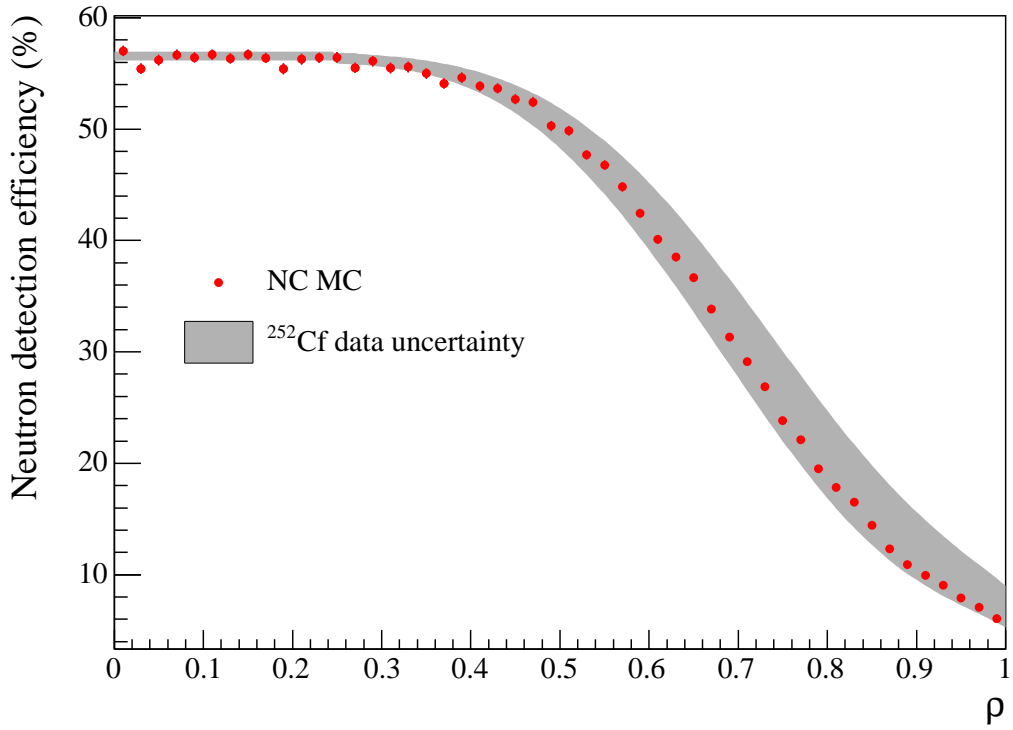


Figure 5.10: Comparison of neutron detection efficiency for Monte-carlo simulated NC events (data points) and that derived from ^{252}Cf calibration data (shaded band) as a function of volume weighted radius, ρ .

5.7 Cf and AmBe Source Comparisons

The $^{241}\text{Am-}^9\text{Be}$ source emits neutrons in coincidence with a 4.4MeV γ -ray. Since neutrons take a while to capture, the 4.4MeV is detected before the neutron. A burst cut similar to that applied to the ^{252}Cf source can be used on the $^{241}\text{Am-}^9\text{Be}$ data to select neutron events. Since there is only one neutron following a 4.4MeV γ -ray, the burst cut has been modified so that only bursts that have exactly one event after the first event in 40msec window are accepted. Figure 5.11 shows a schematic of the burst cut as it is applied to the $^{241}\text{Am-}^9\text{Be}$ data.

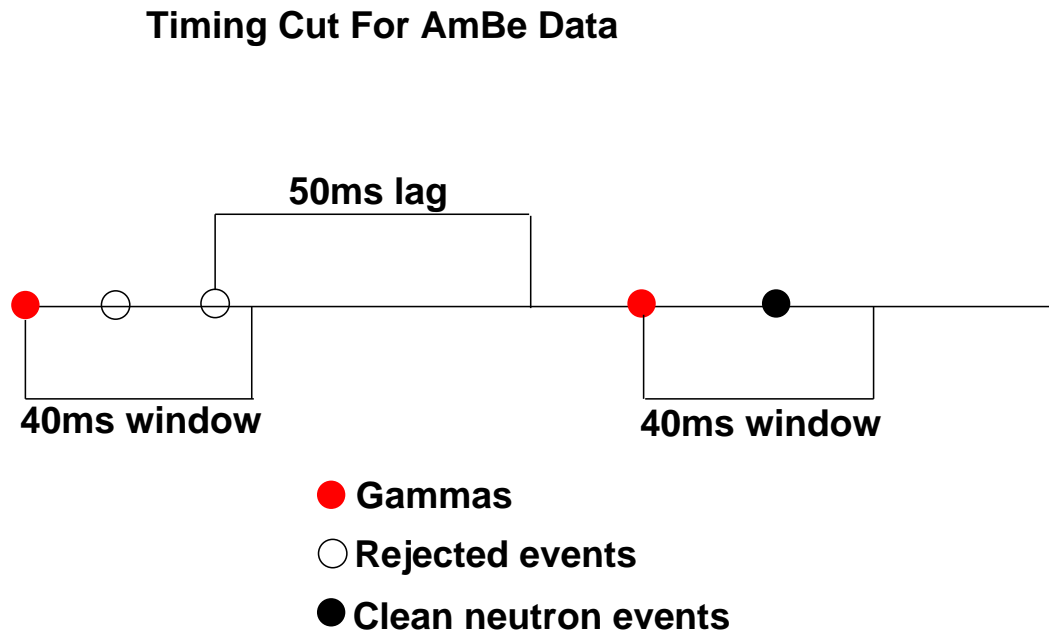


Figure 5.11: Schematic of the burst timing cut used on AmBe data.

The effectiveness of the burst cut on the $^{241}\text{Am-}^9\text{Be}$ data is demonstrated in Fig-

ures 5.12 and 5.13. Figure 5.12 shows the raw $^{241}\text{Am-}^9\text{Be}$ energy as a function of radius for an $^{241}\text{Am-}^9\text{Be}$ run in the centre, and Figure 5.13 shows the same distribution but after the burst cut has been applied. It is clear that the burst cut removes the 4.4MeV γ -ray source background.

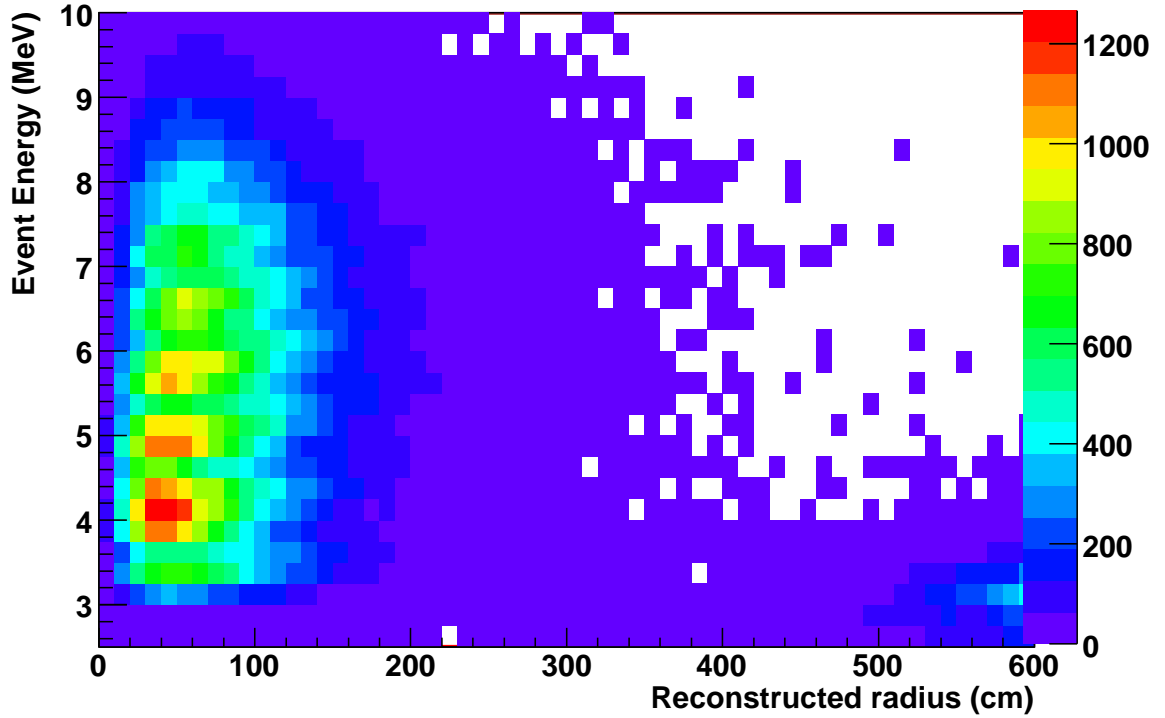


Figure 5.12: Energy as a function of radius for the raw $^{241}\text{Am-}^9\text{Be}$ data before the burst cut is applied for a source at the centre. The low energy events near the source are the 4.4MeV γ -rays from the source. The colour scale represents the number of events per radius-energy bin.

It is hard to get an independent detection efficiency from the $^{241}\text{Am-}^9\text{Be}$ source since the source strength is not known and the ratio of γ -rays to neutrons is only known to within 10%. However it is useful to compare the energy and radial distributions between the two sources to verify the proper selection of neutron events.

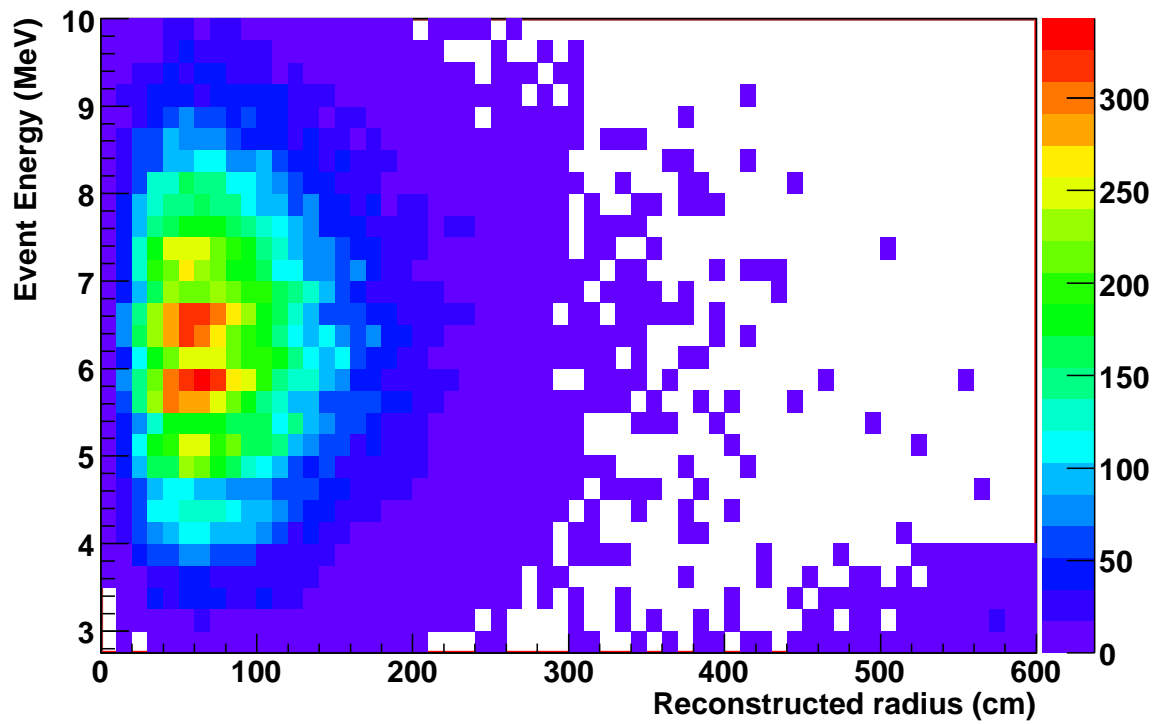


Figure 5.13: Energy as a function of radius for the clean $^{241}\text{Am}-^9\text{Be}$ data after the burst cut was applied for a source at the centre. We notice the absence of low energy events near the source compared to figure 5.12. This is because the burst cut has removed the 4.4MeV γ -rays from the source.

Figure 5.14 shows the comparisons of the energy distributions between the $^{241}\text{Am-}^9\text{Be}$ and ^{252}Cf sources and between $^{241}\text{Am-}^9\text{Be}$ and neutron Monte-carlo. The burst cut has been applied to select neutron events from both sources. A further comparison is shown in Figure 5.15 which shows the normalization between the $^{241}\text{Am-}^9\text{Be}$ neutron energy distribution and the ^{252}Cf and Monte-carlo energy distributions. It is clear from these figures that the events selected by the burst cut are neutrons since a non-neutron γ -ray contribution would show up as a low energy peak.

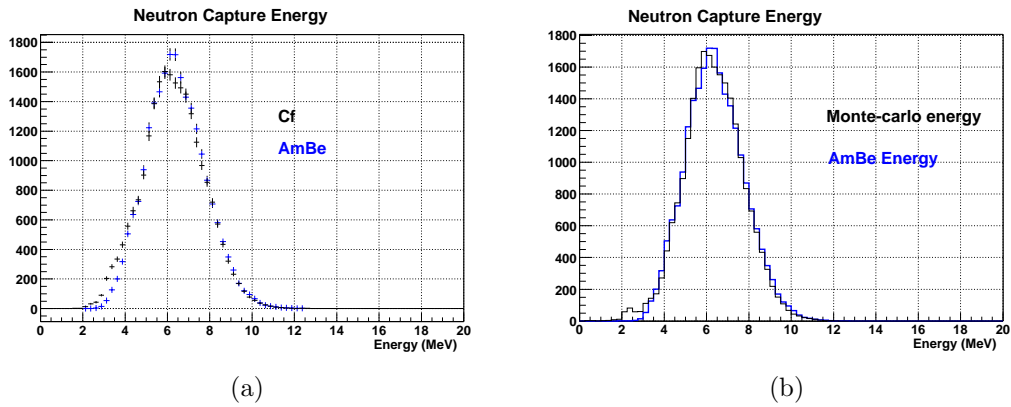


Figure 5.14: Comparison of the selected AmBe neutron energy distribution with the Cf (panel (a)) and Monte-carlo (panel (b)) neutron energy distributions. There is an excess of events below 4MeV in the Cf energy distribution compared to the AmBe distribution. This excess can be attributed to Cf source β and γ backgrounds. There is an apparent excess of events around the peak of the energy distribution for the AmBe data. However from figure 5.15 panel (a) which shows the bin by bin normalization between the AmBe energy data indicates that this excess is just a statistical fluctuation.

The same comparisons as have been done for the energy distributions have also been done for the radial distributions. The γ -rays from the $^{241}\text{Am-}^9\text{Be}$ and ^{252}Cf sources reconstruct closer to the source than the neutrons. Figure 5.16 shows the radial distribution of selected neutron events from the $^{241}\text{Am-}^9\text{Be}$ source with the

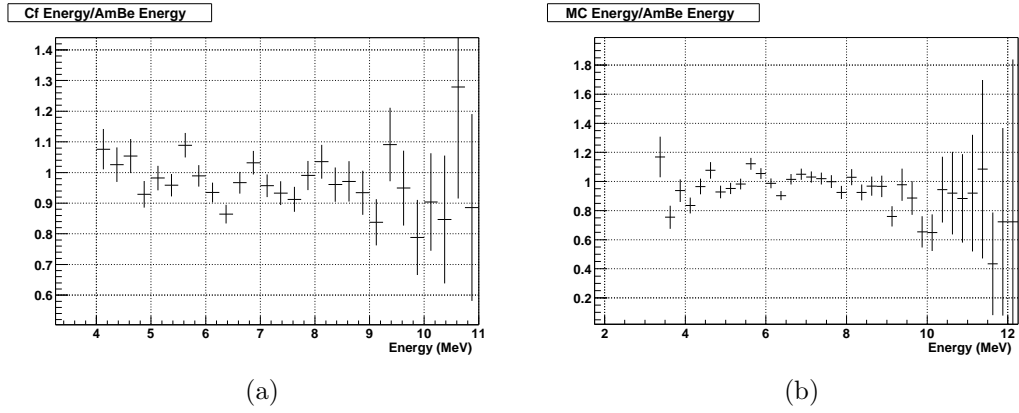
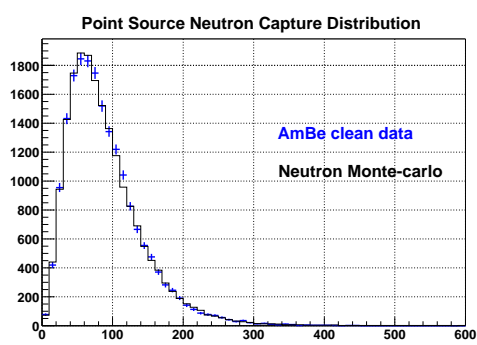
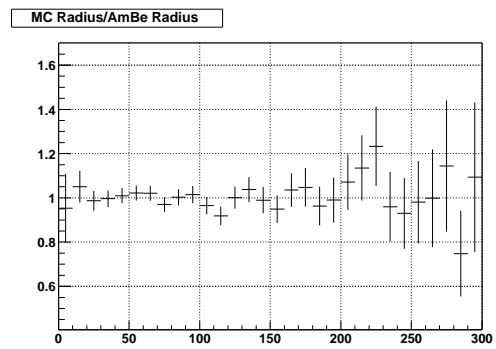


Figure 5.15: The bin by bin normalization between the AmBe neutron energy distribution and the Cf energy distribution (panel (a)), and the normalization with the Monte-carlo neutron energy distribution (panel (b)). The normalization is shown above an energy of 4MeV.

radial distribution of Monte-carlo generated neutrons. Since there is not a significant increase in the number of events that reconstruct close to the $^{241}\text{Am}-^9\text{Be}$ source it can be concluded that the burst cut has removed the source γ -rays.



(a)



(b)

Figure 5.16: Comparison of the AmBe neutron radial distribution with the neutron Monte-carlo (panel (a)) and the bin by bin normalization between the AmBe neutron radial distribution and the neutron Monte-carlo radial distribution (panel (b)).

Chapter 6

Radioactive Backgrounds

The SNO heavy water volume is extremely pure of radioactive backgrounds. Some have even described the centre of the SNO detector as the most radioactive and cosmic ray background free spot in the universe. While this might be an exaggeration, it is very difficult to think of other places where a similarly radio-pure environment naturally exists. This section will focus on the radioactive backgrounds in SNO. There are also cosmic ray backgrounds, muons, and instrumental backgrounds but most of these can be eliminated by low level data-cleaning cuts applied to the data. The radioactive backgrounds in SNO can be classified as external and internal backgrounds. The sources of external background are radioactivity in the AV, the light water, and the PMTs. The internal backgrounds arise from radioactivity in the heavy water. Equation 6-1 lists the contributions to the external and internal backgrounds in the SNO neutrino signal region.

$$B_{ext} = AV_{Bi} + AV_{Tl} + H_2O_{Bi} + H_2O_{Tl} + PMT_{\beta-\gamma}, \quad (6-1.a)$$

$$B_{int} = D_2O_{Bi} + D_2O_{Tl} + D_2O_{Na} \quad (6-1.b)$$

where

AV_{Bi} are the number of events due to Bi activity on the AV,
 AV_{Tl} are the number of events due to Tl activity on the AV,
 H_2O_{Bi} are the number of events due to Bi activity in the light water,
 H_2O_{Tl} are the number of events due to Tl activity in the light water,
 $PMT_{\beta-\gamma}$ are the number of events due to β - γ decays at the PMTs ,
 D_2O_{Bi} are the number of events due to Bi activity in the heavy water,
 D_2O_{Tl} are the number of events due to Tl activity in the heavy water, and
 D_2O_{Na} are the number of events due to Na activity in the heavy water.

A great effort has been taken to minimize the amount of radioactivity so that the neutrino signal region is not dominated by backgrounds. All materials used in the construction of the detector were carefully measured and selected to ensure that they would not provide a significant radioactive background. The "onion skin" design of the detector starts with the most radioactive materials- mine rock and concrete on the outside, then the PMTs and support structure, two meters of pure water shielding, the acrylic vessel, and the heavy water. The levels of uranium and thorium are on the order of parts per million for the rock, parts per billion for the PMTs and support structure, parts per trillion for the AV and parts per 10^{15} for the heavy water. Acrylic from various processors was measured and specially prepared acrylic was chosen to minimize backgrounds. Low radioactivity glass for the PMTs was obtained from Schott glass. Figure 6.1 shows the ^{232}Th and ^{238}U levels in the heavy water volume as a function of time for the entire salt phase running period. SNO is sensitive to all γ -rays that have energies above the Cherenkov threshold and high

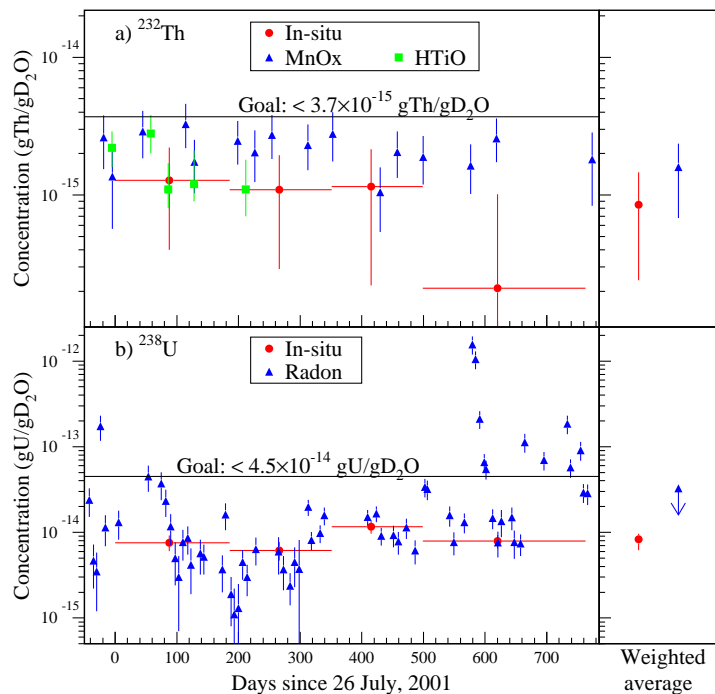


Figure 6.1: Uranium and thorium levels in the the heavy water as a function of time for the salt phase running period. The large increase in the uranium concentration measurements from the radon assays at about 600 days is due to a radon spike that was purposely put in the detector to aid in low energy background calibration.

energy γ -rays can photo-disintegrate deuterium. These can be troublesome since photo-disintegration neutrons are very similar to NC neutrons. SNO is particularly sensitive to γ -rays which are above 2.2 MeV and can therefore disassociate deuterium to produce neutrons. Such γ -rays come from the $\beta - \gamma$ decays of ^{208}Tl , which is part of the ^{232}Th chain, and from $\beta - \gamma$ decays of ^{214}Bi , a daughter of ^{238}U . ^{208}Tl β decays with a total energy of 5MeV with the branch observed by SNO being a 1.8MeV β and the dominant β -delayed γ branch being 2.6MeV. ^{214}Bi decays with a 3.27MeV β with the highest energy subsequent γ being 2.2MeV. Figures 6.2 and 6.3 show the uranium and thorium decay chains giving ^{214}Bi and ^{208}Tl . Another low energy radioactive background is the β decay of ^{24}Na . The ^{24}Na background is unique to the salt phase of SNO since the heavy water in the salt phase obviously contains NaCl. This background arises from neutrons capturing on ^{23}Na producing ^{24}Na . The ^{24}Na decays with a 1.4MeV β followed by two γ -rays of 1.39MeV and 2.75MeV and has a lifetime of 15 hours. Since the probability for a neutron to capture on ^{23}Na is very low, 1 in 380, a large flux of neutrons is required to produce a significant amount of ^{24}Na . These neutrons are produced during calibration running. ^{24}Na can obviously be produced during running of the AmBe and ^{252}Cf neutron calibration sources. However, since the photo-disintegration energy threshold of the deuteron is only 2.2MeV, neutrons can also be produced during running of the ^{238}U , ^{232}Th , and ^{16}N 6.25MeV γ source. Since ^{24}Na has a lifetime of 15 hours, a large fraction of the ^{24}Na background can be eliminated by removing neutrino data that falls in a certain time window after a given calibration run. The length of this time window depends on the calibration source and how long the source was in the detector. In the analysis presented in [1], the 5.5MeV kinetic energy threshold used ensured that very few ^{24}Na background events made it into the neutrino signal window. However, the amount of

^{24}Na photo-disintegration neutrons that remained in the neutrino signal region was calculated and then subtracted from the fitted number of neutral current (NC) events. In the analysis presented in this thesis an energy threshold of 4MeV kinetic energy was chosen. This means a significant number of ^{24}Na $\beta - \gamma$ decays reconstruct within the neutrino signal window. For the lower energy threshold analysis therefore the ^{24}Na background events are extracted using the same signal extraction method as for the neutrino signal. This analysis is described in chapter 8. SNO is sensitive to the Cherenkov light produced by all the $\beta - \gamma$ decay sources listed in equation 6-1. Most of these $\beta - \gamma$ sources will also give rise to photo-disintegration neutrons inside the neutrino signal region. The internal and external photo-disintegration backgrounds are summarized by equation 6-2.

$$N_{ext} = AV_{Bi,n} + AV_{Tl,n} + H_2O_{Bi,n} + H_2O_{Tl,n}, \quad (6-2.a)$$

$$N_{int} = D_2O_{Bi,n} + D_2O_{Tl,n} + D_2O_{Na,n} \quad (6-2.b)$$

where the subscript n denotes the photo-disintegration neutron arising from the corresponding $\beta - \gamma$ decay. There is no neutron component from the PMT background since the γ -rays from the $\beta - \gamma$ decays in the PMT material do not make it inside the heavy water volume. The internal photo-disintegration neutron background is indistinguishable from the NC signal and is determined from measuring the number of decays from the $\beta - \gamma$ backgrounds listed in equation 6-2 and then using the photo-disintegration cross-section to determine the number of neutrons produced. For the internal background sources listed in equation 6-2 approximately 1 in every 300 γ -rays above the photo-disintegration threshold will produce a neutron.

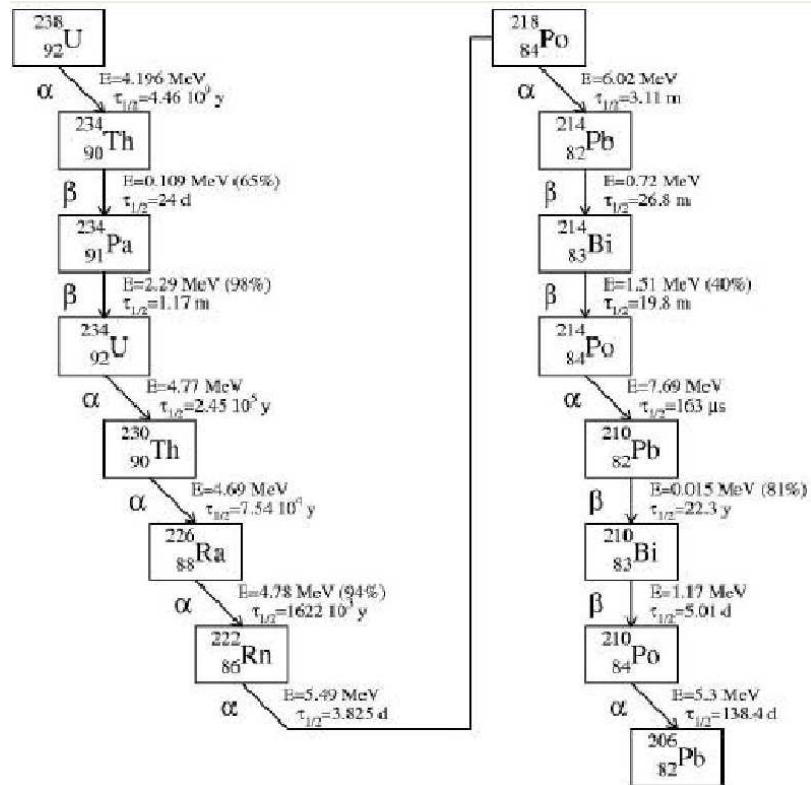


Figure 6.2: Radioactive chain of ^{238}U . The background that SNO is particularly sensitive to comes from the ^{214}Bi β decay.

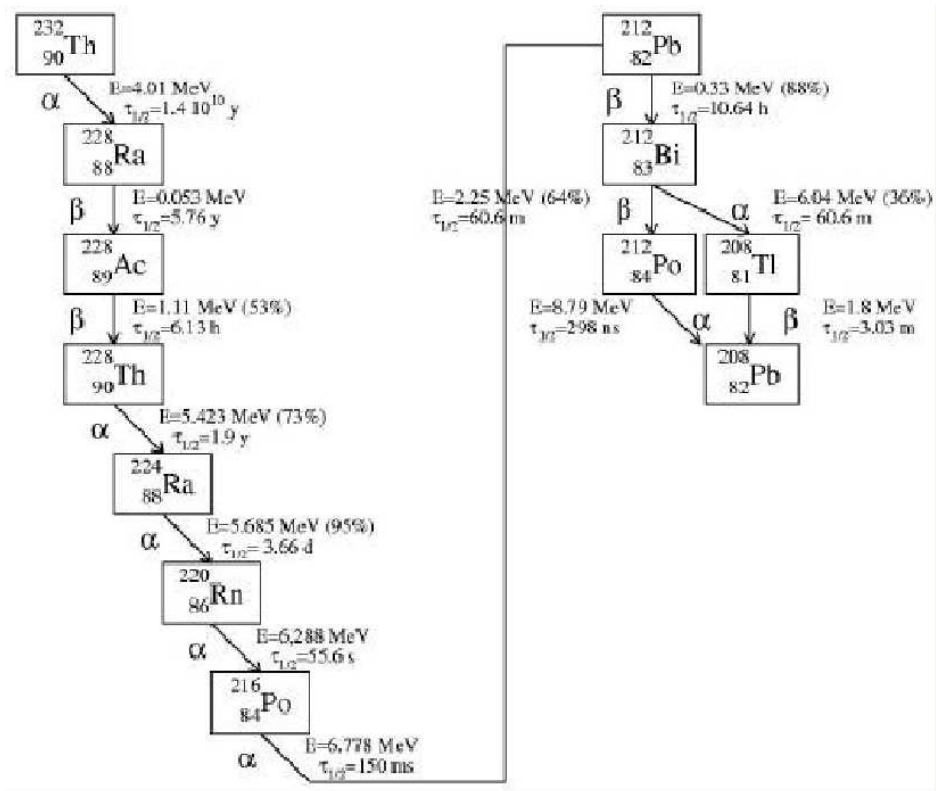


Figure 6.3: Radioactive chain of ^{232}Th . The background that SNO is particularly sensitive to comes from the ^{208}Tl β decay.

6.1 Background Measurement Techniques

There are two methods by which the radioactive backgrounds are measured in SNO. The first method is to fit for the number of ^{214}Bi and ^{208}Tl decays in the neutrino data using the β_{14} isotropy parameter, described by equation 4-1, in an energy window of 4.0 to 4.5MeV. In the 4.0 to 4.5MeV energy window, ^{214}Bi primarily decays through a 3.27MeV β to the ground state where as ^{208}Tl decays with a 1.8MeV β followed by a 2.6MeV subsequent γ . Since ^{214}Bi is a single particle β decay and ^{208}Tl is a β - γ decay ^{208}Tl will have a more isotropic hit pattern than ^{214}Bi . Determining the background level by extracting its level from the data is known as the *in-situ* method for determining radioactive background. For the analysis published in [1], a 5.5MeV threshold was used so the background analysis window of 4.0 to 4.5MeV is outside the neutrino analysis window. The number of background events found in the background window was then extrapolated into the neutrino analysis window using the energy distribution of the ^{214}Bi and ^{208}Tl backgrounds. In the analysis presented in this thesis the neutrino analysis threshold is set at 4MeV, and the backgrounds to the neutrino signal are fitted for along with the neutrino signals themselves. Therefore the *in-situ* method used for the lower energy threshold analysis is fundamentally different from the previous *in-situ* method in that the same data needs to be used for the neutrino analysis and the background extraction. Both the neutrino signal extraction and the background extraction are described in chapter 8.

A second method is called the *ex-situ* analysis and involves measuring the uranium and thorium concentrations in the light and heavy water externally to the detector volume. In the *ex-situ* analysis, the isotopic impurities are extracted from the water by a variety of chemical techniques, purified, and the decays of the radium and radon

parent isotopes to ^{214}Bi and ^{208}Tl are counted externally to the SNO detector. The ^{224}Ra and ^{226}Ra are extracted using beads coated with manganese oxide, MnO_x , or membranes loaded with hydrous titanium oxide, HTiO . The ^{224}Ra and ^{226}Ra are then extracted from the beads and counted in an electrostatic chamber [23]. For the technique involving MnO_x , radon daughters from the radium decays are identified and counted using α spectroscopy. In the technique using HTiO , a $\beta - \alpha$ coincidence is used to tag the daughters of the radium atoms. Over the entire salt running period, 16 MnO_x and 6 HTiO assays were done. From these techniques the concentration of ^{232}Th was determined to be $(1.76 \pm 0.44 \text{ (stat.)}_{-0.94}^{+0.70} \text{ (sys.)}) \times 10^{-15} \text{ gTh/gD}_2\text{O}$ in the heavy water [1]. The Monte-carlo calculations based on these background levels find that for a 4MeV energy threshold and a 550cm fiducial volume this corresponds to 270 ± 170 background events due to ^{208}Tl in the neutrino data. This number includes photo-disintegration neutrons. This number is added as a constraint on the number of extracted ^{208}Tl events in the neutrino signal extraction described in chapter 8. The *ex-situ* techniques only give an upper limit on the ^{238}U concentrations and therefore also on the number of events due to ^{214}Bi in the neutrino signal. Therefore the number of ^{214}Bi events that are in the neutrino signal region are fitted for along with the neutrino signals and other backgrounds. The concentration of ^{238}U and ^{232}Th is much higher in the light water than in the heavy water. In addition to the MnO_x and HTiO techniques, an additional radon assay technique is used to assay the ^{238}U and ^{232}Th concentrations in the light water. For the radon assay, water is taken from sample points in the light water volume. This water is then degassed to remove the radon. The radon is then purified and collected in a cryogenic collector. The α decays are then counted in a Lucas cell scintillator, ZnS , using a PMT [24]. During the salt running period 86 radon assays, 30 MnO_x , and 13 HTiO assays were

performed. The measured concentration of ^{238}U is $20.6 \pm 5.0 \times 10^{-14}\text{gU/gH}_2\text{O}$ and of ^{232}Th it is $5.2 \pm 1.6 \times 10^{-14}\text{gTh/gH}_2\text{O}$. Even though these backgrounds are in the light water, a substantial number of backgrounds are misreconstructed inside 550cm. For a kinetic energy threshold of 4MeV and for a 550cm fiducial volume the *ex-situ* ^{238}U and ^{232}Th measurements correspond to 101 misreconstructed ^{208}Tl events and 522 misreconstructed ^{214}Bi events. Events in the external light water can also be fitted for relatively easily when extracting the neutrino signal since the radial profile of the external backgrounds is much different than the neutrino signals and the internal heavy water backgrounds. Figure 6.4 shows the normalized radial distributions, ρ , of the three neutrino signals and the external H_2O ^{214}Bi and ^{208}Tl backgrounds. The internal backgrounds are not shown but have a similar radial profile to the neutrino signals. Since the radial distributions of the external backgrounds are much different than the neutrino signals the external backgrounds are easily fitted for along with the neutrino signals.

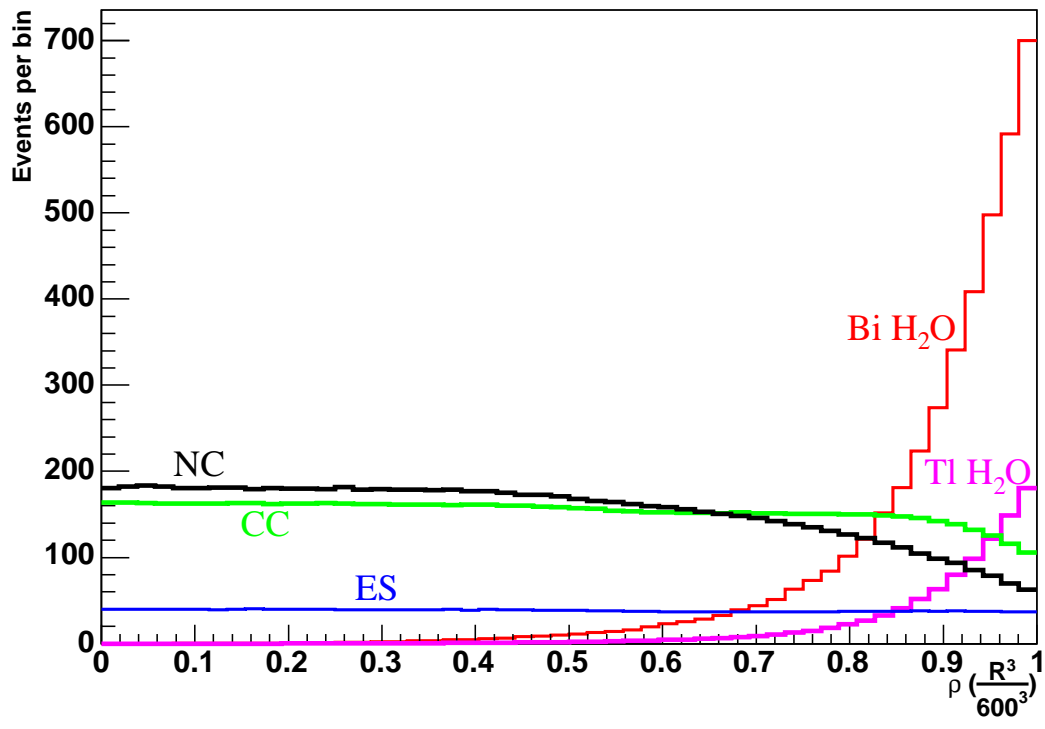
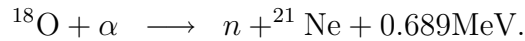
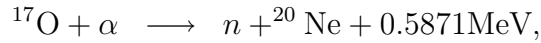
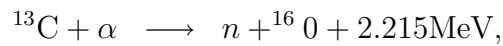
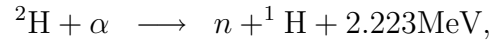


Figure 6.4: The normalized radial distributions for the three neutrino signals and the ^{214}Bi and ^{208}Tl external backgrounds. The shapes of the external background distributions includes the contribution from photo-disintegration neutrons. The radial distributions are for a 4MeV energy threshold.

6.2 Other Sources of Background

Neutrons can also be produced in the SNO detector from the (α, n) reaction. They arise mostly from α emitting isotopes from the uranium and thorium chain that were deposited on the AV during the construction phase of the experiment. Neutrons can be produced through the (α, n) reaction through the following processes:



All 14 of the α emitters in the uranium and thorium chains give α energies that are high enough to produce (α, n) reactions. In the heavy water, ${}^{222}\text{Rn}$ is the main source of (α, n) neutrons. However the contribution to the neutron background from the (α, n) reaction is negligible compared to the AV (α, n) reactions. It is believed that the AV may have accumulated radon daughters through electrostatic attraction [25]. Acrylic, $(\text{C}_5\text{H}_8\text{O}_2)_n$, can facilitate (α, n) reactions through its C and O targets. Very few of the neutrons actually produced in the AV actually make their way inside a fiducial volume of 550cm since the neutron capture cross sections are very high for acrylic and light water compared to heavy water. However, compared to the number of expected NC neutrons the AV (α, n) background is significant and must be accounted for.

One way to tag the (α, n) reactions is to look for a coincidence between the neutron capture and any γ -rays produced in the reaction. The ${}^{17}\text{O}$ and ${}^{18}\text{O}$ (α, n) reactions

can be followed by 2.2 and 2.7MeV γ -rays respectively. To look for these coincidences one has to demand that the second event falls within 40msec of the first event, the maximum time to capture for a neutron in salt. Since these γ -rays are relatively low in energy, only a fraction of these events reconstruct above SNO's energy threshold. The $^{13}\text{C}(\alpha,n)^{16}\text{O}$ reaction however has an excited state of ^{16}O at 6.05MeV that can be excited by ^{210}Po α particles. The 6.05MeV excited state of ^{16}O decays via a e^+e^- pair. It is also possible to excite the 6.13MeV state of ^{16}O which then decays through a γ . The energy response is easier to understand for a single γ than an e^+e^- pair but only 1.6% of the reactions excite the 6.13MeV state. Another way to look for a coincidence is in the $^2\text{H}(n,2n)^1\text{H}$ reaction. The threshold for this reaction is 3.3MeV and the (α,n) reactions usually produce fast neutrons. The $^{13}\text{C}(\alpha,n)^{16}\text{O}$ reaction for example can produce neutrons up to energies of 7.3MeV. The cross section for $(n,2n)$ however is quite low compared to simple elastic scattering on the deuteron, and the neutron energy will quickly go below the 3.3MeV $(n,2n)$ threshold as they elastic scatter. Overall the coincidence method provides an estimate on the number of (α,n) neutrons that is in agreement with other methods [26]. It is difficult however to model the energy response to the e^+e^- pair near the AV so converting the coincidence measurement to an (α,n) neutron number is hard. From the analysis done in [26], the production rates of neutrons, R_n , electron pairs, R_π , and 6.13MeV γ -rays by the (α,n) reactions are

$$R_n = \frac{1}{2}A_i(Y_{acrylic} + Y_{HW}) + \frac{1}{2}A_o(Y_{acrylic} + Y_{LW}) + A_B Y_{acrylic}, \quad (6-3.a)$$

$$R_\pi = 0.774B_\pi Y_{acrylic} \left[\frac{A_i + A_o}{2} + A_B \right], \quad (6-3.b)$$

$$R_\gamma = 0.774B_\gamma Y_{acrylic} \left[\frac{A_i + A_o}{2} + A_B \right] \quad (6-3.c)$$

where

- A_i is the alpha activity on the inner surface of the AV,
- A_o is the alpha activity on the outer surface of the AV,
- A_B is the alpha activity in the bulk of the AV,
- B_π is the branching ratio for the 6.05MeV state,
- B_γ is the branching ratio for the 6.13MeV state,
- $Y_{acrylic}$ is the neutron yield from the acrylic,
- Y_{HW} is the neutron yield from the heavy water, and
- Y_{LW} is the neutron yield from the light water.

The factor of $\frac{1}{2}$ is due to the activity going inward or outward from the AV. The factor of 0.774 in the R_π and R_γ equations relates to the fraction of the neutron yield due to ^{13}C . The rate of measured neutron and electron pair coincidences can then be expressed as

$$R_{n\pi} = R_n D_n D_\pi P(\pi : n) \quad (6-4)$$

where D_n and D_π are the detection efficiencies of the neutron and electron pairs and $P(\pi : n)$ is the probability for making a pair if a neutron is produced. Similarly, the neutron and 6.13MeV γ -ray coincidence rate is

$$R_{n\gamma} = R_n D_n D_\gamma P(\gamma : n). \quad (6-5)$$

Coincidence events can also be produced through the $^2\text{H}(n, 2n)^1\text{H}$ reaction. The detection rate for these coincidences is

$$R_{nn} = R_n (D_n)^2 P(2n : n). \quad (6-6)$$

The detection efficiency can be broken up into three components,

$$D_i = F_i I_i S_i \tag{6-7}$$

where the index i represents a neutron, γ -ray, or an electron pair, and F_i is a fiducial volume factor, I_i is the detectable interaction probability, and S_i is the detection probability associated with applying an energy threshold. For γ -rays and electron pairs I_i is 1 and for neutrons I_i is the capture efficiency which is significantly less than 1 near the AV. Table 6.1 lists the neutron capture efficiencies for neutrons generated on the inner surface of the AV, the AV bulk, and on the outer surface. These efficiencies exclude energy threshold cuts.

	Inner surface	AV bulk	Outer surface
Efficiency	0.476	0.342	0.219

Table 6.1: Neutron capture efficiency on the inner surface, bulk, and outer surface of the AV.

The number of (α ,n) neutrons determined from the coincidence analysis done in [26] is 94 ± 32 .

Direct α counting on the AV has been done by Hugh Evans, a professor at Queen’s University and SNO collaboration member. An acrylic plate that is used to cover one of the gate valves in the detector control room was used for the α counting. This plate has been underground since November 1999, about the same time as the rest of the AV. The α counting technique gives an upper limit of 129 (α ,n) neutrons in the salt data set [25]. This is in agreement with the coincidence measurement. There has also been a measurement of the α rate in the neck of the AV below and above the water level. The measured α rate below the water level is 1.8 ± 0.5 per cm^2 per

day and above the water level it is 9.2 ± 0.9 per cm^2 per day. Using equation 6-3 for the neutron rate and a neutron yield from carbon of $Y_c = 1.0 \times 10^{-7}$ and neutron yield from oxygen of $Y_o = 6.0 \times 10^{-8}$ this translates into 54 to 273 neutrons in the salt data set depending on what α rate is chosen. This range is in agreement with other methods. It is not known whether the activity on the AV was dissolved in the water or if the activity from the air was deposited on the AV.

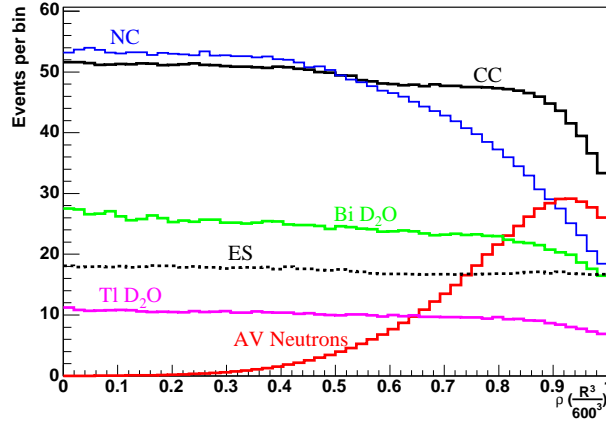
6.3 Fitting for External Backgrounds

The ^{238}U and ^{232}Th concentrations in the light and heavy water can be measured externally to the SNO detector as done in the *ex-situ* analysis. For the external neutron backgrounds the coincidence method and the α counting methods were discussed. In this section we will discuss the fitting for the external backgrounds using the neutrino data. For the analysis in this thesis the backgrounds are fitted for along with the neutrino signal in a maximum likelihood signal extraction. We will start with the description of the fit for the external neutrons using the neutrino data.

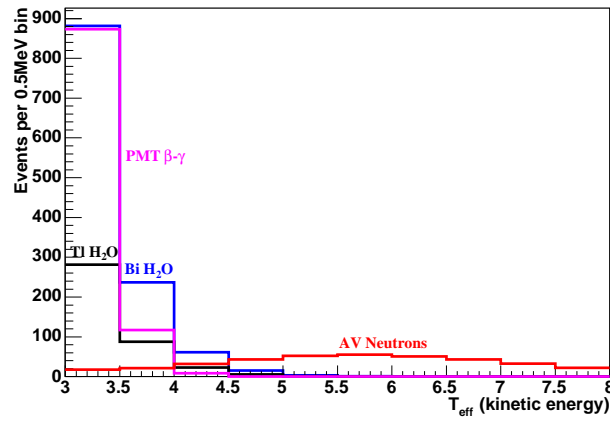
A direct fit for the number of external neutrons has been done on the salt neutrino data. This is the method used in the neutrino analysis presented in this thesis. Fitting for the (α, n) neutrons in the neutrino data provides the most direct and accurate measure of the (α, n) neutron contamination. First done by Mark Boulay in [27], the external neutron fit has been re-done on the reprocessed salt data set with the number of $\beta - \gamma$ events from the ^{214}Bi and ^{208}Tl backgrounds used as constraints in the fits. A maximum likelihood technique is used to do a signal extraction on the neutrino data to extract the number of (α, n) neutrons as well as the other background contributions. Monte-carlo calculations are done to generate the probability

distribution functions, PDFs, that are used to extract the signals. A full description of the maximum likelihood technique and how it is applied to extract the neutrino and background signals is given in chapter 8. The success of the (α,n) neutron signal extraction depends on the fact that the external neutron Monte-carlo radial PDF is very much different than the internal heavy water backgrounds and NC signal, and that the energy and β_{14} external neutron distributions are different than the other external backgrounds. Figure 6.5 shows the radial and energy distributions of neutrons produced on the bulk of the AV that capture in the heavy water. Neutrons produced by the (α,n) reaction on the AV have the same distributions. It is clear that the radial distribution of the AV neutrons gives good separation against the internal backgrounds and neutrino signals. Since the neutron capture energy response peaks around 6.3MeV, see chapter 5, AV neutrons are separated from the other external backgrounds based upon their energy distributions since these other backgrounds peak at much lower energies.

The external neutrons were fitted for in the radial region between 550 and 600cm. Various energy thresholds were used to check the stability of the fit. Table 6.2 shows the fitted number of AV neutrons in the neutrino data for various energy thresholds. The lowest energy threshold used is 5MeV so that most of the $\beta - \gamma$ backgrounds are removed. For comparison purposes, the results shown are the fit results extrapolated to a radial region within 550cm and an energy threshold of 5.5MeV kinetic energy. The number of external neutrons are extracted using external neutron distributions generated from a Monte-carlo calculation and from ^{252}Cf data. The ^{252}Cf data used to generate the external neutron distributions were ^{252}Cf runs in which that source was touching the AV. This is not the same as the Monte-carlo, which is neutrons generated in the bulk of the AV. The ^{252}Cf source was deployed touching the inside



(a) normalized radius



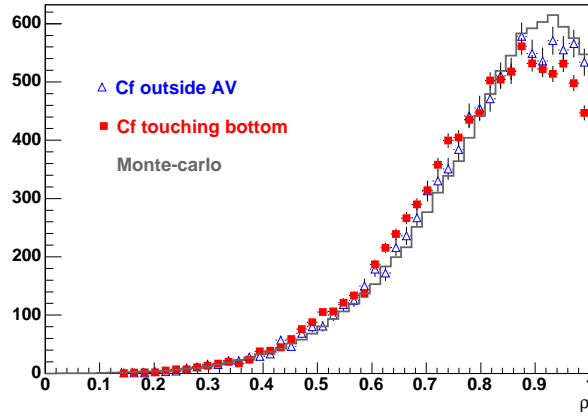
(b) kinetic energy

Figure 6.5: Comparison of the radial distribution (panel a) and energy distribution (panel b) of the AV neutrons to the neutrino signals and backgrounds.

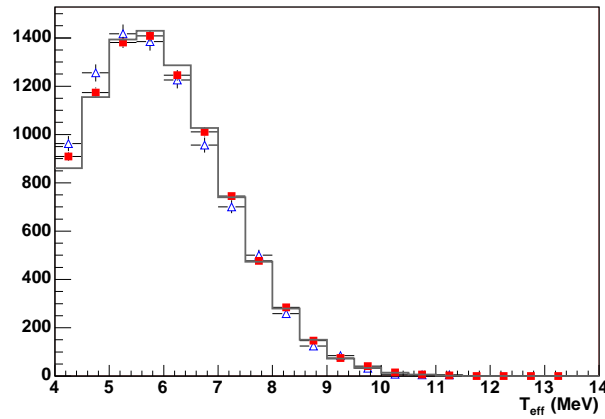
of the AV at the bottom and touching the top of the AV in the light water. Table 6.2 shows the number of fitted external neutrons is in agreement when either the Monte-carlo generated distribution or the distributions generated from the ^{252}Cf source on the inside of the AV are used. If the ^{252}Cf source on the outside of the AV is used then number of fitted external neutrons is less than half of the number fitted for the source on the inside. Table 6.1 indicates that the neutron capture efficiency on the outside of the AV is less than half of the capture efficiency on the inside. This is in agreement with the fit result. Figure 6.6 shows a comparison between the the radial and energy distributions generated from Monte-carlo and ^{252}Cf data. While slightly different, the distributions are not different enough to give drastically different results in the number of fitted neutrons. The fitted number of external neutrons is used to constrain the number of external neutrons inside 550cm for the neutrino signal extraction.

Energy Threshold	Monte-carlo PDF	^{252}Cf inside	^{252}Cf outside
5MeV	153 ± 37	—	—
5.5MeV	144 ± 44	150 ± 49	70 ± 35
6MeV	173 ± 49	142 ± 48	67 ± 43

Table 6.2: Number of fitted external AV neutrons for various kinetic energy thresholds. The left column of numbers is the extracted number of external neutrons when a Monte-carlo calculation is used to generate the AV neutron distributions. The middle column is the fitted number of external neutrons when the ^{252}Cf neutron calibration source touching the inside of the AV is used to generate the external neutron distributions. The right column is the fitted number of external neutrons when the ^{252}Cf neutron calibration source touching the outside of the AV is used to generate the external neutron distributions.



(a) normalized radius



(b) kinetic energy

Figure 6.6: Comparisons of energy (panel b) and radial (panel a) distributions between the external neutron Monte-carlo, ^{252}Cf outside the AV, and ^{252}Cf touching bottom. The energy thresholds used in the fit for external neutrons are 5MeV, 5.5MeV, and 6MeV. The energy threshold for both these plots is 4MeV.

The most obvious way to fit for the external backgrounds is to use their radial distributions since the radial distributions for the external backgrounds are much different than the internal backgrounds or neutrino signals. The external backgrounds are fitted for along with the neutrino signals using the radial distributions as the primary separator, this analysis is shown in chapters 8 and 9. However, separation between PMT $\beta - \gamma$ events and other external backgrounds cannot be done using the radial distributions alone since the radial distribution of the PMT $\beta - \gamma$ events are similar to the rest of the external backgrounds. To separate between the PMT $\beta - \gamma$ events and the other external backgrounds the PMT isotropy parameter, β_{14} , is mostly used. Events near or at the PMTs have a different isotropy distribution than the other external backgrounds since the Cherenkov light from these events is reflected off the PMT glass differently than the light water background events. Figure 6.7 shows the β_{14} distributions for the light water ^{214}Bi and ^{208}Tl external backgrounds compared to the PMT $\beta - \gamma$ background. The higher the β_{14} value the less isotropic the event.

It is useful to extract the external backgrounds outside the neutrino signal region and then use the estimated backgrounds as a constraint in the neutrino fit. This reduces the uncertainty on the external backgrounds and since the number of fitted neutrino events are somewhat correlated to the fitted number of background events this also reduces the uncertainty on the neutrino signals.

In the salt phase of SNO the isotropy distribution of the PMT hit pattern for events is one of the distributions used to extract the signals. The β_{14} parameter is used as a measure of the isotropy. For the neutrino signal region the β_{14} parameter is chosen to be between -0.12 and 0.95. This window was chosen so that a large fraction of the misreconstructed background events would be cut but most of the

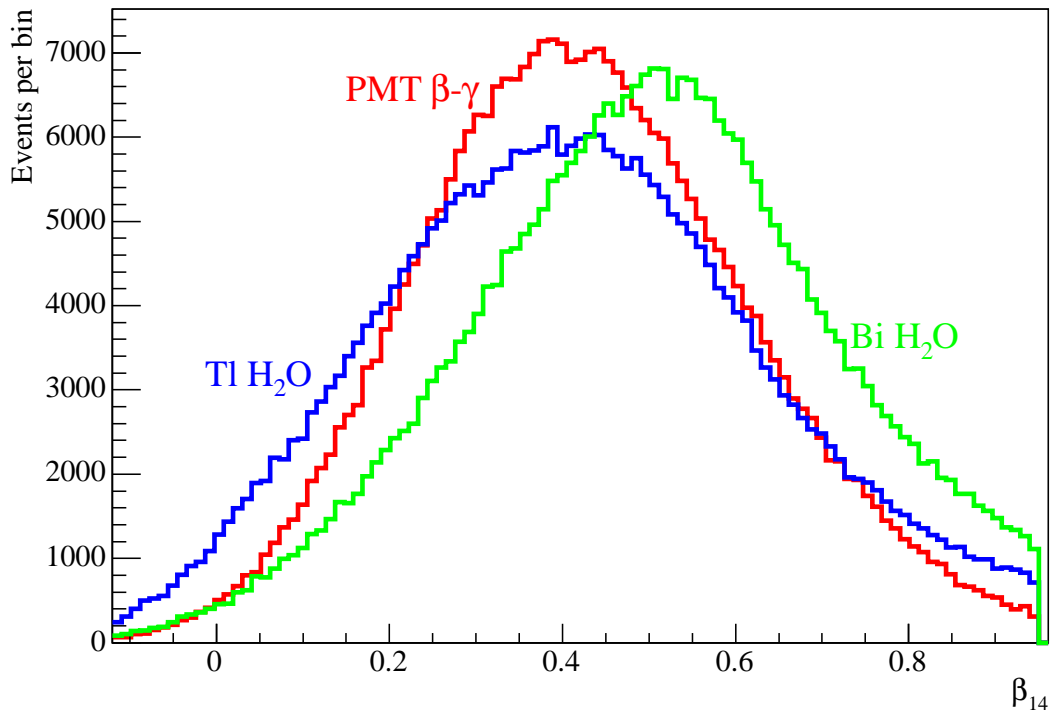


Figure 6.7: β_{14} distributions of the ^{214}Bi and ^{208}Tl H₂O backgrounds compared to the PMT $\beta - \gamma$ background.

neutrino events would still remain. The β_{14} parameter is defined such that the higher the β_{14} value the less isotropic the event. The external background β_{14} distributions have long tails at the high end of the β_{14} scale that extend past 0.95, as shown in figure 6.9. The high β_{14} values for the external backgrounds arise from events that misreconstruct inside the D₂O volume instead of outside the AV where the event actually occurred. The misreconstructed events have the same PMT hit pattern as the events that originate outside the AV but since they reconstruct in the D₂O the Cherenkov light appears to be much narrower and so is less isotropic. Figure 6.8 shows a schematic representation of this effect.

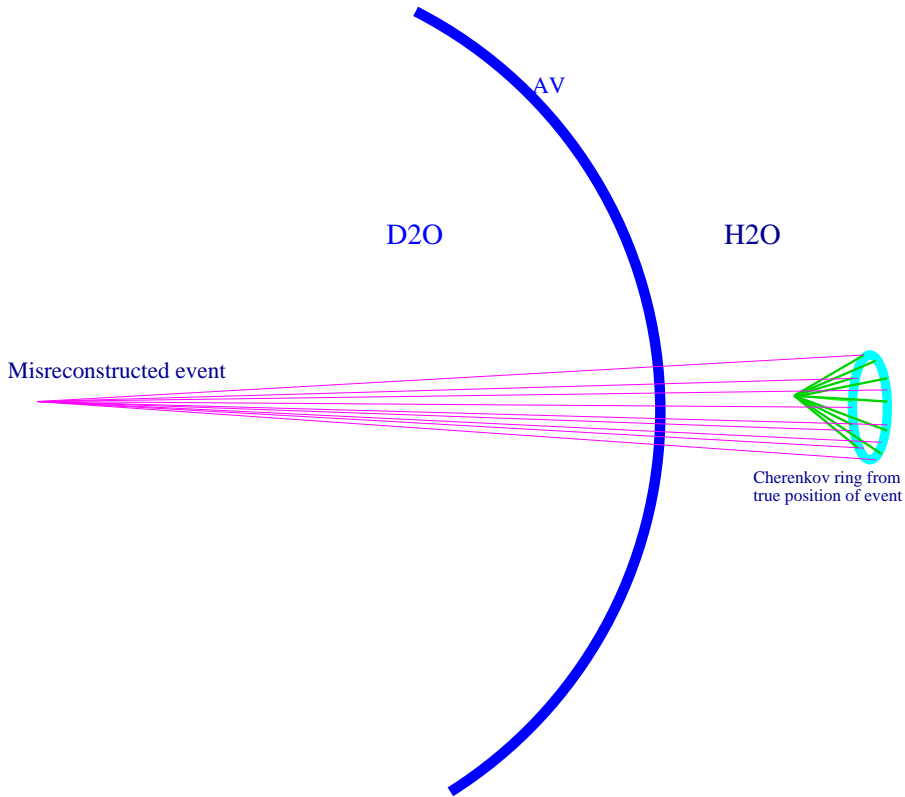


Figure 6.8: Schematic of the Cherenkov light cone for a misreconstructed event compared to the light cone for the same event that reconstructs in the correct position. The light cone for the misreconstructed event is much narrower and therefore has a lower isotropy and a higher β_{14} value.

The neutrino data set has been fit in the high β_{14} region between 0.95 and 2.0 to extract the number of external backgrounds. The external backgrounds that are extracted are Bi and Tl in the H_2O and the AV, and the PMT $\beta - \gamma$'s. Monte-carlo PDFs are use for the AV and H_2O backgrounds and Thorium source runs near the PMTs are used to generate the PMT $\beta - \gamma$ PDF. Figures 6.9 and 6.10 show the β_{14} and radial distributions for external background PDFs in the β_{14} region of 0.95 to 2.0. The radial distributions shown in figure 6.10 are different than the external background radial distributions for the neutrino signal window.

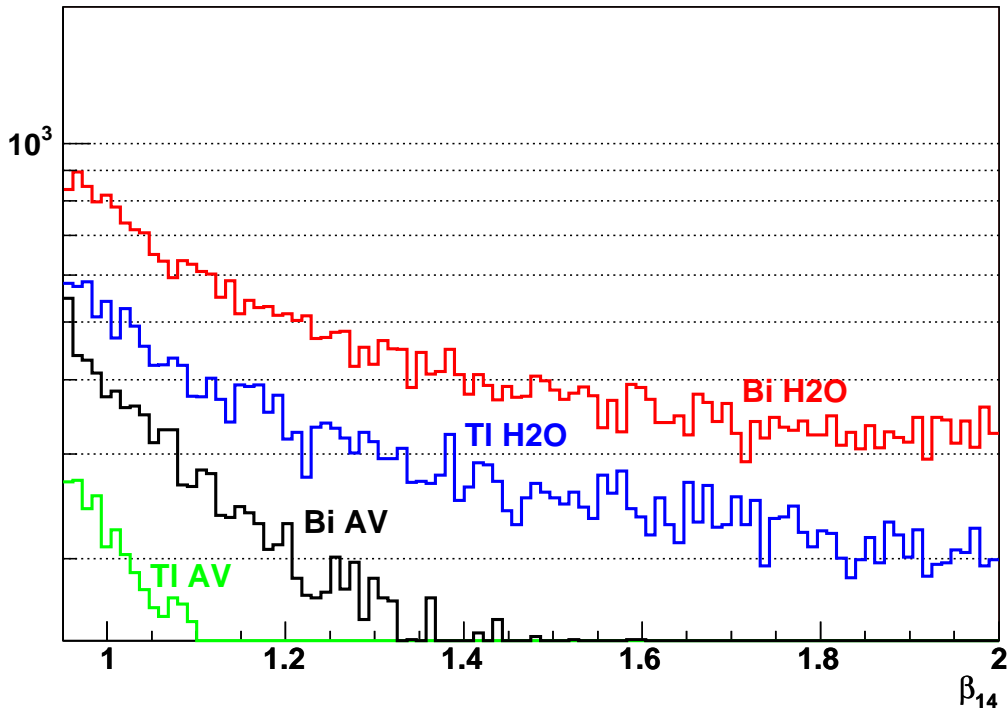


Figure 6.9: The β_{14} tail distributions for the external backgrounds.

The distributions used to fit for the external backgrounds in the high β_{14} tail region are generated through Monte-carlo calculations. To verify the Monte-carlo, calibration data from a radon spike in the H_2O is used.

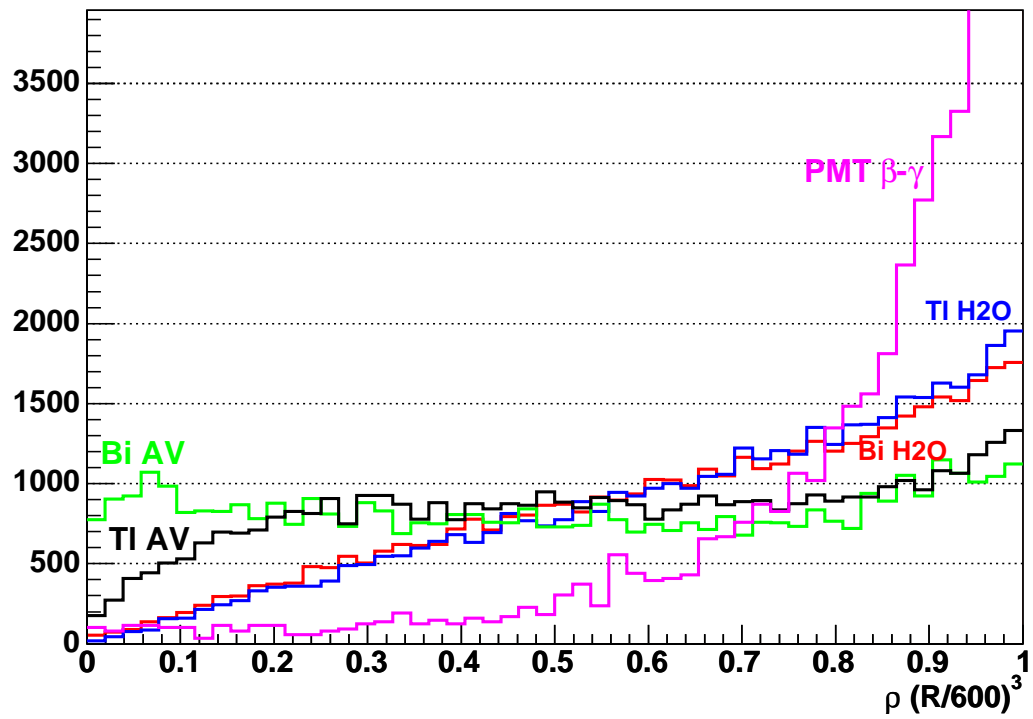


Figure 6.10: Radial distributions of the external backgrounds for events that have a β_{14} value between 0.95 and 2.0 from Monte-carlo.

Table 6.3 summarizes the results from the β_{14} tail fit. As a comparison the Bi and Tl H₂O numbers from the low energy background analysis [24] are also shown.

	High β_{14} Fit	Low Energy Background
Bi H ₂ O	459 ± 56	522 ± 264
Tl H ₂ O	135 ± 16	101 ± 57
Bi AV	159 ± 50	—
Tl AV	308 ± 80	—
PMT	216 ± 72	—

Table 6.3: Extracted number of external backgrounds after fitting in the β_{14} tail region. The number of events are normalized to a 550cm fiducial volume, an energy threshold of 4MeV kinetic, and the normal β_{14} region of -0.12 to 0.95. The high β_{14} fit refers to the external background fit done in the β_{14} tail region of 0.95 to 2.0 and the numbers in the low energy background column refer to the results obtained from the measurements made by the low energy background group [24].

Chapter 7

The Neutrino Signals in SNO

SNO is only sensitive to the ${}^8\text{B}$ and hep neutrinos from the sun. However the ${}^8\text{B}$ flux is a factor of about two thousand times higher than the hep flux, therefore for the analysis presented here the input to the Monte-carlo is the ${}^8\text{B}$ neutrino energy spectrum as calculated by the standard solar model (SSM). The ${}^8\text{B}$ spectrum used for the SNO analysis is taken from Ortiz et al. [28]. The neutrino-electron and neutrino-deuteron cross sections are taken from an effective field theory (EFT) calculation done in [29]. The EFT calculation gives an uncertainty on the neutrino-deuteron cross section of 3%. This uncertainty has to be included when converting from the extracted number of neutrino events to an absolute neutrino flux.

7.1 The Neutral Current Interaction in the Salt Phase of SNO

SNO can detect all flavours of neutrinos through the neutral current (NC) interaction on deuterium,



This interaction has a threshold of 2.224MeV so it is usually initiated by the ${}^8\text{B}$ solar neutrinos with a small contribution from the hep neutrinos. The reaction is detected by detection of the outgoing neutron. In the pure D_2O phase, the neutron captured predominantly on ${}^2\text{H}$ producing an ${}^3\text{H}$ in an excited state. The ${}^3\text{H}$ then de-excites with emission of a 6.25MeV γ -ray which then can Compton scatter electrons. The electrons above the Cherenkov threshold then emit Cherenkov light which is detected by the PMTs. The average Cherenkov light produced by the electrons corresponds to about 5.5MeV. This is less than the energy of the de-excitation γ -ray because some of the scattered electrons will have energies below the Cherenkov threshold of 0.750MeV. The Cherenkov light produced in the NC interaction has no dependence on the direction of the neutrino.

For the pure D_2O phase running period the extracted number of neutrino events for the three signals were 1967.7 CC events, 263.6 ES events, and 576.5 NC events [12]. Therefore in pure D_2O phase the NC signal was statistically limited compared to the CC signal. In June of 2001 salt, about two tonnes of NaCl, was added to the heavy water volume to give a concentration of 0.002 g(NaCl)/g(D_2O). The neutron capture cross section of ${}^{35}\text{Cl}$ is much higher than that of ${}^2\text{H}$, 44mb compared to 0.5mb and the sensitivity of SNO to the NC interaction was increased by a factor of 3 compared to the pure D_2O phase. Neutron capture on ${}^{35}\text{Cl}$ produces an excited state of ${}^{36}\text{Cl}$ which then decays with a cascade of γ -rays with a maximum total energy of 8.6MeV. The energies of the γ -rays with the highest relative intensity are shown in table 7.1.

E_γ (MeV)	I (%)
1.164	27.7
1.601	3.5
1.951	20.2
1.959	12.9
2.863	6.6
3.067	3.9
4.979	3.6
5.715	5.6
6.110	20.2
6.619	7.8
6.627	4.8
7.413	10.4
7.790	8.5

Table 7.1: γ -ray energies from the reaction $^{35}\text{Cl}(n,\gamma)$. Shown are only the highest intensity γ -rays (above 3%). The full cascade has over a hundred possible γ -rays.

7.2 The Charged Current Interaction in the Salt Phase of SNO

The CC interaction is only sensitive to electron flavour neutrinos. The CC interaction in SNO is given by



This interaction has a threshold of 1.4MeV and is detected through the Cherenkov light produced by the outgoing electron. Other than being 1.4MeV lower, the energy spectrum of the outgoing electron is very similar to the neutrino. This makes the CC interaction very useful in measuring the energy spectrum of ^8B neutrinos. Figure 7.1 shows the electron energy spectra for neutrino energies of 5, 10, and 15MeV. The direction of the outgoing electron in the CC interaction is weakly correlated with the

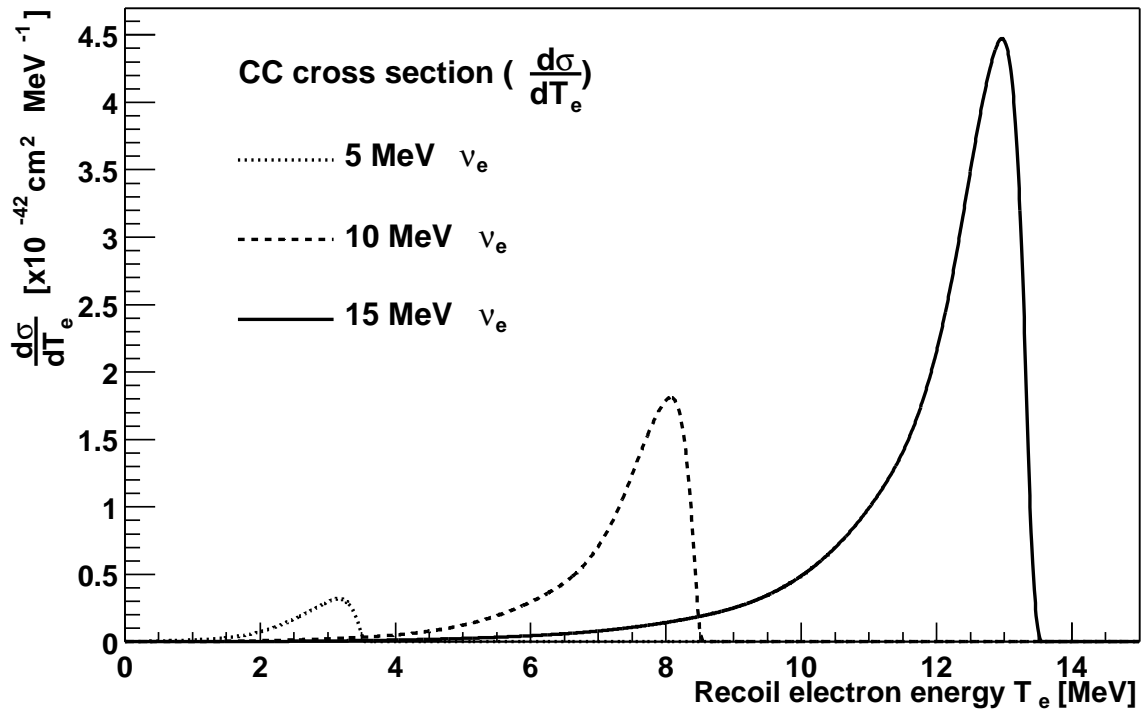


Figure 7.1: The CC differential cross section versus electron kinetic energy, T_e , for neutrino energies of 5, 10, and 15 MeV. The plot is taken from [30].

direction of the incoming neutrino. Although there is only a weak correlation, the CC electron directional distribution can be used to aid in the separation of the CC interaction from background and NC events.

For the salt phase of SNO the response of the SNO detector to the CC interaction is the same as that in the pure D₂O phase since the concentration of salt added is too small to effect the optics of the water. However, the addition of salt has made the distribution of Cherenkov light from the NC interaction much more isotropic than that of the CC interaction. This gives us additional information with which to separate the NC from the CC interaction. A large part of the uncertainty on the CC flux measurement in the pure D₂O phase was the correlation between the NC and CC events. Being able to separate between NC events and CC events using Cherenkov light isotropy is therefore a major advantage of the salt phase over the pure D₂O phase in terms of reducing the uncertainty on the extracted number of CC and NC events. The event isotropy comparison between the NC and CC interactions is discussed in chapter 8. The biggest advantage of being able to separate NC and CC events in terms of event isotropy is that the shape of the CC energy spectrum can be determined without relying on knowing the ⁸B neutrino energy spectrum. Extracting the neutrino energy spectrum allows for testing of the spectral distortions produced by the MSW neutrino oscillation theory. Figure 7.2 shows the energy spectrum of CC events as a function of outgoing electron energy with the SNO detector response included. The dashed blue curve is the CC spectrum for an undistorted ⁸B spectrum and the red curve is the oscillated ⁸B spectrum using the LMA solution to the MSW oscillations with mixing parameters of $\tan^2\theta = 0.4$ and $\Delta m^2 = 7.1 \times 10^{-5}$. The LMA solution predicts an upturn at lower energies. The analysis presented in chapters 8 and 9 extracts a CC energy spectrum down to an electron energy of 4MeV.

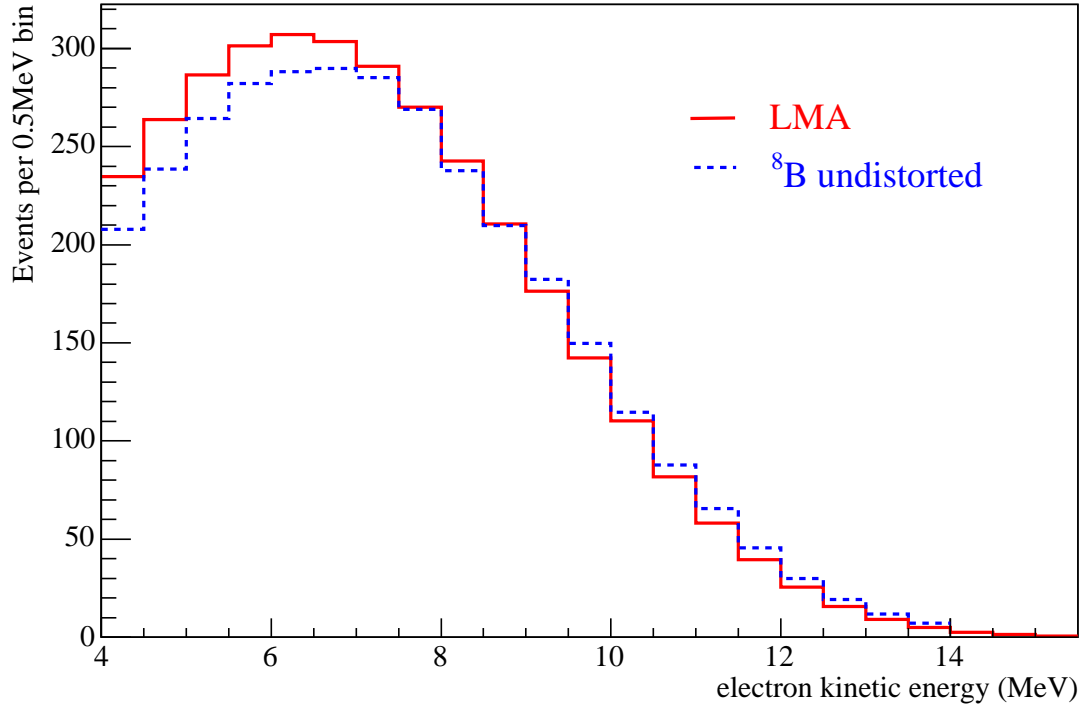


Figure 7.2: Energy spectrum of CC events in SNO for an undistorted ^8B spectrum (blue-dash) and the spectrum with MSW oscillations (red). The red curve is for the LMA solution to the MSW oscillation with mixing parameters of $\tan^2\theta = 0.4$ and $\Delta m^2 = 7.1 \times 10^{-5}$

7.3 The Elastic Scattering Interaction in the Salt Phase of SNO

The elastic scattering interaction is given by,

$$\nu_x + e \longrightarrow \nu_x + e$$

This interaction is sensitive mostly to electron flavour neutrinos with a weak sensitivity to other flavours of about 1/7 that of the electron flavour. The response of the SNO detector to this interaction is unchanged for the salt phase compared to the pure D₂O phase. SNO is not as sensitive to the ES interaction as it is to the other 2 neutrino signals. For example, in the pure D₂O phase there were 7 times more CC events extracted than ES events. Due to momentum conservation, the most probable direction of the scattered electron will be the same as the incoming neutrino. Therefore the $\cos \theta_{sun}$ distribution of ES events, which is the distribution of the cosine of the angle between the sun and the reconstructed event direction, will have a peak at angles corresponding to directly away from the sun. Since the other neutrino signals have $\cos \theta_{sun}$ distributions that have little or no correlation with the solar direction the ES events can be easily separated based upon the $\cos \theta_{sun}$ distribution.

7.4 Background Signals in the Salt Phase of SNO

To extract the neutrino signals down to a 4MeV energy threshold we need to include all known backgrounds in the SNO detector. As discussed in chapter ??, the radioactive backgrounds in SNO are ²¹⁴Bi, ²⁰⁸Tl, and ²⁴Na in the heavy water, ²¹⁴Bi and ²⁰⁸Tl in the light water, external (α, n) neutrons, and PMT $\beta - \gamma$ events. The internal

and external Cherenkov backgrounds were summarized by equation 6-1

$$\begin{aligned}
 B_{ext} &= AV_{Bi} + AV_{Tl} + H_2O_{Bi} + H_2O_{Tl} + PMT_{\beta-\gamma}, \\
 B_{int} &= D_2O_{Bi} + D_2O_{Tl} + D_2O_{Na}
 \end{aligned}$$

and the neutron backgrounds from photo-disintegration were summarized by equation 6-2

$$\begin{aligned}
 N_{ext} &= AV_{Bi,n} + AV_{Tl,n} + H_2O_{Bi,n} + H_2O_{Tl,n}, \\
 N_{int} &= D_2O_{Bi,n} + D_2O_{Tl,n} + D_2O_{Na,n}.
 \end{aligned}$$

For the 4MeV energy threshold analysis the number of background events from the various sources are extracted along with the neutrino signals.

7.5 Extracting the Neutrino Signals with the SNO Observables

Neutrino events cannot be separated in SNO on an event by event basis. However, after the low level and high level data cuts are applied and the events are reconstructed in position and energy a suitable energy threshold can be chosen such that the events with energy above the threshold are mostly neutrinos. Also, in both the pure D₂O phase and in the salt phase a single event cannot be identified to be a CC, elastic scattering (ES), neutral current (NC) event. However, given a distribution of events the number of events of each type can be extracted. Extracting the number of signal and background events from a distribution of events is known as a signal extraction. These distributions are generated using Monte-carlo calculations. The inputs to the Monte-carlo are the energy shape of the incident neutrinos, the neutrino-deuteron and

neutrino-electron cross sections, and the detailed description of the SNO detector and its response. The Monte-carlo returns the shapes of the three neutrino signals with the detector response factored in.

We considered five main observables to extract the different components of the SNO neutrino data: energy, isotropy, radial position, $\cos\theta_{sun}$, and $\vec{U} \cdot \vec{R}$. Energy is the calibrated energy of the event derived from the number of PMTs hit and the position and direction of the event. For the signal extraction we use the kinetic energy which we designate as T_{eff} . Radial position is just the radial position from the centre of the detector. For radius we use a term designated as ρ that represents the fraction of the D₂O volume,

$$\rho = \frac{R^3}{600^3}$$

Isotropy is a measure of the mean pair angle between the detected photons in a given event. The isotropy parameter used is called β_{14} and is defined as $\beta_1 + 4\beta_4$. Where,

$$\beta_1 = \frac{2}{N(N-1)} \sum_{i=1}^{N-1} \sum_{j=i+1}^N \cos\theta_{ij}, \quad (7-1)$$

and

$$\beta_4 = \frac{2}{N(N-1)} \sum_{i=1}^{N-1} \sum_{j=i+1}^N \cos^4\theta_{ij}. \quad (7-2)$$

These are just the first and fourth order Legendre polynomial of the mean pair angle between detected photons, as estimated by the angle between the centres of the PMTs, θ_{ij} . N is the total number of PMTs hits for an event and i and j are indices representing any two PMTs. The combination $\beta_1 + 4\beta_4$ was chosen since the distribution is very similar to a Gaussian and thus can be easily perturbed to determine the systematic uncertainties. An event with a single Cherenkov ring is less isotropic than a multi-ring

event. The $\cos\theta_{sun}$ value is the cosine of the angle between the event direction and the vector from the sun. The vector \vec{U} is the direction vector defined by

$$\vec{U} = (u, v, w) \quad (7-3)$$

and the vector \vec{R} is defined as

$$\vec{R} = (x, y, z). \quad (7-4)$$

Therefore the product $\vec{U} \cdot \vec{R}$ is a measure of how inward or out-ward going an event is. A $\vec{U} \cdot \vec{R}$ value less than zero means the event is reconstructed to be going inward and a value greater than zero implies an outward going event. The product $\vec{U} \cdot \vec{R}$ is normalized such that a value of 1 implies the event is going directly outward from centre and a value of -1 means the event is going directly inward from centre.

7.5.1 Neutrino Signal Distributions

Figure 7.3 shows the comparison between the three neutrino signals in kinetic energy, isotropy, $\cos\theta_{sun}$, and radial position. From figure 7.3 it is evident that the NC and CC neutrino events are significantly different from each other in their β_{14} distributions that they can be separated from each other on a statistical basis without relying on the energy distributions. For the separation of ES neutrino events we rely on the $\cos\theta_{sun}$ distributions. In the ES reaction the scattered electron direction is very strongly peaked in the direction away from the incoming neutrino. This means that the electron direction is peaked directly away from the sun. For the NC reaction the direction of the γ -rays produced in the de-excitation of ^{36}Cl are not correlated to the direction of the initial neutrino that produced the neutron. Therefore in NC reaction the direction of the incident neutrino is lost. The CC reaction is weakly sensitive to the the direction of the incoming neutrino direction and is slightly backward peaked

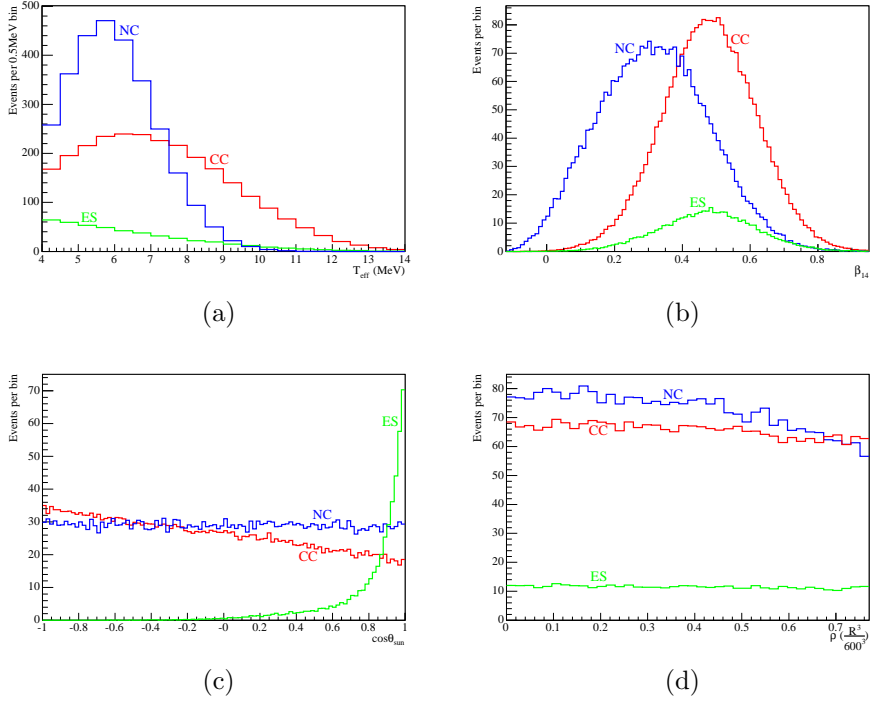


Figure 7.3: Energy, β_{14} , $\cos\theta_{sun}$, and radial distributions for the CC, ES, and NC neutrino signals.

compared to the ES reaction. The $\cos\theta_{sun}$ distribution is therefore a very strong handle on the extracting the number of ES events. In fact, the ES neutrino events are the most easily extracted of the neutron signals. The radial distributions of the neutrino signals are all very similar. The radial distributions play an important role when the external radioactive backgrounds are included in this analysis.

7.5.2 The Background Distributions

The backgrounds distributions are shown in figures 7.4 and 7.5 for the internal and external backgrounds respectively. From figure 7.4 it is clear that the energy

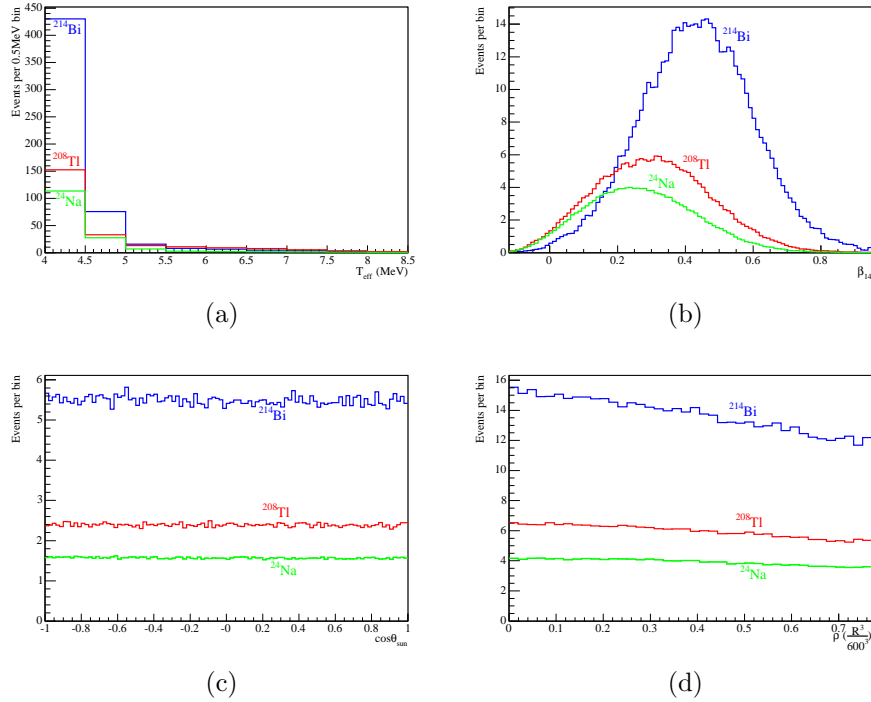


Figure 7.4: Energy, β_{14} , $\cos\theta_{sun}$, and radial distributions for the internal heavy water radioactive background signals in SNO.

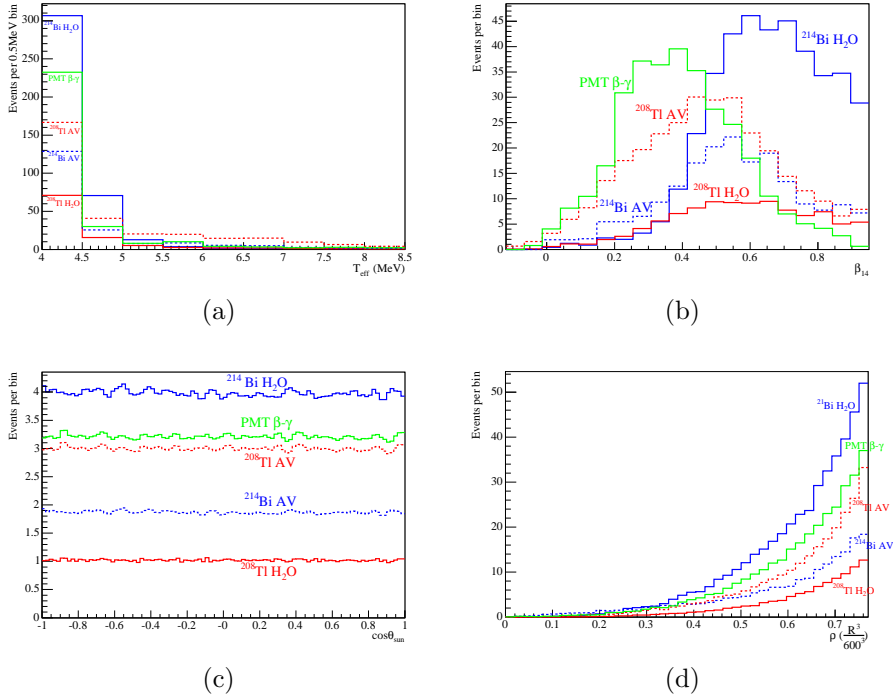


Figure 7.5: Energy, β_{14} , $\cos\theta_{\text{sun}}$, and radial distributions for the external light water, AV, and PMT radioactive background signals in SNO.

distributions of the backgrounds are very much different than the neutrino signals. All the known backgrounds in SNO peak at much lower energies than the neutrino signals. Panel (b) of figure 7.4 shows that the β_{14} distribution gives good separability between the ^{208}Tl and ^{214}Bi backgrounds in the heavy water. This is because the ^{208}Tl β -decay has a delayed γ -ray that comes with the decay. Therefore in the SNO detector the ^{208}Tl events have two Cherenkov rings associated with them and are more isotropic on average than ^{214}Bi events. As expected, the $\cos\theta_{sun}$ and radial distributions do not give any separation between the internal backgrounds. For the external backgrounds however, the radial distributions are obviously much different than the internal backgrounds. To separate between the different external backgrounds we use the β_{14} and $\vec{U}\cdot\vec{R}$ distributions. Figure 7.6 shows the $\vec{U}\cdot\vec{R}$ distributions for the external backgrounds. As a comparison the $\vec{U}\cdot\vec{R}$ distribution of the internal ^{214}Bi background in the heavy water is also shown in figure 7.6. There is obviously a significant difference in the $\vec{U}\cdot\vec{R}$ distribution between the internal and external backgrounds.

The long tail on the high side of the β_{14} distributions for the external backgrounds is due to external background events that Compton scatter in the light water but misreconstruct in the heavy water. These events have a very tight Cherenkov ring that is expected of outward going events that occur near the PMTs in the light water. However, since these events misreconstruct in the heavy water, the light from these events looks like a narrow beam pointing outward towards the PMTs and not like Cherenkov light with the expected Cherenkov angle. The end result are events that are much less isotropic than normal Cherenkov light and therefore show up on the high side of the β_{14} distribution. This effect was described in section 6.3.

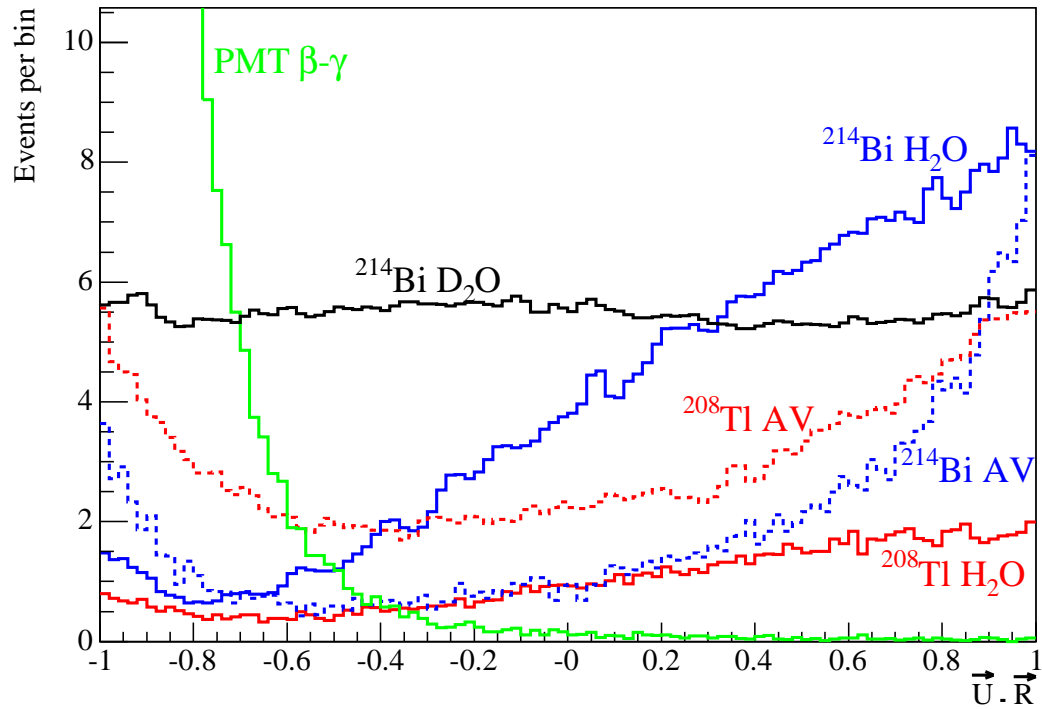


Figure 7.6: The $\vec{U} \cdot \vec{R}$ distributions for the external backgrounds. Also shown for comparison is the $\vec{U} \cdot \vec{R}$ distribution for the internal heavy water ^{214}Bi background.

Chapter 8

Extracting the Neutrino Signals

The previous analysis of the salt phase data was done for an energy threshold of 5.5MeV kinetic energy and a fiducial volume within 550cm [13]. The reason for this choice of analysis window was to minimize the internal and external Cherenkov background in the signal window. As mentioned previously, the dominant backgrounds are ^{214}Bi and ^{208}Tl in the D_2O and H_2O regions. Since these backgrounds have energies that peak at much lower energies than the neutrino signals, most of the background can be eliminated by choosing a sufficiently high energy threshold. However, the interesting physics in terms of deviation from the standard large mixing angle (LMA) solution can only be observed at energies lower than 5.5MeV. The possible processes that may cause deviation from the LMA solution were discussed in chapter 2, and will also be discussed in chapter 10. To decrease the energy threshold it is necessary to decrease the amount of background. This is done by employing an energy dependent fiducial volume. For lower energies, the radial cut is moved in from 550cm so that the external background can be decreased. At higher energies there are fewer background events and the radial cut can be relaxed. Figure 8.1 shows the number of events as

a function of energy and radius for the salt phase data with only the low level data cleaning cuts applied. The external H₂O background contribution is clearly visible a high radius and low energy. It is clear then that the external background can be removed by choosing events that reconstruct further from the AV.

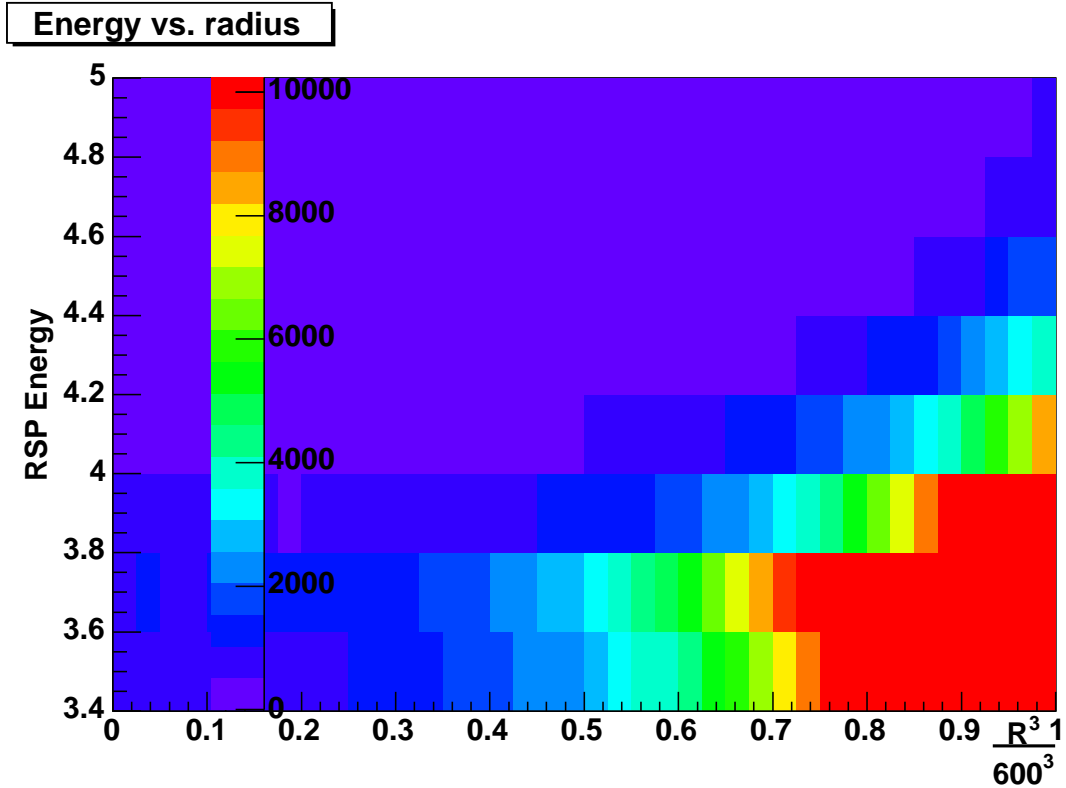


Figure 8.1: The number of events as of function of energy, and fraction of the heavy water volume, $\frac{R^3}{600^3}$. Colour corresponds to the number of events per bin.

For the lowest energy bins the uncertainty on the extracted CC signal is dominated by the uncertainty on the number of Cherenkov background events. To get the best possible measurement of the CC spectrum we therefore want to minimize the Cherenkov background uncertainty to charge current signal for every energy bin. This is the deciding factor in choosing an appropriate fiducial volume for a given energy

threshold. Figure 8.2 shows the Cherenkov background uncertainty to CC signal ratio for various energy bins and fiducial volumes. A fiducial volume of 476cm seems to give the optimum background uncertainty to CC signal ratio. Any fiducial volume less than that and the reduction in background is less than the loss of statistical precision.

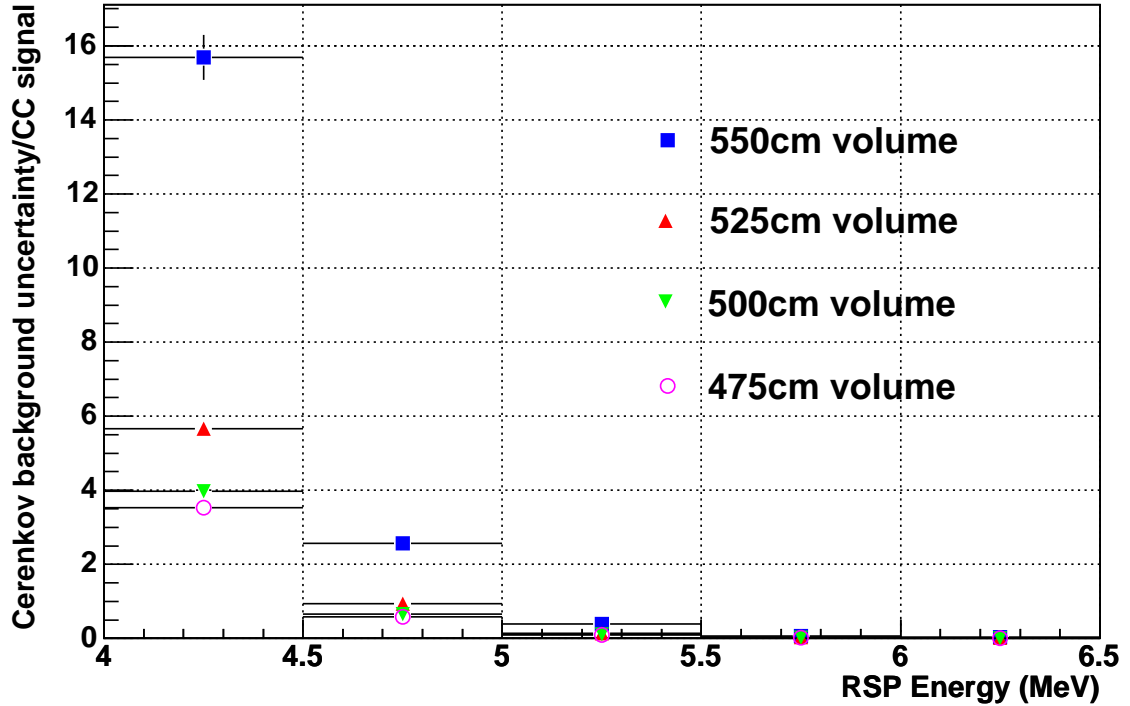


Figure 8.2: Ratio of Cherenkov background uncertainty to CC signal.

8.1 Signal Extraction in the Salt Phase of SNO

To extract and separate the number of events for the CC, ES, and NC neutrino interactions Probability Distribution Functions (PDFs) are defined based on the observables

outlined in section 7.5. For the analysis in this thesis the PDFs are parameterized as follows,

$$P(T_{eff}, \beta_{14}, \rho, \cos \theta_{sun}, \vec{U} \cdot \vec{R}) = P(T_{eff}, \beta_{14}) \times P(\rho) \times P(\cos \theta_{sun}) \times P(\vec{U} \cdot \vec{R}) \quad (8-1)$$

where T_{eff} , β_{14} , $\cos \theta_{sun}$, ρ , and $\vec{U} \cdot \vec{R}$ are the observables described in section 7.5. Since there is a strong correlation between energy and isotropy we use a two dimensional PDF for T_{eff} and β_{14} . Figure 8.3 shows the two dimensional distributions for β_{14} as a function of T_{eff} for the 3 neutrino signals.

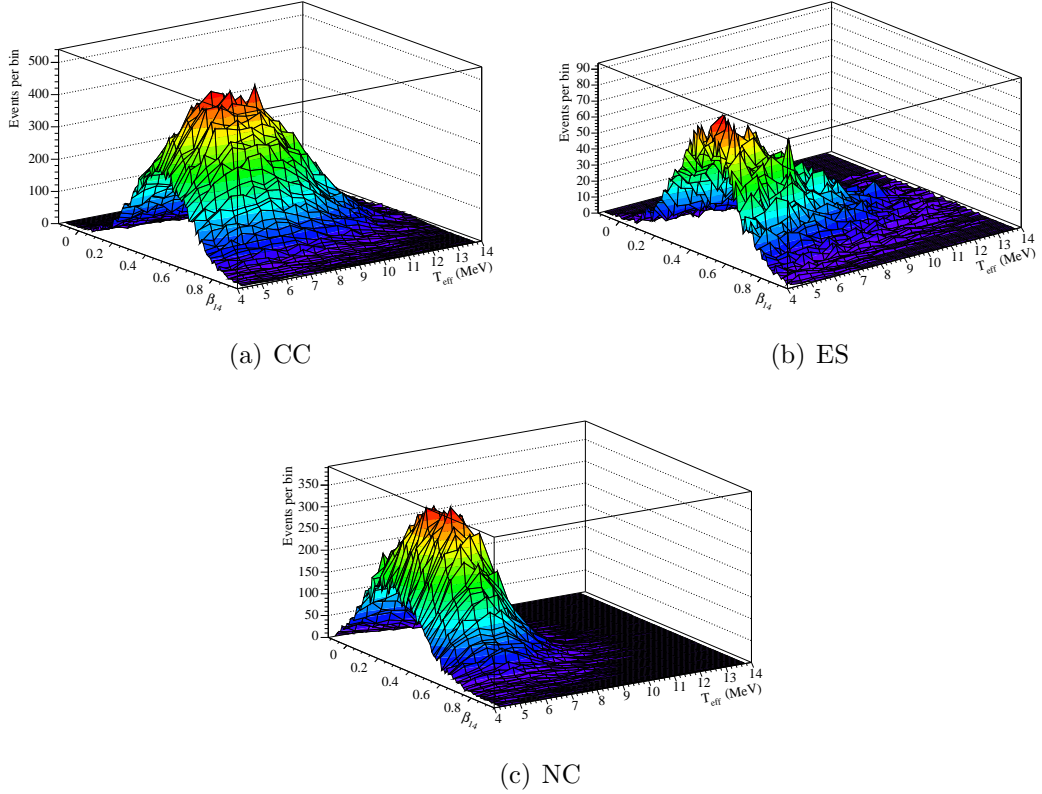


Figure 8.3: 2-Dimensional energy versus β_{14} PDFs for the 3 neutrino signals.

In doing a signal extraction the neutrino signals are separated using the PDFs,

$$\mathcal{F}_{signal} = \alpha_{CC}F_{CC} + \alpha_{ES}F_{ES} + \alpha_{NC}F_{NC} + \alpha_{BKG}F_{BKG}. \quad (8-2)$$

where F_{CC} , F_{ES} and F_{NC} are the 3 neutrino signals as functions of the radial, $\cos \theta_{sun}$, energy/ β_{14} , and $\vec{U} \cdot \vec{R}$ PDFs. F_{BKG} represents the background signals as a function of the same PDFs. The values α_{CC} , α_{NC} , α_{ES} , and α_{BKG} are the number of events corresponding to each signal and is what we want to extract. The background events can also be separated in the same signal extraction,

$$\begin{aligned} \mathcal{F}_{BKG} &= \alpha_{BID2O}F_{BID2O} + \alpha_{TLD2O}F_{TLD2O} \\ &+ \alpha_{BIH2O}F_{BIH2O} + \alpha_{TLH2O}F_{TLH2O} \\ &+ \alpha_{BIAV}F_{BIAV} + \alpha_{TLAV}F_{TLAV} \\ &+ \alpha_{PMT}F_{PMT} + \alpha_{NA24}F_{NA24} + \alpha_{NCBE}F_{NCBE}. \end{aligned}$$

where F_{BID2O} , F_{BIH2O} , F_{BIAV} , F_{TLD2O} , F_{TLH2O} , and F_{TLAV} represent the ^{214}Bi and ^{208}Tl backgrounds in the D_2O , H_2O , and on the acrylic vessel respectively. F_{NA24} is ^{24}Na background in the D_2O , F_{PMT} is the PMT $\beta-\gamma$ background, and finally F_{NCBE} is the external neutron background originating at the acrylic vessel specifically from the (α, n) reaction. The photo-disintegration neutron events caused by γ -rays from various backgrounds are included in the corresponding background PDFs.

Neutrino signals may be extracted with the CC and ES energy shape constrained or unconstrained. In the constrained analysis the PDFs are parameterized as defined by equation 8-1 and the energy PDFs used are the two dimensional PDFs shown in figure 8.3. In the un-constrained fit the ES and CC PDF parameterization is given as

$$P(\beta_{14}^i, \rho, \cos \theta_{sun}, \vec{U} \cdot \vec{R}) = P(\beta_{14}^i) \times P(\rho) \times P(\cos \theta_{sun}) \times P(\vec{U} \cdot \vec{R}) \quad (8-3)$$

where the index i represents i^{th} energy bin in the two dimensional CC and ES distributions of figure 8.3. Therefore each PDF β_{14}^i is the β_{14} distribution at a given energy bin. For the signal extraction done here the energy bins are 0.5MeV wide and the extraction is done between 4 and 14MeV.

As done in [30] and in most signal extractions done on the SNO data we extract the neutrino signals using a maximum likelihood technique. A likelihood function can be defined as

$$\mathcal{L} = \prod_{i=1}^N \mathcal{F}_{signal,i} \quad (8-4)$$

where i represents the i 'th events in the data set and \mathcal{F}_{signal} is just the sum of the signal PDFs as defined by equation 8-2. We define the log-likelihood as

$$\mathcal{L}_{log} = -2 \sum_{i=0}^N \log(\mathcal{F}_{signal,i}). \quad (8-5)$$

Substituting equation 8-3 into equation 8-5 we get

$$\mathcal{L}_{log} = -2 \sum_{i=1}^N \log(\alpha_{CC}F_{CC} + \alpha_{ES}F_{ES} + \alpha_{NC}F_{NC} + \alpha_{BKG}F_{BKG}) \quad (8-6)$$

where the $\alpha_{BKG}F_{BKG}$ term represents the background contribution of equation 8-3. We vary the parameters α_{CC} , α_{ES} , α_{NC} , α_{BID2O} , α_{TLD2O} , α_{BIH2O} , α_{TLH2O} , α_{BLAV} , α_{TLAV} , α_{PMT} , α_{NA24} , and α_{NCBE} in order to minimize equation 8-6. Ultimately our goal is to convert the number of extracted neutrino events into a neutrino flux. Therefore we need to include the probability of getting data set of N events given a mean flux, Φ [31]. A Poisson distribution is therefore included in the likelihood function to give an extended likelihood function,

$$\mathcal{L}_E = \frac{\exp^{-\Phi} \Phi^N}{N!} \mathcal{L} \quad (8-7)$$

Now we can get the total number of signal events from the fitted α parameters,

$$\begin{aligned}
\Phi_{CC} &= \Phi_{\alpha_{CC}} \\
\Phi_{ES} &= \Phi_{\alpha_{ES}} \\
\Phi_{NC} &= \Phi_{\alpha_{NC}} \\
\Phi_{BID2O} &= \Phi_{\alpha_{BID2O}} \\
\Phi_{BIH2O} &= \Phi_{\alpha_{BIH2O}} \\
\Phi_{TLD2O} &= \Phi_{\alpha_{TLD2O}} \\
\Phi_{TLH2O} &= \Phi_{\alpha_{TLH2O}} \\
\Phi_{BIAV} &= \Phi_{\alpha_{BIAV}} \\
\Phi_{TLAV} &= \Phi_{\alpha_{TLAV}} \\
\Phi_{PMT} &= \Phi_{\alpha_{PMT}} \\
\Phi_{NA24} &= \Phi_{\alpha_{NA24}} \\
\Phi_{NCBE} &= \Phi_{\alpha_{NCBE}}
\end{aligned}$$

Putting equation 8-4 into the extended likelihood function, equation 8-7, we now get

$$\mathcal{L}_E = \frac{\exp^{-(\Phi_{signal} + \Phi_{bkg})}}{N!} \prod_{i=1}^N (\Phi_{signal} F_{signal} + \Phi_{bkg} F_{bkg}) \quad (8-8)$$

where

$$\Phi_{signal} = \Phi_{CC} + \Phi_{ES} + \Phi_{NC}$$

and

$$\Phi_{bkg} = \Phi_{BID2O} + \Phi_{TLD2O} + \Phi_{BIH2O} + \Phi_{TLH2O} + \Phi_{BIAV} + \Phi_{TLAV} + \Phi_{PMT} + \Phi_{NA24} + \Phi_{NCBE}$$

similarly

$$\Phi_{signal}F_{signal} = \Phi_{CC}F_{CC} + \Phi_{ES}F_{ES} + \Phi_{NC}F_{NC}$$

and

$$\begin{aligned}\Phi_{bkg}F_{bkg} &= \Phi_{BID2O}F_{BID2O} + \Phi_{TLD2O}F_{TLD2O} \\ &+ \Phi_{BIH2O}F_{BIH2O} + \Phi_{TLH2O}F_{TLH2O} \\ &+ \Phi_{BIAV}F_{BIAV} + \Phi_{TLAV}F_{TLAV} \\ &+ \Phi_{PMT}F_{PMT} + \Phi_{NA24}F_{NA24} + \Phi_{NCBE}F_{NCBE}\end{aligned}$$

Taking the negative log of equation 8-8 we have

$$\mathcal{L}_E = 2 \left[\Phi_{signal} + \Phi_{bkg} + \log(N!) - \sum_{i=1}^N \log(\Phi_{signal}F_{signal} + \Phi_{bkg}F_{bkg}) \right] \quad (8-9)$$

By minimizing equation 8-9 we determine the number of signal and background events in the data set. Unlike equation 8-6, the uncertainties on the best fit values for equation 8-9 will include uncertainties due to Poisson fluctuations in the number of events in our data set. Therefore the uncertainties on the number of signal events can be used on the corresponding neutrino fluxes.

To reduce the uncertainties on the extracted neutrino signals, the background event numbers are constrained by measurements external to the neutrino signal window. These measurements were described in chapter 6. The external background constraints are added to the logarithm of the likelihood function when doing the fit. If we wish to add an external constraint on the number of fitted background events x for example, then the addition to the likelihood function would be,

$$x_a = \frac{1}{\sqrt{2\pi}\sigma_{x_m}} \exp^{0.5\left(\frac{x-x_m}{\sigma_{x_m}}\right)^2}, \quad (8-10)$$

$$F = F - 2\log(x_a) \quad (8-11)$$

where x_m is the measured number of background events from the external constraint, σ_{x_m} is the uncertainty on the background measurement, and F is the logarithm of the likelihood function.

Chapter 9

Systematic Uncertainties in the Flux Extraction

To extract the neutrino signals in the salt phase of SNO we rely on Monte-carlo calculations to generate the PDFs. Since the Monte-carlo plays such an important role in the analysis, it is crucial that it is verified. The verification of the Monte-carlo is done through comparison with the calibration sources. While no calibration source exists that exactly reproduces any of the neutrino signals, Monte-carlo simulations are done for the calibration sources and then compared with the sources themselves. If the calibration source Monte-carlo is able to reproduce the calibration data then there is confidence that the Monte-carlo technique reproduces the neutrino signals. Disagreement between the shapes of the distributions derived from the calibration data and from the Monte-carlo are incorporated as systematic uncertainties on the extracted neutrino signals. The ^{16}N β - γ source is the main source used to verify the Monte-carlo in energy, radius, β_{14} , $\cos\theta_{sun}$, and $\vec{U} \cdot \vec{R}$. Other sources, such as the ^{252}Cf neutron source, are used as secondary tests. To test the extraction of the

neutrino signals it is also useful to generate fake Monte-carlo data sets to test the signal extraction and make sure there are no biases in the extraction.

9.1 Energy Systematic Uncertainties

The largest component of the systematic uncertainties on the extracted neutrino signals is due to the uncertainty on the energy scale and resolution. Most of the systematic uncertainty due to the energy response is estimated by comparing the ^{16}N calibration source data with ^{16}N source Monte-carlo. The largest components of the energy response uncertainty will be described in detail in this section and all the uncertainties that were used to derive the full energy response uncertainty will be summarized in a table at the end of this section.

9.1.1 Energy Stability Uncertainty

The energy response of the SNO detector is not stable over the salt phase running period. This energy response drift is believed to be caused by an increase in the attenuation coefficients in the D_2O volume which in turn decreases the light output of events. The increase in the D_2O attenuation is thought to be caused by manganese deposited in the D_2O after MnO_x assays. The MnO_x assays were described in section 6.2. Indeed, after the MnO_x assays were stopped at the end of the salt phase running period there was no more drift observed in the energy response for the remainder of the salt phase. The optical constants were determined through the Laserball calibration. It was found that the constants changed over time. These constants were then fed into the Monte-carlo which then showed a drift in the energy response. The drift in the energy response was studied by comparing the energy response to ^{16}N calibration

source runs at the centre of the detector as a function of date. Figure 9.1 shows the comparison of the means of the $N_{corrected}$ distributions between the ^{16}N Monte-carlo and data. $N_{corrected}$ is the number of prompt PMT hits for a given event corrected for the number of PMTs that are working compared to the total number of PMTs, the noise rate, and the optical response relative to the optical response at the centre. $N_{corrected}$ is thus given by

$$N_{corrected} = \frac{N_{prompt} - N_{noise}}{\epsilon_{response}/\epsilon_0} \frac{PMT_{total}}{PMT_{working}} \quad (9-1)$$

where N_{prompt} is the number of prompt hits, N_{noise} is the noise hits, $\epsilon_{response}$ is the optical response, ϵ_0 is the optical response at the centre, PMT_{total} is the total number of PMTs, and $PMT_{working}$ is the number of working PMTs.

After the energy response is corrected for the varying attenuation coefficients the Monte-carlo energy response is compared to the data for the ^{16}N source and the difference is added as a systematic uncertainty to the energy scale and resolution uncertainties. Figure 9.2 shows a comparison between the mean energy obtained from the ^{16}N Monte-carlo and the ^{16}N data for calibration runs at the centre for the entire salt data set. The mean and width of the ^{16}N data energy was divided by the mean and width of the Monte-carlo energy. The weighted mean of the data to Monte-carlo ratios of the energy width and mean are given by

$$R_{mean} = \frac{1}{w_\mu} \sum_{i=1}^N \frac{1}{\sigma_{\mu,i}^2} \frac{\mu_{d,i}}{\mu_{mc,i}} \quad (9-2.a)$$

$$R_{width} = \frac{1}{w_\sigma} \sum_{i=1}^N \frac{1}{\sigma_{\sigma,i}^2} \frac{\sigma_{d,i}}{\sigma_{mc,i}} \quad (9-2.b)$$

where

$\mu_{d,i}$ mean energy for data run i,

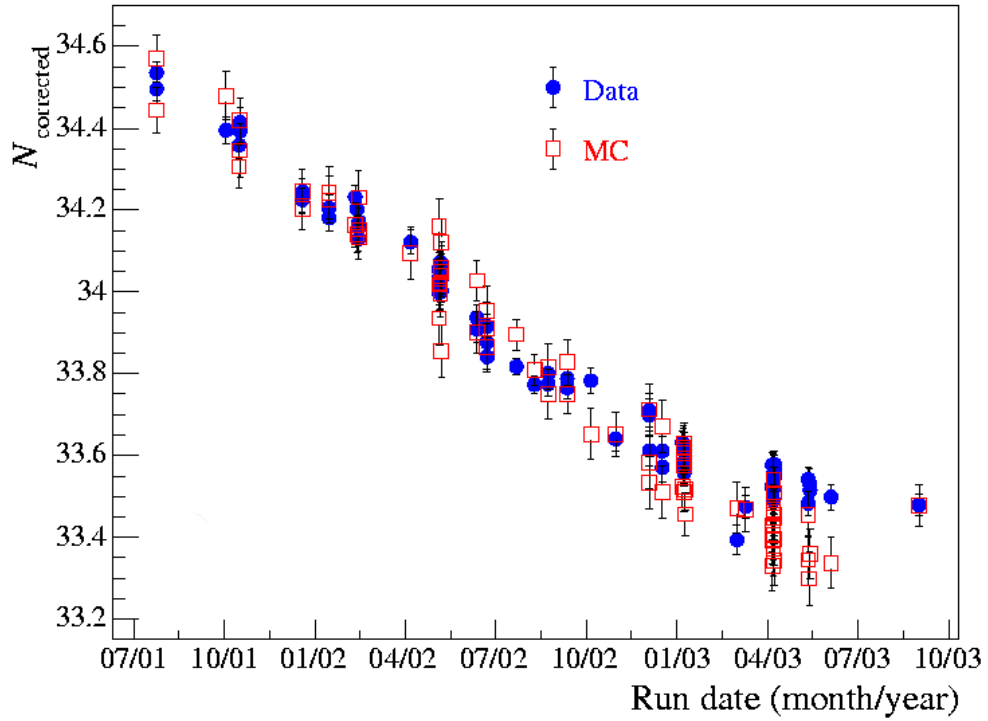


Figure 9.1: Mean of the $N_{corrected}$ distributions for Monte-carlo and ^{16}N data as a function of date. We can see that the trend of the Monte-carlo points are in good agreement with data. Figure is taken from [1]

$\mu_{mc,i}$ mean energy for Monte-carlo run i,
 $\sigma_{\mu,i}$ is the uncertainty on the ratio of the data energy to the Monte-carlo energy,
 $w_{\mu} = \sum_{i=1}^N \frac{1}{\sigma_{\mu,i}^2}$,
 $\sigma_{d,i}$ width of the energy distribution for data run i,
 $\sigma_{mc,i}$ width of the energy distribution for Monte-carlo run i,
 $\sigma_{\sigma,i}$ is the uncertainty on the ratio of the data energy width to the Monte-carlo energy width, and
 $w_{\sigma} = \sum_{i=1}^N \frac{1}{\sigma_{\sigma,i}^2}$.

The fractional uncertainty on the the energy mean and width is then given by

$$\sigma_{mean} = |1 - R_{mean}| \quad (9-3.a)$$

$$\sigma_{width} = |1 - R_{width}| \quad (9-3.b)$$

Table 9.1 shows the ratios of data to Monte-carlo for the mean and width of the ^{16}N source energy distribution. The ratios of the mean and widths are split into two time periods since during the end of the salt phase the attenuation coefficients did not change anymore. Most of the salt phase data is in the period where the attenuation coefficients are changing, about 88% of the data, while the during the remainder of the data the attenuation coefficients were constant. The energy scale and energy resolution uncertainty from the drift in the energy response are therefore

$$Energyscale = 0.879 \times 0.11 + 0.121 \times 0.4 = 0.15\%$$

$$Energyresolution = 0.879 \times 1.7 + 0.121 \times 2.6 = 1.8\%$$

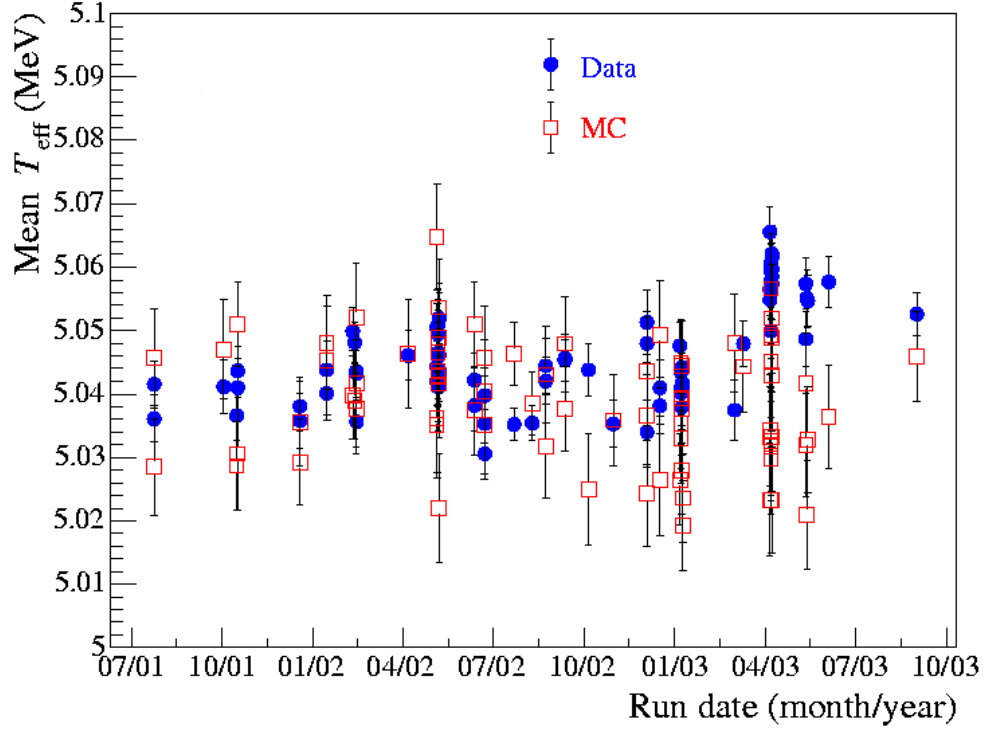


Figure 9.2: Mean energy of ^{16}N source calibration runs and ^{16}N source source Monte-carlo as a function of date for the entire salt data set. The ^{16}N runs are at the centre of the detector. Figure is taken from [1]

	Mean	Weighted Mean
Ratio of means (before 04/03)	1.0014 ± 0.00026	1.0012 ± 0.00018
Ratio of means (after 04/03)	1.0041 ± 0.00075	1.0039 ± 0.00065
Ratio of widths (before 04/03)	1.018 ± 0.0012	1.017 ± 0.0011
Ratio of widths (after 04/03)	1.026 ± 0.0048	1.026 ± 0.0042

Table 9.1: Ratio of data to Monte-carlo energies for ^{16}N source runs at centre. The ratios are for the mean and widths of the energy distributions.

9.1.2 Energy Uncertainty from Position Asymmetry

The energy response of the detector is not uniform throughout the D₂O volume. This is especially true at positions near the acrylic vessel (AV) and also at the top of the detector near the neck since there are no PMTs in the neck area. Near the AV the energy response changes due to reflections off the AV and the fact that the PMT efficiency is dependent on incident angle. While the Monte-carlo reproduces some of the energy response as a function of position, the difference between the Monte-carlo energy response and the ¹⁶N data energy response is included into the total energy uncertainty. Due to limitations on the ability to deploy calibration sources, there are many more ¹⁶N runs in the bottom half of the detector than at the top near the AV. Since the neutrino data are uniformly distributed in the detector, the energy response derived from the ¹⁶N calibration does not reflect the energy response to neutrino data. Therefore the asymmetry in the deployment of the ¹⁶N calibration source has to be included in the systematic uncertainty of the energy response. This is done through a volume weighted comparison between data and Monte-carlo for ¹⁶N runs at various positions. This uncertainty is determined in a similar way as the time dependence uncertainty outlined by equations 9-2 and 9-3. For the position asymmetry the data to Monte-carlo ratios are also weighted by the volume region of the given run,

$$R_{mean}^p = \frac{1}{w_\mu^p} \sum_{i=1}^N \frac{1}{(\sigma_{\mu,i} r_i^3)^2} \frac{\mu_{d,i}}{\mu_{mc,i}} \quad (9-4.a)$$

$$R_{width}^p = \frac{1}{w_\sigma^p} \sum_{i=1}^N \frac{1}{(\sigma_{\sigma,i} r_i^3)^2} \frac{\sigma_{d,i}}{\sigma_{mc,i}} \quad (9-4.b)$$

$$w_\mu^p = \sum_{i=1}^N \frac{1}{(\sigma_{\mu,i} r_i^3)^2} \quad (9-4.c)$$

$$w_\sigma^p = \sum_{i=1}^N \frac{1}{(\sigma_{\sigma,i} r_i^3)^2} \quad (9-4.d)$$

where r_i is the radial position of event i . As in equation 9-3 the deviation of $R_{v_{mean}}^p$ and $R_{v_{width}}^p$ from unity is taken as the uncertainty. Figure 9.3 shows the ^{16}N mean energy as a function of source radius for both data and Monte-carlo. The volume weighted differences between data and Monte-carlo are taken as an uncertainty.

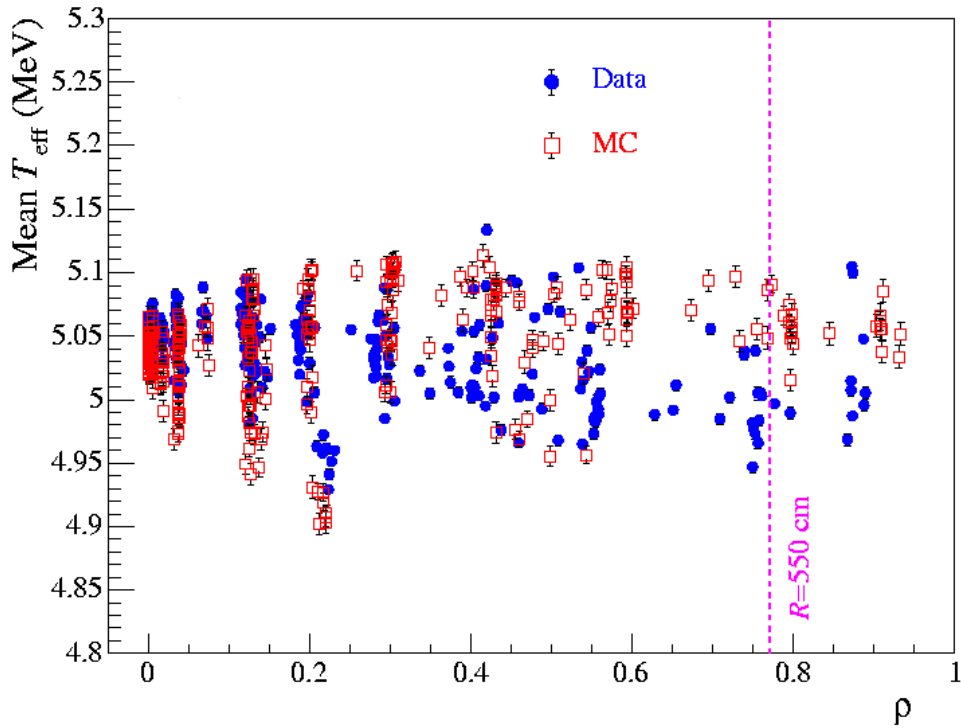


Figure 9.3: Mean energy of ^{16}N source calibration runs and ^{16}N source source Monte-carlo as a function of source position. The dashed line represents the previous radial acceptance region of 550cm. Figure is taken from [1].

Figure 9.4 shows the run-by-run ratio of mean data energy to mean Monte-carlo energy as a function of radial source position. It is obvious that for runs at higher radius the Monte-carlo over estimates the energy response by over 1%. The uncertainty on the energy scale arising from the volume weighted difference between data

and Monte-carlo is 0.45%. The corresponding uncertainty on the energy resolution is 1.4%.

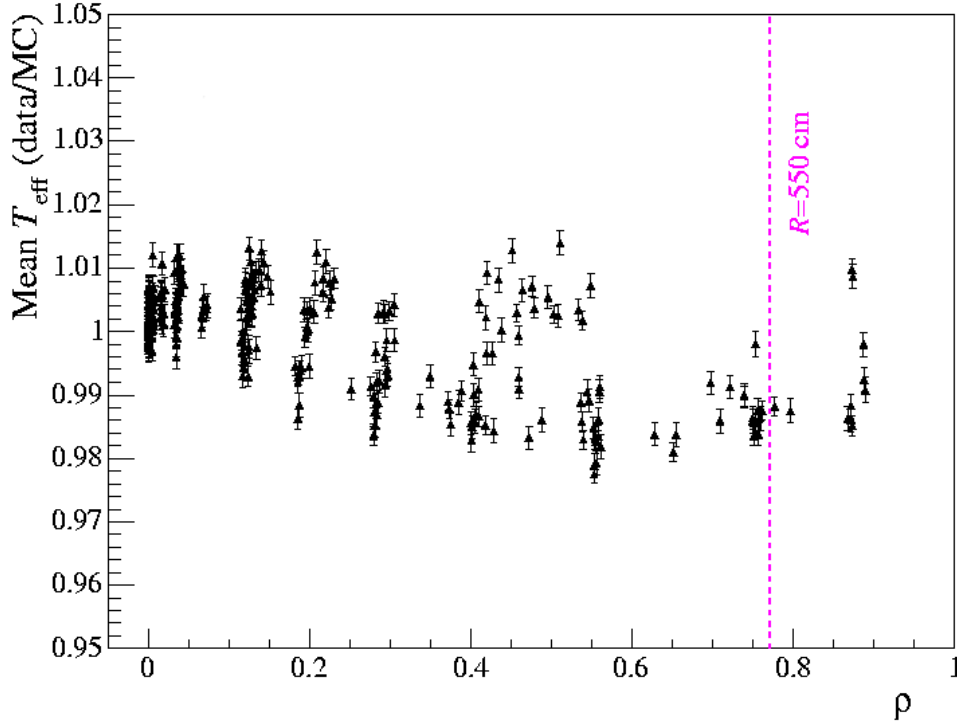


Figure 9.4: Ratio of mean ^{16}N data energy to Monte-carlo energy on a run-by-run basis as a function of radial source position. ρ represents the normalized radius ($R^3/600^3$). Figure is taken from [1].

As mentioned previously, the set of ^{16}N calibration runs sample the lower half ($z < 0$) of the detector a lot more than the top half. Figure 9.5 shows the x and z coordinates of the ^{16}N source positions. It is clear that there are not only a lot more ^{16}N runs at the bottom half of the detector but the runs in the top half do not extend all the way to 600cm. The volume weighted comparison between data and Monte-carlo as outlined by equation 9-4 does not take into account x, y, and z asymmetries

in the ^{16}N source deployment. To assign an uncertainty from the asymmetry in ^{16}N positions the reconstructed ^{16}N was divided into seven radial bins. For each of the radial bins the mean and width of the energy distribution for each run is collected in a histogram. The size of the standard deviation of the histogram for the mean energies is assumed to be measure of the change in the mean energy due to source position. Similarly, the standard deviation of the histogram of the energy widths is assumed to be a measure of the dependence of the energy resolution on source position. The volume weighted average of the seven radial bins in mean energy and energy width are taken as the uncertainty. Tables 9.2 and 9.3 show the standard deviation for each of the radial bins of the energy mean and energy width respectively. Included are also the volume weighted energy mean and energy width. These are taken as the contribution from the position asymmetry to the total energy uncertainty.

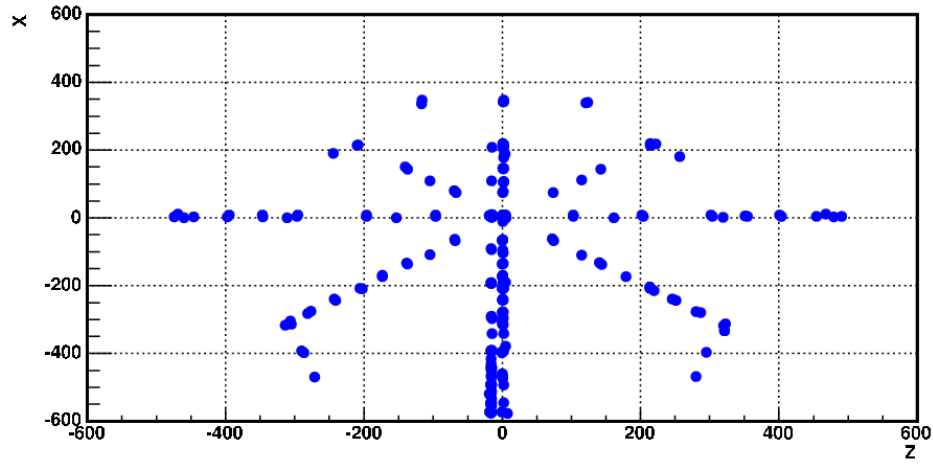


Figure 9.5: The X and Y coordinates of ^{16}N source deployment positions.

Region ($R^3/600^3$)	σ
0-0.1	0.0031
0.1-0.15	0.0052
0.15-0.25	0.0064
0.25-0.35	0.0057
0.35-0.5	0.0082
0.5-0.6	0.0093
0.6-0.77	0.0037
Volume weighted	0.0059

Table 9.2: Standard deviations of the reconstructed data to Monte-carlo ratio of the ^{16}N mean energy for various radial bins. The volume weighted standard deviation is taken as the uncertainty on the energy scale due to detector asymmetry. We therefore take this uncertainty to be 0.59%.

Region ($R^3/600^3$)	σ
0-0.1	0.011
0.1-0.15	0.011
0.15-0.25	0.013
0.25-0.35	0.012
0.35-0.5	0.018
0.5-0.6	0.015
0.6-0.77	0.012
Volume weighted	0.014

Table 9.3: Standard deviations of the reconstructed data to Monte-carlo ratio of the ^{16}N energy width for various radial bins. The volume weighted standard deviation, 1.4%, is the uncertainty on the energy scale due to detector asymmetry.

9.1.3 ^{16}N Source Modeling

The uncertainty that arises from modeling the ^{16}N source is one of the larger uncertainties that go into the total energy scale uncertainty. The dominant source uncertainties arise from uncertainties on the branching ratios in the ^{16}N decay, uncertainty in the source geometry used in the Monte-carlo simulation, and the velocity dependence in the Cherenkov wavelength spectrum. The velocity dependence deals with the change in the emitted Cherenkov wavelength as a function of electron velocity. There is also a contribution from the uncertainty on the parameters and cross sections that are used in the EGS4 (Electron-gamma shower particle transport code) code that is used by the Monte-carlo. The combined source modeling contribution to the energy scale uncertainty is 0.65%.

9.1.4 Other Sources of Energy Uncertainties

The detector PMT status uncertainty arises from the uncertainty in the $\text{PMT}_{\text{working}}$ number used in equation 9-1. A misidentification of the number working PMTs directly effects the energy response via equation 9-1. The electronics threshold and gain uncertainties arise from changes in the PMT threshold and electronics gain during the data running period. This uncertainty is determined by running ^{16}N source runs with the PMT voltages varied, and separately with the threshold for data acquisition varied. The electronics rate and time calibration uncertainty are determined by comparing the difference in energy response between high rate and low rate ^{16}N runs. This uncertainty needs to be included since the energy calibration is done through high rate ^{16}N data where as the neutrino data is low rate in comparison. Cross-talk is an effect where the PMTs near a hit PMT also fire due to electronic

pickup. This means that some events will appear to have a higher energy than their true energy. For events with a large energy (i.e. a lot of hit PMTs) the effect of cross-talk can be quite large. To check the energy response at higher energies the pT source, which generates 19.8MeV γ -rays is used. The total uncertainty attributed to cross-talk and non-linearity is 0.25%.

9.1.5 Summary of Energy Uncertainties

Table 9.4 and 9.5 summarize the total energy scale and energy width uncertainties.

Source	Uncertainty
Detector PMT status	0.20%
Electronics threshold	0.20%
Electronics gain	0.40%
Electronics rate effects	0.10%
Time calibration	0.10%
Time drift/stability	0.15%
Radial distribution	0.45%
Detector asymmetry	0.59%
^{16}N Source Modeling	0.65%
Cross-talk/pickup non-linearity	0.25%
Total	1.15%

Table 9.4: Contributions to the energy scale uncertainty from various sources.

Source	Uncertainty
Time stability	1.8%
Detector asymmetry	1.4%
Radial Dependence	0.8%
Total	3.4%

Table 9.5: Contributions to the energy resolution uncertainty from various sources.

9.2 Systematic Uncertainties on the β_{14} Isotropy Parameter

The uncertainty on the β_{14} isotropy parameter is determined through comparison of the ^{16}N and ^{252}Cf calibration sources with their respective Monte-carlo simulations. The β_{14} parameter is a measure of how isotropic the emitted light is for a given event and is described by equations 7-1 and 7-2. When comparing the ^{252}Cf data with Monte-carlo, the neutron events are selected from the ^{252}Cf data by using the burst analysis method described in section 5.2. The β_{14} parameter is strongly correlated with the energy of an event so in the neutrino signal extraction the energy and β_{14} parameter are combined in a single two-dimensional PDF. Just like for the determination of the energy systematics, a volume weighted difference between data and Monte-carlo is sought for the β_{14} parameter. The comparison between the data and Monte-carlo β_{14} distributions also accounts for any other possible sources of systematic uncertainties other than position and time variations. To do this Monte-carlo is compared with ^{16}N and ^{252}Cf source data at various radial positions. Figure 9.6 shows a comparison of the widths of the β_{14} distributions between ^{252}Cf data and Monte-carlo for source positions at various radii. Similarly, figure 9.7 shows the comparison of the means of the β_{14} distributions between data and Monte-carlo for the ^{16}N source. As for the energy systematics, we take the ratio of data to Monte-carlo and the volume weighted deviation from unity is taken as the uncertainty. Table 9.6 summarized the β_{14} systematic uncertainties from the ^{252}Cf and ^{16}N sources. The larger uncertainties from the ^{16}N source are used in the signal extraction. The reason the uncertainties derived from the ^{252}Cf source are much smaller than for the ^{16}N source may be attributed to differences between the single γ -ray β_{14} response between

data and Monte-carlo being averaged away over the multiple γ -rays produced in the neutron capture.

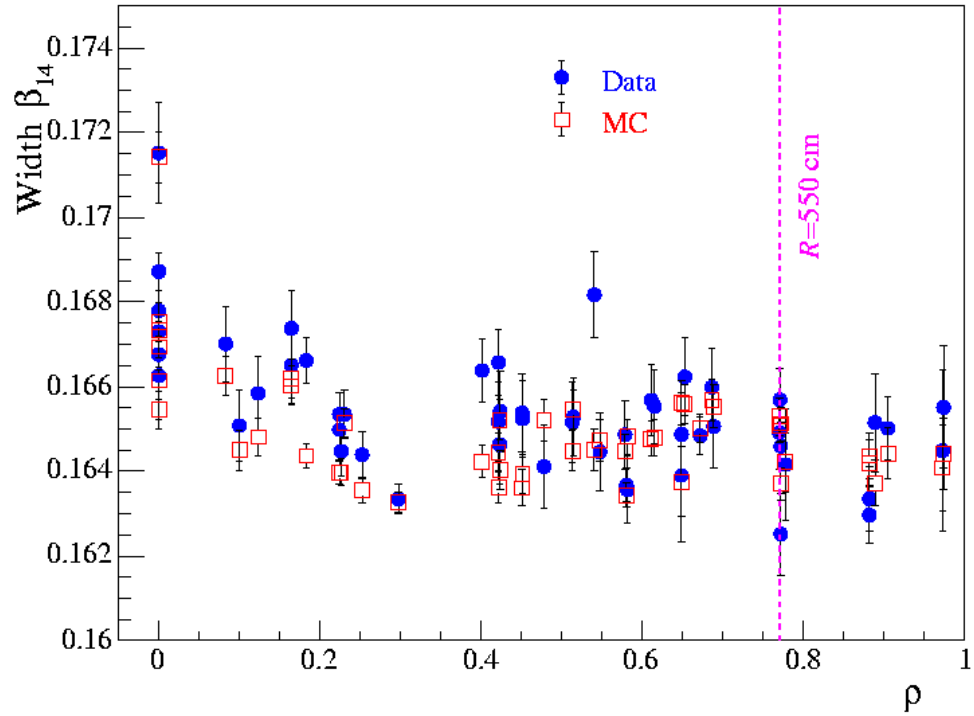


Figure 9.6: Comparison of the width of the β_{14} distributions for ^{252}Cf data and Monte-carlo at various radial positions of the source. Figure is taken from [1].

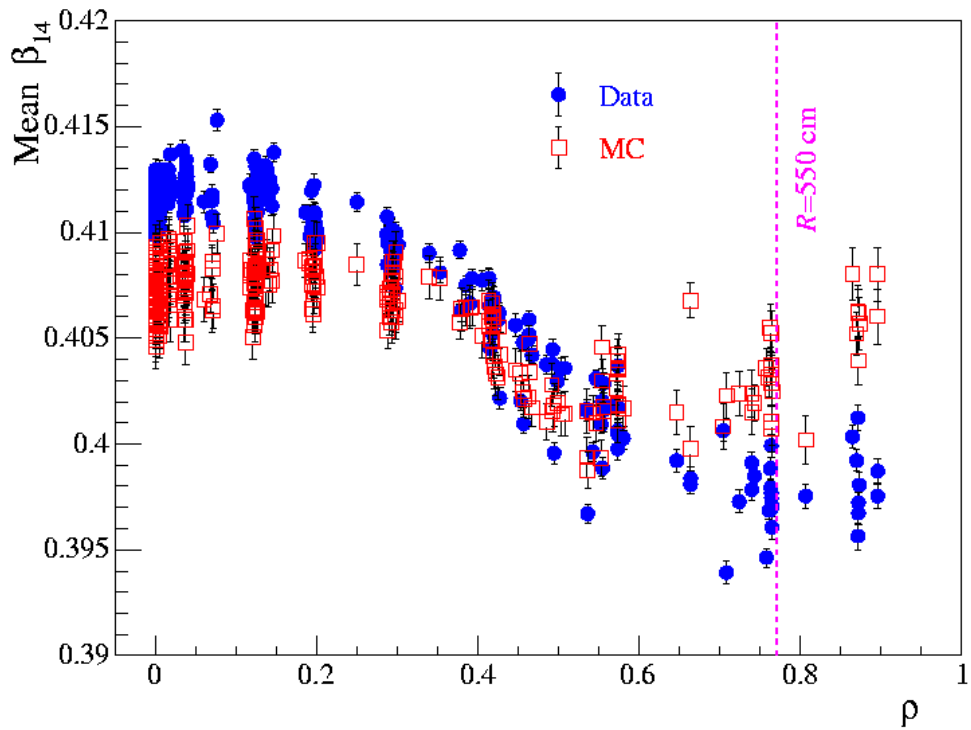


Figure 9.7: Comparison of the mean of the β_{14} distributions for ^{16}N data and Monte-carlo at various radial positions of the source. Figure is taken from [1].

Source	Mean	Resolution
^{252}Cf	0.48%	0.67%
^{16}N	0.85%	0.94%

Table 9.6: Uncertainties on the mean and resolution of the β_{14} parameter derived from the ^{16}N and ^{252}Cf sources . The uncertainty derived from the ^{16}N source is used in the signal extraction.

9.3 Angular Resolution Systematic Uncertainty

The uncertainty on the angular resolution is a factor in the uncertainty on the $\cos \theta_{sun}$ distribution which is the most powerful observable in extracting the number of ES events. The $\cos \theta_{sun}$ distribution is just the distribution of the angle between the fitted event direction and the direction to the sun. Therefore what we need to determine is an uncertainty on the fitted direction. Like the other systematic uncertainties, the ^{16}N source is employed to derive the uncertainty on the fitted direction. The angular distribution between the reconstructed direction and the true direction of an event can be parameterized by

$$R = N[e^{A_1(\cos \theta - 1)} + B e^{A_2(\cos \theta - 1)}] \quad (9-5)$$

where $\cos \theta$ is the angle between the fitted and true direction, N is a normalization, and the parameters $A_{1,2}$ and B are fitted using Monte-carlo electrons uniformly distributed in the detector. Equation 9-5 is fit to the angular distribution at various electron energies to determine the energy dependence of the parameters. The angular resolution distribution can also be generated from ^{16}N data. As done in [32], the angle between the true direction of the ^{16}N γ -ray and its reconstructed direction is given by

$$\cos \theta = (\vec{x} - \vec{s}) \cdot \vec{u}_{fit} / \|\vec{x} - \vec{s}\| \quad (9-6)$$

where

- \vec{x} is the reconstructed position of the event,
- \vec{s} is the position of the source, and
- \vec{u}_{fit} is the unit vector representing the reconstructed direction of the event.

For this technique to be accurate the distance from the source to the reconstructed event position must be much larger than the position uncertainty. To achieve this ^{16}N data that reconstructs more than 150cm from the source is chosen. The assumed true direction of the event is the direction from the source to the reconstructed position. Figure 9.8 shows a comparison between the angular resolution distribution of ^{16}N data and Monte-carlo.

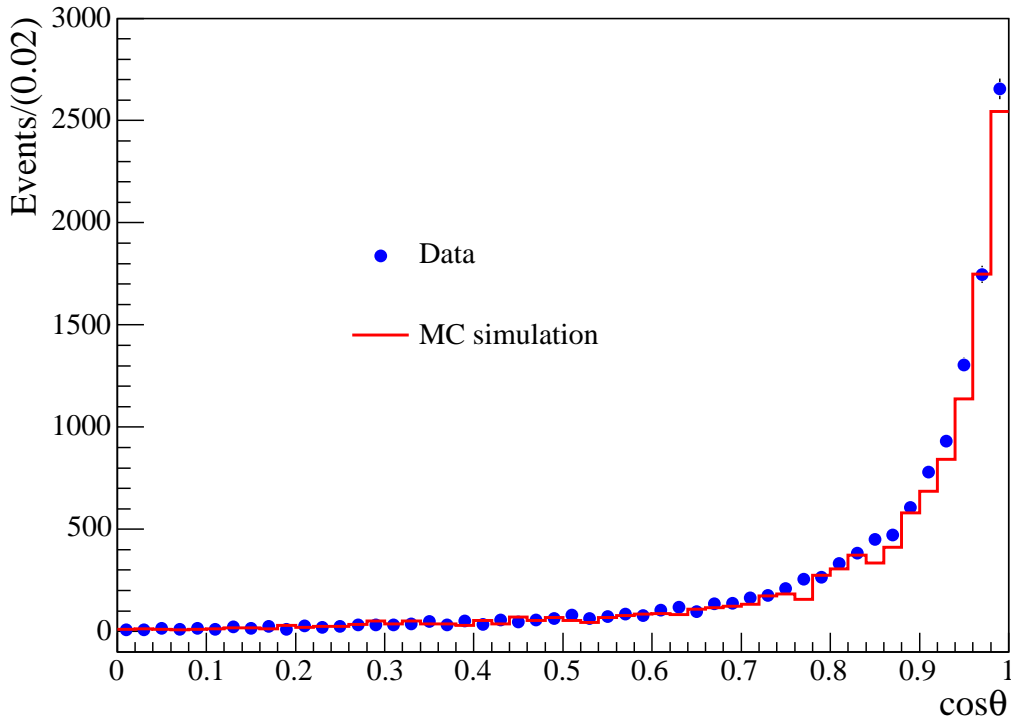


Figure 9.8: Comparison of the angular resolution distributions for ^{16}N data and Monte-carlo. Equation 9-6 is used to determine $\cos\theta$ and only events that reconstruct more than 150cm from the source are chosen.

From the data to Monte-carlo comparison for the ^{16}N source we can assign uncertainties on the parameters $A_{1,2}$ and B in the angular resolution function. Table 9.7

summarizes the uncertainties on the resolution function parameters.

Parameter	Uncertainty
A ₁	16%
A ₂	13%
B	31%

Table 9.7: Uncertainties on the angular resolution function parameters from equation 9-5.

The uncertainty on the angular resolution has to be propagated into the $\cos\theta_{sun}$ PDF. This is done by first smearing the event directions in all the signal and background Monte-carlos used to generate the PDFs. Since $\cos\theta_{sun}$ is a function of the angle between the event direction and the direction to the sun, perturbing the reconstructed event directions also perturbs the $\cos\theta_{sun}$ distribution. The event direction smearing is done by rotating the event direction about a smearing angle, $\cos\theta_{recon}$, where θ_{recon} is just the angle between the reconstructed direction before and after smearing. The $\cos\theta_{recon}$ value is chosen randomly from a Gaussian distribution with centre at 1 and width defined by the uncertainties on the angular resolution parameters A_{1,2} and B. Since the angular resolution parameters were found to have an energy dependence, the width of the Gaussian distribution has to include this energy dependence. The width of the Gaussian distribution used for smearing is then

$$Width = e^{-(2.93553+0.1448T_{eff})}$$

where T_{eff} is the reconstructed kinetic energy of the event.

9.4 Uncertainties on the Reconstructed Position

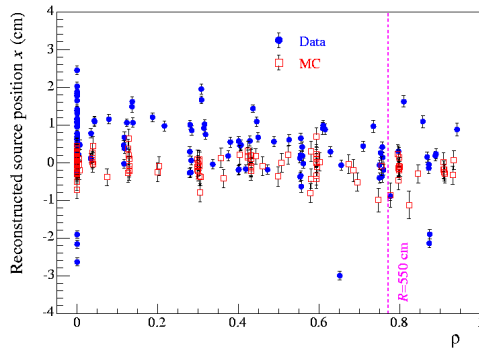
The position of an event is reconstructed using the times of the triggered PMTs for that given event. The PMT time calibration is done through a triggered Laserball calibration source which emits light isotropically at various possible optical wavelengths. The event position is reconstructed by minimizing the PMT time residual,

$$T_i^{res} = t_i - t_{fit} - \frac{r_{fit} - r_i}{u_{eff}} \quad (9-7)$$

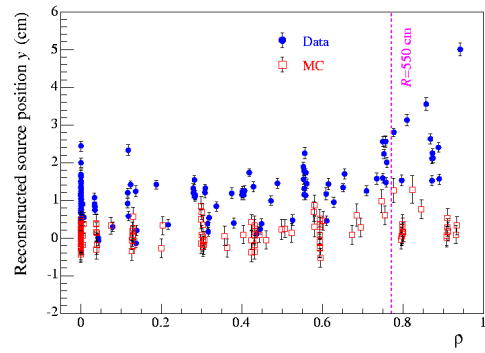
where t_i is the trigger time of the i^{th} PMT for the event and r_i is the PMT position. Similarly, t_{fit} and r_{fit} are the reconstructed time and position for the event, and u_{eff} is the speed of light in D₂O. For a wavelength of 380nm this is 21.87cm/ns.

Like the other systematic uncertainties, the systematic uncertainty for the position reconstruction is determined through comparison of ¹⁶N source data with Monte-carlo. The distribution of the reconstructed event positions in x, y, and z are fitted to Gaussian functions around their mean. The mean of the fitted Gaussians are taken to be the reconstructed source positions. Specifically what is compared is the difference between the mean of the reconstructed source position and the actual manipulator position. For source runs deployed in single axis mode the uncertainty on the manipulator position is assumed to be less than 2cm. Figure 9.9 shows the differences between the mean reconstructed event x, y, and z event positions and the manipulator positions for both ¹⁶N data and Monte-carlo. Overall there is about a 2cm difference between data and Monte-carlo in x and y and a 6cm overall difference in z. The radial scale uncertainty is taken to be 1%. The uncertainty on the radial resolution is taken as 15%.

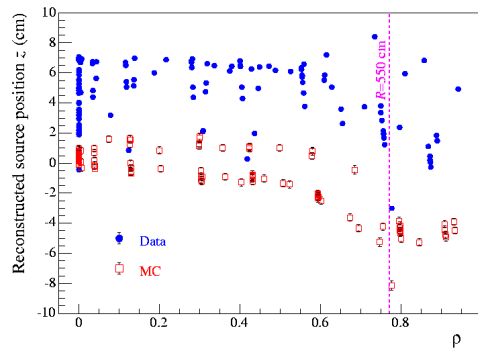
Most of the difference between the reconstructed ¹⁶N data and Monte-carlo can be attributed to an overall offset in the Laserball PMT calibration. The spread in



(a)



(b)



(c)

Figure 9.9: Comparison of the difference between the mean reconstructed event x , y , and z positions and the manipulator x , y , and z positions for ^{16}N source positions at various radii. The differences are shown for ^{16}N data and Monte-carlo. Figure is taken from [1].

the reconstructed positions can be attributed to changes in the PMT calibration over time. Since the Laserball position is one of the components that goes into the PMT calibration, the Laserball positions have been adjusted to attempt to remove the position offsets. To do this we look at changes in the PMT reconstruction times over the salt and pure D₂O running periods due to changes in the PMT calibration (PCA). For a given PMT, the time difference between an initial reference run and all subsequent runs is given by

$$\Delta t = t_i - t_{i0} \quad (9-8)$$

where t_i is the PMT time for PMT i for some subsequent run and t_{i0} is the PMT time for the same PMT at the initial reference run. We can approximate Δt by

$$\Delta t = \delta \frac{P_{x,y,z}}{c\|P\|} \quad (9-9)$$

where $P_{x,y,z}$ is the PMT x,y, or z position, $\|P\|$ is the distance to the PMT from centre (839cm), and c is the speed of light in water. A linear regression in x, y, and z gives δ , which is the x, y, or z offset due to the PCA. The Laserball position is then adjusted by this offset. Figure 9.10 shows the offsets in the z position due to the PMT timing calibration as a function of run number before and after the corrections to the Laserball positions are applied. Correcting the Laserball position therefore removes a large fraction of the PCA offset.

9.5 Uncertainties on the $\vec{U} \cdot \vec{R}$ Distribution

The $\vec{U} \cdot \vec{R}$ distribution is a measure of how inward or outward going an event is. An event with a $\vec{U} \cdot \vec{R}$ of 1 is going directly outward from centre and a $\vec{U} \cdot \vec{R}$ value of -1 means the event is going directly inward relative to the centre. The $\vec{U} \cdot \vec{R}$ distribution

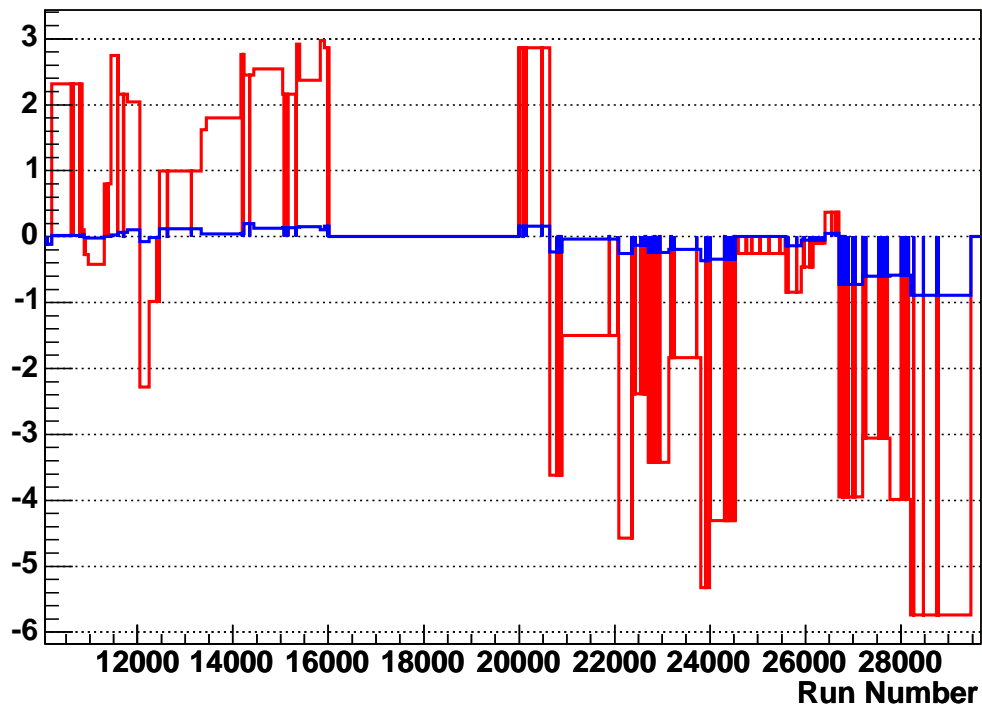


Figure 9.10: z position offsets (in cm) as a function of run number for both pure D₂O and salt phase running periods. The salt phase begins after run 20000. The red curve represents the offsets before any corrections and the blue curve are the offsets after the Laserball positions have been adjusted.

is derived from taking the inner product between the direction vector, $\vec{U} = (u, v, w)$, and the position vector, $\vec{R} = (x, y, z)$. Therefore uncertainties in the event direction and event position are propagated through to the $\vec{U} \cdot \vec{R}$ distribution. A direct measure of the $\vec{U} \cdot \vec{R}$ systematic uncertainty as done for the energy systematics through the ^{16}N source has not been done.

9.6 Monte Carlo Signal Extraction Studies

Before applying the maximum likelihood technique to the data the signal extraction was verified on a known sample of events. A Monte Carlo data set was generated with the same number of signal and background events as is expected in the real neutrino data. The Monte carlo data were generated by randomly sampling the PDFs used for the signal extraction. The signal extraction is performed on the Monte carlo data and the extracted CC and ES energy spectra are compared with the known number of events in the Monte carlo data for the neutrino signals. To test if there are no biases in the extracted number of events we generate many Monte carlo data samples and verify that the extracted number of events is statistically spread about the number of events actually in the data samples. Figure 9.11 shows the extracted number of CC and ES events for about a hundred Monte carlo data sets. The number of CC and ES events are extracted for every 0.5MeV bin between 4MeV and 13MeV. The blue points are the fitted number of events and the solid curves are the number of events in the Monte carlo data per 0.5MeV bin. Panel (c) of 9.11 shows the average of the fitted CC events for every 0.5MeV bin. It is clear that there is no apparent bias in the extracted number of events.

As another check that the signal extraction algorithm is working properly, the

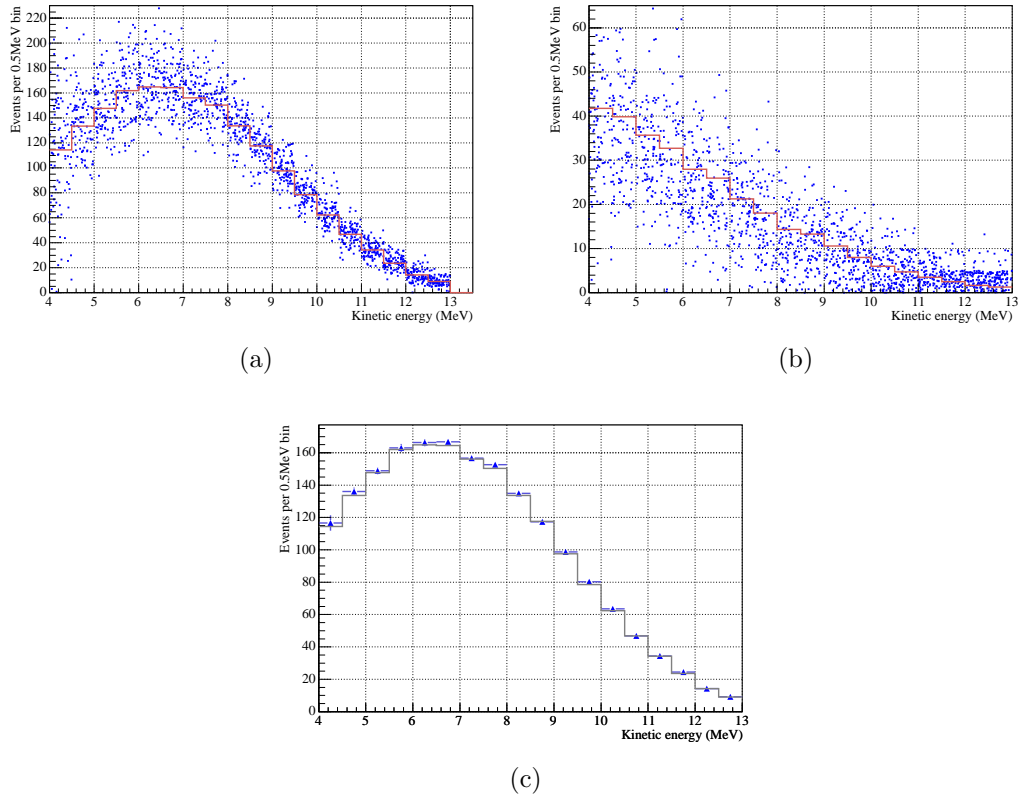


Figure 9.11: Extracted CC (panel (a)) and ES (panel (b)) spectra from Monte carlo data sets. The points are the extracted number of CC and ES events per 0.5MeV energy bin for about 100 Monte carlo data sets. The solid lines are the actual generated number of events in the data set. Panel (c) shows the average of the extracted number of events from panel (a). There is good agreement between the fitted number of events and the number of events in the data sets.

fitted energy, β_{14} , and $\cos \theta_{sun}$ distributions are shown for a Monte carlo data set in figure 9.12 and compared with the Monte-carlo data. Also shown in the fit plots are the extracted distributions for the three neutrino signals and the dominant back-grounds.

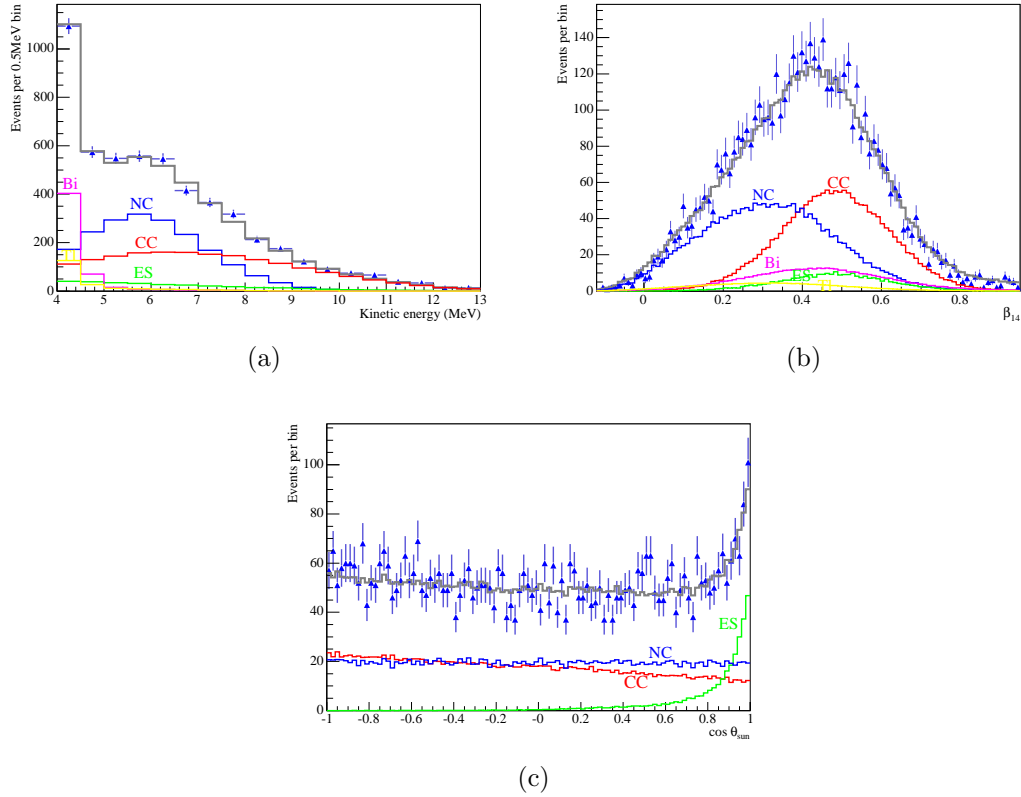
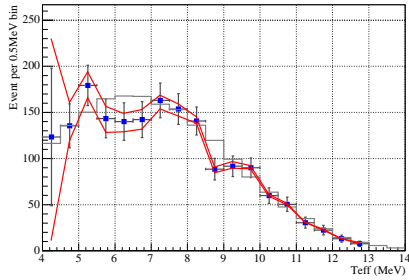


Figure 9.12: The fitted energy (panel a), β_{14} (panel b), and $\cos \theta_{sun}$ (panel c) distributions to the Monte carlo data. The points are the Monte carlo data and the solid lines are the fits to the data. The three neutrino signals and the dominant background distributions are shown. The fits are done in the shape unconstrained mode.

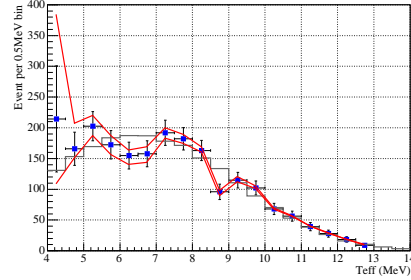
9.7 Extracted ES and CC Spectra

The number of ES and CC events were extracted for every 0.5MeV bin between 4MeV and 14MeV by relying on the β_{14} isotropy distribution. We can also do the constrained fit in which we hypothesize that the ES and CC energy spectra are fixed to the ^8B spectrum, and the total number of ES and CC events are determined. Since we have added an additional PDF that is quite different for ES, CC and NC events, the uncertainties on the extracted event numbers are smaller for the constrained than the unconstrained fit. Figures 9.13 and 9.14 show the extracted CC and ES energy spectra for various radial acceptance regions. The error bars on the points represent the statistical uncertainties and the red lines represent the limits of the systematic uncertainties. To verify the quality of the fit the extracted energy, β_{14} , and $\cos\theta_{sun}$, and radial distributions are compared to the data. Figure 9.15 shows the fit compared to the data for the neutrino signal extraction. Also shown are the components of the fit from the neutrino signals and the dominant background PDFs.

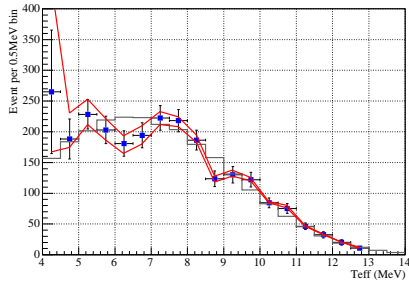
Tables 9.8, 9.9, 9.10, and 9.11 show the extracted number of CC and ES events for 476cm and 550cm radial acceptance regions. The extracted event numbers are for 0.5MeV bin widths. The contributions from the various systematic uncertainties are also listed in the tables. It is evident that for the lowest energy bins the systematic uncertainties become very large. This can be explained by the large background to signal ratio in the lowest energy bins. As the energy PDFs are perturbed within their systematic uncertainties the number of low energy background events changes greatly since the background energy distributions peak very sharply at lower energies. Since the CC and ES energy shapes are unconstrained there is a large correlation between background events and the CC or ES signals, therefore a large change in the number of



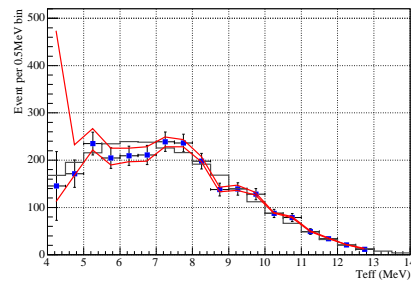
(a) R=476cm



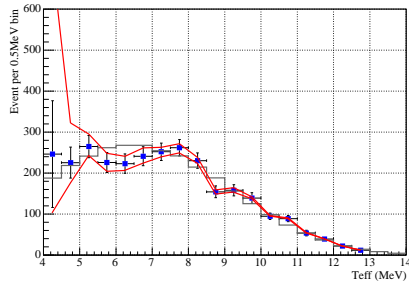
(b) R=505cm



(c) R=536cm

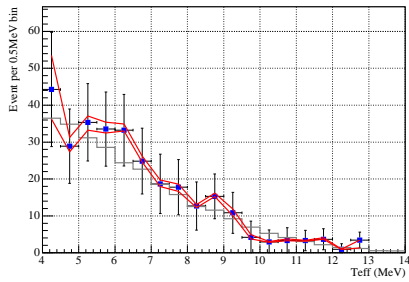


(d) R=550cm

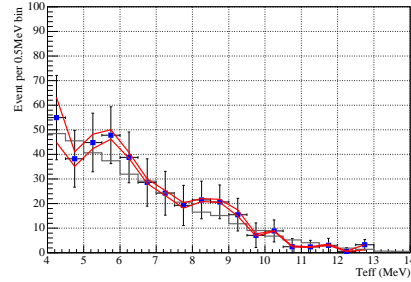


(e) R=576cm

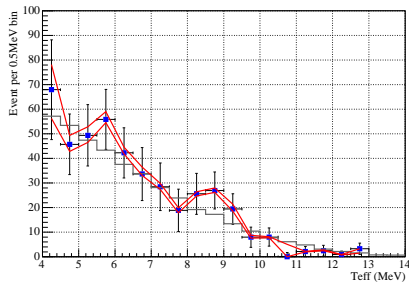
Figure 9.13: Extracted CC spectra for various fiducial radii. Red curves are the systematic uncertainty limits, the points are the extracted spectra, and the solid line is the undistorted CC spectrum.



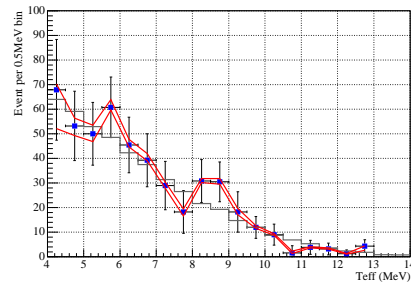
(a) R=476cm



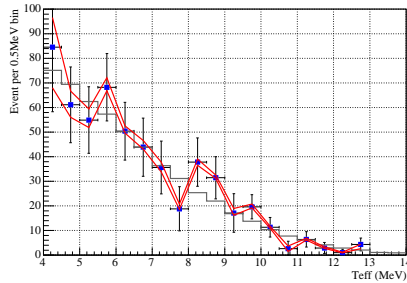
(b) R=505cm



(c) R=536cm



(d) R=550cm



(e) R=576cm

Figure 9.14: Extracted ES spectra for various fiducial radii. Red curves are the systematic uncertainty limits, the points are the extracted spectra, and the solid line is the undistorted ES spectrum.

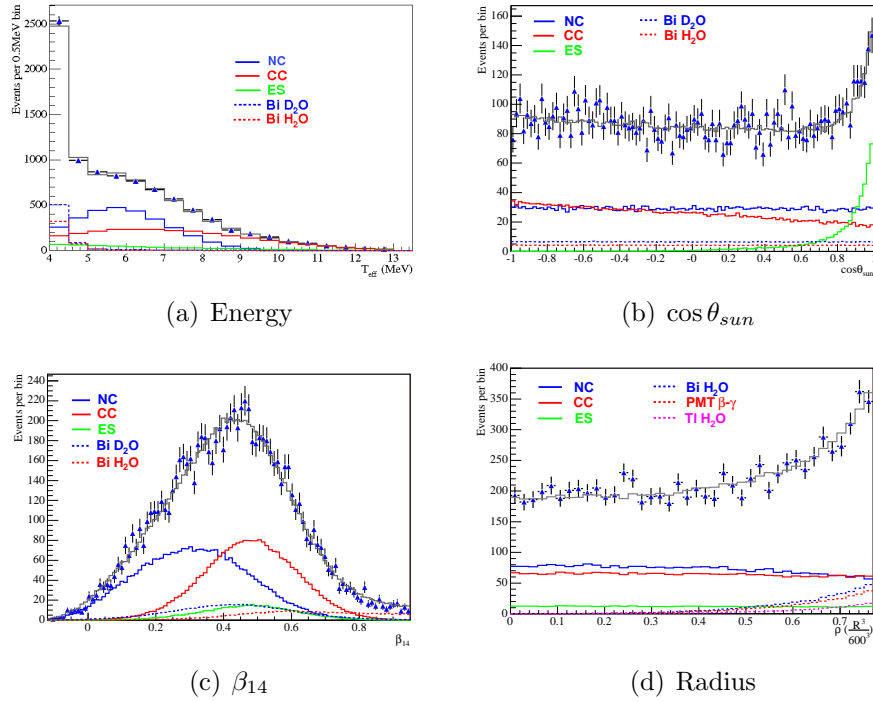


Figure 9.15: The neutrino data fitted with the neutrino and background PDFs. Shown are the fits in the energy, β_{14} , and $\cos \theta_{sun}$, and radial distributions. Only the dominant backgrounds are shown for the fits in panels a, b, and c. For the radial fit, the dominant external backgrounds are shown since the internal backgrounds have a very similar radial distribution to the neutrino signals. The fits are done in a fiducial volume of 550cm.

background events influences the extracted number of signal events. The systematic uncertainties are not as dominant for the ES events as they are for the CC events due to their unique $\cos \theta_{sun}$ distribution.

Bin (MeV)	Fit	E	σ_E	β_{14}	$\sigma_{\beta_{14}}$	R	σ_R	σ_{Ang}	σ_{sys}	σ_{total}
4-4.5	123.3 ± 74.6	+32.5 -39.4	+73.1 -73.1	+0.0 -19.2	+11.2 -11.2	+11.5 -0.7	+2.9 -2.9	± 2.9	+81.7 -86.1	+101.6 -105.2
4.5-5	135.5 ± 23.8	+0.0 -2.7	+16.2 -16.2	+5.4 -7.8	+3.3 -3.3	+1.7 -0.5	+1.8 -1.8	± 0.1	+17.6 -18.6	+24.9 -25.6
5-5.5	179.3 ± 21.9	+4.5 -4.7	+4.7 -4.7	+5.6 -4.2	+1.4 -1.4	+0.7 -0.6	+0.7 -0.7	± 0.3	+8.8 -8.0	+15.0 -14.6
5.5-6	143.4 ± 21.0	+5.2 -5.2	+3.5 -3.5	+8.7 -7.6	+0.4 -0.4	+0.6 -0.0	+0.1 -0.1	± 0.3	+10.8 -9.9	+18.1 -17.6
6-6.5	140.1 ± 20.4	+2.4 -3.2	+1.7 -1.7	+6.9 -5.1	+0.5 -0.5	+1.1 -0.0	+2.1 -2.1	± 0.1	+7.9 -6.6	+16.6 -16.0
6.5-7	142.2 ± 19.5	+1.9 -0.2	+4.1 -4.1	+5.8 -7.2	+0.4 -0.4	+0.0 -0.5	+0.3 -0.3	± 0.1	+7.4 -8.3	+15.6 -16.1
7-7.5	163.0 ± 18.8	+1.6 -1.2	+0.5 -0.5	+4.9 -2.7	+2.2 -2.2	+1.1 -0.1	+0.9 -0.9	± 0.0	+5.8 -3.8	+12.9 -12.2
7.5-8	153.7 ± 16.7	+2.6 -3.3	+0.4 -0.4	+3.5 -1.6	+2.2 -2.2	+0.6 -0.0	+0.7 -0.7	± 0.0	+5.0 -4.3	+12.0 -11.7
8-8.5	140.6 ± 15.2	+0.8 -1.7	+1.2 -1.2	+1.7 -2.1	+0.0 -0.0	+0.2 -0.1	+0.1 -0.1	± 0.1	+2.3 -3.0	+11.0 -11.2
8.5-9	88.5 ± 11.8	+3.8 -1.5	+1.6 -1.6	+3.0 -2.0	+0.3 -0.3	+0.1 -0.0	+0.6 -0.6	± 0.6	+5.2 -3.1	+14.3 -13.7
9-9.5	91.7 ± 11.2	+2.3 -3.0	+3.5 -3.5	+1.2 -1.0	+0.9 -0.9	+0.2 -0.0	+0.4 -0.4	± 0.3	+4.5 -4.8	+13.0 -13.1
9.5-10	90.0 ± 10.6	+1.6 -0.3	+2.0 -2.0	+0.0 -0.5	+1.0 -1.0	+0.0 -0.2	+0.2 -0.2	± 0.8	+2.9 -2.4	+12.1 -12.0
10-10.5	59.9 ± 8.4	+0.3 -1.5	+0.6 -0.6	+0.6 -0.0	+1.0 -1.0	+0.1 -0.1	+0.0 -0.0	± 0.2	+1.3 -1.9	+14.1 -14.1
10.5-11	50.4 ± 7.8	+1.1 -0.3	+0.1 -0.1	+0.1 -0.0	+0.8 -0.8	+0.0 -0.2	+0.1 -0.1	± 0.7	+1.6 -1.2	+15.5 -15.4
11-11.5	30.5 ± 5.9	+0.1 -0.2	+0.9 -0.9	+0.0 -0.6	+0.3 -0.3	+0.4 -0.0	+0.3 -0.3	± 0.2	+1.1 -1.2	+19.4 -19.4
11.5-12	22.3 ± 5.2	+0.0 -0.1	+0.2 -0.2	+0.0 -0.0	+0.8 -0.8	+0.2 -0.0	+0.2 -0.2	± 1.8	+2.0 -2.0	+23.2 -23.2
12-12.5	13.1 ± 3.8	+0.0 -0.6	+0.6 -0.6	+0.0 -0.0	+0.0 -0.0	+0.0 -0.2	+0.1 -0.1	± 0.7	+0.9 -1.1	+29.0 -29.0
12.5-13	7.6 ± 3.0	+3.1 -0.0	+12.5 -12.5	+3.1 -12.5	+3.2 -3.2	+0.4 -0.0	+0.1 -0.1	± 0.1	+13.7 -18.0	+41.7 -43.3

Table 9.8: Extracted number of CC events for an ES and CC unconstrained fit for events with reconstructed radius less than 476cm. Shown are the extracted number of ES events per 0.5MeV bin with the first bin being 4.0MeV-4.5MeV. The systematic uncertainties from energy scale (E), energy resolution (σ_E), β_{14} scale (β_{14}), β_{14} resolution ($\sigma_{\beta_{14}}$), radial scale (R), radial resolution (σ_R), and angular resolution (σ_{Ang}). The total systematic uncertainty (σ_{sys}) and total uncertainty (σ_{total}) are given in the last 2 columns.

Bin (MeV)	Fit	E	σ_E	β_{14}	$\sigma_{\beta_{14}}$	R	σ_R	σ_{Ang}	σ_{sys}	σ_{total}
4-4.5	44.3 \pm 15.5	+5.4 -7.2	+16.3 -16.3	+0.0 -2.6	+1.1 -1.1	+3.4 -0.0	+1.2 -1.2	\pm 13.2	+22.0 -22.4	+41.3 -41.5
4.5-5	28.9 \pm 10.1	+0.3 -1.8	+3.6 -3.6	+4.2 -2.3	+4.4 -4.4	+0.0 -2.1	+0.3 -0.3	\pm 5.3	+8.8 -8.5	+36.0 -36.0
5-5.5	35.4 \pm 10.5	+0.6 -1.3	+2.7 -2.7	+1.7 -5.2	+0.4 -0.4	+0.2 -0.2	+0.1 -0.1	\pm 4.5	+5.5 -7.5	+30.2 -30.6
5.5-6	33.6 \pm 10.1	+1.1 -1.6	+1.0 -1.0	+2.5 -2.0	+1.5 -1.5	+0.0 -0.6	+1.1 -1.1	\pm 4.6	+5.7 -5.7	+30.5 -30.5
6-6.5	33.2 \pm 9.7	+0.2 -0.4	+1.9 -1.9	+2.7 -0.0	+2.6 -2.6	+0.6 -0.5	+0.3 -0.3	\pm 2.7	+5.1 -4.3	+29.6 -29.5
6.5-7	24.8 \pm 8.9	+0.1 -0.0	+0.4 -0.4	+0.5 -0.9	+3.5 -3.5	+0.3 -0.4	+0.2 -0.2	\pm 4.0	+5.4 -5.4	+36.3 -36.3
7-7.5	18.7 \pm 8.1	+2.7 -0.0	+4.0 -4.0	+1.8 -3.7	+1.2 -1.2	+0.4 -0.1	+0.7 -0.7	\pm 2.8	+6.0 -6.3	+43.6 -43.6
7.5-8	17.8 \pm 7.5	+0.8 -4.0	+1.2 -1.2	+3.0 -1.7	+0.6 -0.6	+0.0 -1.7	+4.1 -4.1	\pm 1.8	+5.6 -6.6	+42.5 -42.7
8-8.5	12.7 \pm 6.5	+2.1 -0.0	+0.5 -0.5	+1.4 -1.5	+1.5 -1.5	+0.5 -1.9	+1.3 -1.3	\pm 1.9	+3.7 -3.7	+51.6 -51.6
8.5-9	15.3 \pm 6.1	+1.3 -0.0	+0.7 -0.7	+2.0 -0.0	+1.6 -1.6	+0.3 -0.0	+0.6 -0.6	\pm 4.7	+5.6 -5.0	+40.0 -39.9
9-9.5	10.8 \pm 5.6	+4.0 -1.6	+5.9 -5.9	+5.4 -1.6	+3.6 -3.6	+0.0 -0.7	+1.7 -1.7	\pm 6.0	+11.4 -9.6	+52.6 -52.2
9.5-10	4.2 \pm 4.4	+0.0 -5.5	+4.2 -4.2	+2.4 -5.7	+3.6 -3.6	+1.6 -0.0	+3.3 -3.3	\pm 16.7	+18.2 -19.6	+106.6 -106.9
10-10.5	2.9 \pm 3.2	+1.9 -2.1	+2.0 -2.0	+0.2 -0.0	+1.5 -1.5	+2.0 -0.0	+1.0 -1.0	\pm 4.0	+5.6 -5.2	+109.9 -109.9
10.5-11	3.3 \pm 3.5	+0.8 -0.0	+0.1 -0.1	+2.2 -1.6	+2.7 -2.7	+1.9 -0.0	+1.1 -1.1	\pm 11.7	+12.4 -12.1	+105.2 -105.1
11-11.5	3.3 \pm 2.8	+0.7 -0.1	+0.7 -0.7	+1.9 -0.0	+1.8 -1.8	+0.0 -3.8	+3.0 -3.0	\pm 1.1	+4.3 -5.3	+83.8 -83.9
11.5-12	3.7 \pm 2.8	+0.1 -0.1	+0.2 -0.2	+0.0 -0.1	+0.3 -0.3	+0.0 -0.9	+1.2 -1.2	\pm 10.8	+10.9 -10.9	+78.5 -78.5
12-12.5	0.9 \pm 1.5	+0.7 -0.0	+0.9 -0.9	+0.4 -0.0	+0.2 -0.2	+3.5 -0.0	+1.4 -1.4	\pm 8.1	+9.0 -8.2	+161.5 -161.5
12.5-13	3.4 \pm 2.2	+0.1 -36.0	+1.5 -1.5	+0.0 -36.1	+35.9 -35.9	+0.0 -0.7	+0.2 -0.2	\pm 0.1	+36.0 -62.4	+165.2 -172.9

Table 9.9: Extracted number of ES events for an ES and CC unconstrained fit for events with reconstructed radius less than 476cm. Shown are the extracted number of ES events per 0.5MeV bin with the first bin being 4.0MeV-4.5MeV. The systematic uncertainties from energy scale (E), energy resolution (σ_E), β_{14} scale (β_{14}), β_{14} resolution ($\sigma_{\beta_{14}}$), radial scale (R), radial resolution (σ_R), and angular resolution (σ_{Ang}). The total systematic uncertainty (σ_{sys}) and total uncertainty (σ_{total}) are given in the last 2 columns.

Bin (MeV)	Fit	E	σ_E	β_{14}	$\sigma_{\beta_{14}}$	R	σ_R	σ_{Ang}	σ_{sys}	σ_{total}
4-4.5	145.5 \pm 72.9	+23.4 -97.8	+93.8 -93.8	+0.0 -107.3	+42.6 -42.6	+0.0 -40.7	+25.4 -25.4	\pm 96.2	+145.2 -208.0	+153.6 -213.9
4.5-5	171.5 \pm 29.1	+1.7 -8.0	+23.7 -23.7	+0.0 -14.3	+8.0 -8.0	+0.0 -4.6	+1.2 -1.2	\pm 13.0	+28.3 -33.0	+33.0 -37.1
5-5.5	235.1 \pm 24.2	+4.0 -6.2	+9.3 -9.3	+3.1 -6.7	+1.2 -1.2	+0.0 -0.8	+0.0 -0.0	\pm 2.3	+10.8 -13.3	+14.9 -16.8
5.5-6	204.4 \pm 21.9	+5.0 -4.7	+0.5 -0.5	+5.3 -8.7	+2.3 -2.3	+0.7 -0.5	+1.0 -1.0	\pm 0.7	+7.7 -10.2	+13.2 -14.8
6-6.5	209.3 \pm 20.4	+2.4 -2.8	+1.7 -1.7	+5.9 -6.1	+1.6 -1.6	+0.2 -0.2	+0.1 -0.1	\pm 0.6	+6.8 -7.2	+11.9 -12.1
6.5-7	210.9 \pm 20.2	+1.1 -1.6	+3.0 -3.0	+5.7 -7.4	+0.1 -0.1	+0.4 -0.6	+1.1 -1.1	\pm 0.5	+6.7 -8.3	+11.7 -12.7
7-7.5	239.0 \pm 20.4	+2.1 -1.5	+1.2 -1.2	+4.1 -3.6	+0.1 -0.1	+0.4 -0.0	+0.7 -0.7	\pm 0.5	+4.9 -4.2	+9.8 -9.5
7.5-8	236.5 \pm 18.6	+2.5 -2.2	+0.9 -0.9	+2.8 -1.6	+0.1 -0.1	+0.0 -0.2	+0.4 -0.4	\pm 0.3	+3.9 -2.9	+8.8 -8.4
8-8.5	198.0 \pm 16.5	+0.8 -2.5	+2.2 -2.2	+1.0 -3.0	+1.0 -1.0	+0.2 -0.1	+0.0 -0.0	\pm 0.5	+2.8 -4.6	+8.8 -9.6
8.5-9	138.0 \pm 13.4	+3.4 -1.9	+0.6 -0.6	+1.2 -2.0	+0.6 -0.6	+0.2 -0.5	+0.3 -0.3	\pm 0.6	+3.7 -3.0	+10.4 -10.2
9-9.5	139.2 \pm 13.0	+1.9 -3.0	+3.5 -3.5	+1.2 -1.3	+0.4 -0.4	+0.0 -0.1	+0.2 -0.2	\pm 0.5	+4.3 -4.9	+10.3 -10.5
9.5-10	128.3 \pm 11.9	+1.4 -1.1	+2.4 -2.4	+0.5 -0.4	+0.9 -0.9	+0.0 -0.1	+0.2 -0.2	\pm 0.5	+3.0 -2.8	+9.7 -9.7
10-10.5	87.5 \pm 8.7	+0.3 -0.6	+1.1 -1.1	+0.5 -0.4	+0.4 -0.4	+0.1 -0.1	+0.2 -0.2	\pm 0.3	+1.4 -1.4	+10.0 -10.0
10.5-11	78.7 \pm 8.4	+0.7 -0.2	+0.3 -0.3	+0.0 -0.6	+0.4 -0.4	+0.1 -0.1	+0.2 -0.2	\pm 0.3	+0.9 -0.9	+10.7 -10.7
11-11.5	49.1 \pm 6.1	+0.0 -0.3	+0.0 -0.0	+0.6 -0.3	+0.9 -0.9	+0.8 -0.0	+1.1 -1.1	\pm 0.3	+1.7 -1.5	+12.5 -12.5
11.5-12	33.8 \pm 5.1	+0.2 -0.0	+0.1 -0.1	+0.0 -0.1	+0.1 -0.1	+0.2 -0.0	+0.1 -0.1	\pm 1.4	+1.4 -1.4	+15.2 -15.2
12-12.5	20.8 \pm 4.4	+0.1 -0.2	+0.3 -0.3	+0.0 -0.2	+0.1 -0.1	+0.0 -0.3	+0.1 -0.1	\pm 0.1	+0.3 -0.5	+21.4 -21.4
12.5-13	11.7 \pm 3.6	+1.8 -0.0	+8.1 -8.1	+0.0 -8.0	+1.8 -1.8	+0.0 -0.1	+0.2 -0.2	\pm 0.2	+8.5 -11.6	+32.2 -33.2

Table 9.10: Extracted number of CC events for an ES and CC unconstrained fit for events with reconstructed radius less than 550cm. Shown are the extracted number of ES events per 0.5MeV bin with the first bin being 4.0MeV-4.5MeV. The systematic uncertainties from energy scale (E), energy resolution (σ_E), β_{14} scale (β_{14}), β_{14} resolution ($\sigma_{\beta_{14}}$), radial scale (R), radial resolution (σ_R), and angular resolution (σ_{Ang}). The total systematic uncertainty (σ_{sys}) and total uncertainty (σ_{total}) are given in the last 2 columns.

Bin (MeV)	Fit	E	σ_E	β_{14}	$\sigma_{\beta_{14}}$	R	σ_R	σ_{Ang}	σ_{sys}	σ_{total}
4-4.5	67.9 ± 20.5	+2.5 -12.4	+12.5 -12.5	+0.0 -11.3	+0.1 -0.1	+0.5 -7.1	+5.8 -5.8	± 2.4	+14.2 -23.0	+33.4 -37.9
4.5-5	53.2 ± 14.1	+1.1 -2.2	+5.6 -5.6	+0.5 -0.8	+3.3 -3.3	+0.0 -2.9	+0.8 -0.8	± 4.8	+8.2 -8.9	+27.7 -27.9
5-5.5	50.0 ± 12.8	+1.1 -2.3	+3.2 -3.2	+1.2 -4.3	+0.4 -0.4	+0.5 -0.1	+0.7 -0.7	± 6.7	+7.6 -8.9	+26.6 -27.0
5.5-6	60.8 ± 12.3	+1.8 -1.4	+0.1 -0.1	+2.0 -0.2	+1.2 -1.2	+0.0 -0.4	+0.4 -0.4	± 4.4	+5.3 -4.8	+20.9 -20.8
6-6.5	45.5 ± 11.3	+0.8 -0.5	+2.4 -2.4	+1.8 -0.3	+2.4 -2.4	+0.3 -0.9	+0.5 -0.5	± 3.0	+5.0 -4.7	+25.3 -25.3
6.5-7	39.2 ± 10.8	+0.5 -0.1	+1.8 -1.8	+1.4 -0.0	+3.0 -3.0	+0.4 -0.3	+0.1 -0.1	± 5.9	+7.0 -6.8	+28.4 -28.3
7-7.5	29.0 ± 9.8	+1.2 -0.0	+2.6 -2.6	+2.0 -3.2	+0.8 -0.8	+0.0 -1.3	+0.9 -0.9	± 3.5	+5.0 -5.7	+34.3 -34.4
7.5-8	18.2 ± 8.7	+1.1 -4.5	+2.3 -2.3	+2.9 -5.0	+1.9 -1.9	+0.0 -1.3	+4.4 -4.4	± 5.3	+8.0 -10.1	+48.2 -48.6
8-8.5	30.8 ± 8.7	+0.7 -0.6	+0.1 -0.1	+1.2 -1.3	+1.2 -1.2	+0.4 -0.8	+0.0 -0.0	± 2.8	+3.3 -3.4	+28.5 -28.5
8.5-9	30.5 ± 8.1	+1.0 -1.5	+2.6 -2.6	+2.1 -0.0	+1.0 -1.0	+0.0 -0.6	+0.7 -0.7	± 3.2	+4.9 -4.6	+27.0 -27.0
9-9.5	18.2 ± 8.2	+0.0 -2.0	+5.5 -5.5	+4.8 -1.7	+3.5 -3.5	+0.8 -0.0	+0.3 -0.3	± 5.1	+9.6 -8.6	+46.0 -45.8
9.5-10	11.9 ± 4.4	+0.0 -1.3	+0.2 -0.2	+1.2 -0.9	+1.0 -1.0	+0.0 -2.1	+0.8 -0.8	± 5.2	+5.5 -6.0	+37.5 -37.6
10-10.5	9.0 ± 4.3	+0.4 -0.8	+0.2 -0.2	+0.0 -1.2	+0.3 -0.3	+0.0 -0.4	+0.9 -0.9	± 2.1	+2.4 -2.8	+47.6 -47.6
10.5-11	1.6 ± 2.9	+2.9 -6.2	+7.8 -7.8	+25.1 -0.0	+7.2 -7.2	+3.1 -8.5	+12.1 -12.1	± 10.2	+31.8 -21.8	+190.5 -189.1
11-11.5	3.8 ± 2.8	+1.1 -0.0	+2.1 -2.1	+0.2 -2.3	+3.5 -3.5	+0.0 -5.1	+4.1 -4.1	± 4.7	+7.6 -9.4	+73.7 -73.9
11.5-12	3.2 ± 2.4	+0.0 -0.7	+0.3 -0.3	+1.0 -0.0	+1.2 -1.2	+0.0 -2.0	+1.5 -1.5	± 14.4	+14.6 -14.7	+77.3 -77.4
12-12.5	1.2 ± 1.6	+0.0 -0.8	+7.1 -7.1	+2.3 -0.2	+1.4 -1.4	+5.3 -0.0	+1.4 -1.4	± 2.2	+9.6 -7.7	+128.6 -128.5
12.5-13	4.4 ± 2.6	+0.0 -27.8	+1.4 -1.4	+0.0 -1.3	+27.7 -27.7	+0.1 -0.1	+0.5 -0.5	± 0.4	+27.7 -39.3	+131.2 -134.1

Table 9.11: Extracted number of ES events for an ES and CC unconstrained fit for events with reconstructed radius less than 550cm. Shown are the extracted number of ES events per 0.5MeV bin with the first bin being 4.0MeV-4.5MeV. The systematic uncertainties from energy scale (E), energy resolution (σ_E), β_{14} scale (β_{14}), β_{14} resolution ($\sigma_{\beta_{14}}$), radial scale (R), radial resolution (σ_R), and angular resolution (σ_{Ang}). The total systematic uncertainty (σ_{sys}) and total uncertainty (σ_{total}) are given in the last 2 columns.

9.8 Extracted Neutral Current and Background Events

The NC signals and the background distributions are not dependent on the shape of the ^8B neutrino energy spectrum. Therefore these signals can be extracted with their energy shapes fixed and the extracted number of events is the total number of events throughout the whole energy range not just for an individual 0.5MeV bin. The number of events for a given energy bin can then be interpolated since we know the shapes of the energy distributions of these signals very well. Table 9.12 and 9.12 show the fitted NC and background events for 476cm and 550cm fiducial volumes respectively. The systematic uncertainties are also included.

	Fit	E	σ_E	β_{14}	$\sigma_{\beta_{14}}$	R	σ_R	σ_{Ang}	σ_{sys}	σ_{total}
nc	1992.6 ± 92.7	+1.6 -1.5	+2.6 -2.6	+3.5 -5.8	+0.2 -0.2	+0.0 -0.4	+0.4 -0.4	± 0.2	+4.7 -6.6	+6.6 -8.1
Bi	506.1 ± 97.8	+13.2 -10.2	+22.6 -22.6	+5.2 -0.2	+0.9 -0.9	+0.0 -2.5	+3.0 -3.0	± 2.3	+27.0 -25.3	+33.2 -31.8
Bi H2O	38.6 ± 16.1	+0.0 -17.7	+2.8 -2.8	+16.4 -9.3	+12.9 -12.9	+10.6 -7.1	+20.0 -20.0	± 1.7	+30.9 -32.1	+51.8 -52.5
Bi AV	17.4 ± 19.4	+84.0 -47.9	+36.7 -2.8	+88.1 -0.0	+31.2 -31.2	+51.4 -28.9	+15.1 -15.1	± 0.3	+141.5 -75.3	+180.1 -134.6
Tl	210.2 ± 113.0	+0.0 -21.8	+35.8 -35.8	+29.7 -2.2	+21.5 -21.5	+1.1 -1.5	+2.3 -2.3	± 0.8	+51.3 -47.2	+74.3 -71.6
Tl H2O	13.9 ± 7.3	+6.8 -10.9	+42.0 -42.0	+17.6 -21.1	+19.6 -19.6	+11.1 -4.3	+8.0 -8.0	± 1.9	+52.0 -52.9	+74.1 -74.7
Tl AV	41.0 ± 29.4	+46.8 -22.6	+32.6 -32.6	+0.0 -36.9	+41.8 -41.8	+8.9 -39.1	+29.3 -29.3	± 5.0	+77.2 -84.2	+105.4 -110.6
Na24	111.8 ± 91.6	+48.8 -0.0	+29.3 -29.3	+6.9 -43.1	+17.1 -17.1	+4.8 -0.0	+6.4 -6.4	± 3.0	+60.4 -55.3	+101.8 -98.8
Pmt	34.2 ± 12.4	+4.4 -22.2	+85.8 -85.8	+30.3 -10.5	+6.1 -6.1	+0.0 -9.9	+15.9 -15.9	± 0.5	+92.7 -91.4	+99.6 -98.4
Extn	46.9 ± 41.2	+14.5 -16.4	+67.8 -67.8	+59.5 -8.4	+59.4 -59.4	+17.7 -0.0	+11.7 -11.7	± 1.5	+111.1 -92.8	+141.7 -127.8

Table 9.12: Extracted number of NC and background events for an ES and CC unconstrained fit for events with reconstructed radius less than 476cm. The systematic uncertainties from energy scale (E), energy resolution (σ_E), β_{14} scale (β_{14}), β_{14} resolution ($\sigma_{\beta_{14}}$), radial scale (R), radial resolution (σ_R), and angular resolution (σ_{Ang}). The total systematic uncertainty (σ_{sys}) and total uncertainty (σ_{total}) are given in the last 2 columns.

	Fit	E	σ_E	β_{14}	$\sigma_{\beta_{14}}$	R	σ_R	σ_{Ang}	σ_{sys}	σ_{total}
nc	2918.0 ± 89.4	+1.4 -1.9	+1.6 -1.6	+2.7 -5.0	+1.3 -1.3	+0.0 -0.8	+0.8 -0.8	± 0.2	+3.7 -5.8	+5.3 -7.0
Bi	548.9 ± 113.3	+14.0 -5.2	+28.3 -28.3	+17.5 -0.0	+12.4 -12.4	+3.9 -0.0	+2.6 -2.6	± 3.0	+38.5 -31.5	+43.7 -37.7
Bi H2O	113.4 ± 26.2	+5.4 -21.8	+0.9 -0.9	+0.4 -5.3	+16.5 -16.5	+6.1 -19.6	+7.7 -7.7	± 0.2	+20.0 -35.0	+30.6 -41.9
Bi AV	84.6 ± 31.3	+0.0 -32.3	+32.1 -0.9	+25.2 -50.8	+14.2 -14.2	+5.4 -11.8	+7.1 -7.1	± 0.7	+44.1 -71.0	+57.5 -80.1
Tl	239.1 ± 120.0	+0.0 -17.6	+26.8 -26.8	+21.8 -0.0	+23.1 -23.1	+1.0 -3.4	+3.7 -3.7	± 0.5	+41.7 -39.8	+65.3 -64.1
Tl H2O	28.1 ± 31.4	+116.6 -0.0	+59.9 -59.9	+55.8 -48.6	+100.0 -100.0	+66.4 -0.0	+26.2 -26.2	± 0.6	+188.1 -129.0	+218.8 -170.6
Tl AV	0.0 ± 34.6	-	-	-	-	-	-	-	-	-
Na24	157.1 ± 98.5	+31.6 -0.0	+9.6 -9.6	+0.0 -26.3	+16.8 -16.8	+3.7 -4.0	+2.0 -2.0	± 1.0	+37.3 -33.0	+73.0 -70.9
Pmt	58.2 ± 15.4	+8.5 -5.6	+46.7 -46.7	+0.0 -7.8	+18.4 -18.4	+14.2 -0.0	+15.0 -15.0	± 0.1	+54.9 -53.3	+61.0 -59.5
Extn	0.0 ± 7.0	-	-	-	-	-	-	-	-	-

Table 9.13: Extracted number of NC and background events for an ES and CC unconstrained fit for events with reconstructed radius less than 550cm. The systematic uncertainties from energy scale (E), energy resolution (σ_E), β_{14} scale (β_{14}), β_{14} resolution ($\sigma_{\beta_{14}}$), radial scale (R), radial resolution (σ_R), and angular resolution (σ_{Ang}). The total systematic uncertainty (σ_{sys}) and total uncertainty (σ_{total}) are given in the last 2 columns. For the backgrounds where the fit results are equivalent to 0 the systematics uncertainties as a percent are meaningless and are therefore not given.

Chapter 10

Physics Interpretation

The number of neutrino events have been extracted for the CC, ES, and NC signals above a kinetic energy threshold of 4.0MeV in the salt phase of SNO. This is significantly lower than the already published salt analysis threshold of 5.5MeV [1]. To extract the neutrino signals down to the 4MeV energy threshold the number of internal and external backgrounds are extracted along with the neutrino signals. This has provided a tight constraint on the number of background events. The extracted CC and NC fluxes have smaller uncertainties than the previously published results. The CC flux is extracted from an energy dependent fiducial volume analysis. This is done to minimize the radioactive background to CC signal ratio for every energy bin.

10.1 ^8B Energy Shape Constrained Fits

The lowest uncertainties on the neutrino fluxes are achieved by doing a ^8B energy shape constrained fit on the neutrino data. The energy shape can then be used as an additional constraint on the CC and ES extraction. The NC number by itself provides

a direct test of the standard solar model calculation for the neutrino flux. While the shape constrained fit provides the smallest uncertainties on the extracted fluxes and is useful for testing the no-oscillation hypothesis the fit results do not provide any other physics information. The energy shape constrained fits have been performed with a 476cm, 550cm, and 576cm radial acceptance region. The extracted number of CC, NC, and ES events obtained from the constrained fit are given in tables 10.1 and 10.3. The fits are done down to an energy threshold of 4MeV, the same as for the unconstrained fits. For the results published in [1] the constrained signal extraction was done for an energy threshold of 5.5MeV and a radial region of 550cm. The results presented here have a smaller statistical and systematic uncertainty than the results in [1]. The lower energy threshold means more events are in the data sample and therefore the extracted numbers have better statistical precision. Since the backgrounds are fitted for along with the signals down to 4MeV the number of background events are better constrained in the neutrino signal window which results in a smaller systematic uncertainty. The dominant systematic uncertainties on the CC and NC numbers are the uncertainties associated with the energy response and the β_{14} parameter. These were described in sections 9.1 and 9.2. The dominant systematic uncertainty on the extracted number of ES events is the uncertainty that arises from the angular resolution. The angular resolution uncertainty was described in section 9.3.

It is more useful to express the numbers in tables 10.1 and 10.3 in terms of absolute neutrino fluxes. In this way the the CC and NC fluxes can be compared to determine the oscillation angle and the NC flux can be used to check the SSM prediction.

Signal	476cm volume	550cm volume
CC	$1765 \pm 3.8 \%$ (stat) $^{+3.6}_{-3.6} \%$ (syst)	$2627 \pm 3.1 \%$ (stat) $^{+3.6}_{-4.3} \%$ (syst)
NC	$1998 \pm 4.2 \%$ (stat) $^{+4.0}_{-4.3} \%$ (syst)	$2900 \pm 3.4 \%$ (stat) $^{+5.8}_{-3.5} \%$ (syst)
ES	$273 \pm 10 \%$ (stat) $^{+14.6}_{-13.1} \%$ (syst)	$461 \pm 8.4 \%$ (stat) $^{+9.2}_{-7.1} \%$ (syst)

Table 10.1: Extracted number of CC, ES, and NC events after performing a ^8B energy shape constrained fit on the salt neutrino data. Shown are the extracted number for an analysis volume of 476cm, 550cm. The uncertainties on the numbers are given as a percent.

Signal	576cm volume
CC	$2939 \pm 3.0 \%$ (stat) $^{+4.0}_{-4.2} \%$ (syst)
NC	$3384 \pm 3.0 \%$ (stat) $^{+4.7}_{-4.0} \%$ (syst)
ES	$536 \pm 7.8 \%$ (stat) $^{+9.1}_{-8.0} \%$ (syst)

Table 10.2: Extracted number of CC, ES, and NC events after performing a ^8B energy shape constrained fit on the salt neutrino data. Shown are the extracted number for an analysis volume of 576cm. The uncertainties on the numbers are given as a percent.

Signal	Flux ($\times 10^6 \text{cm}^{-2} \text{sec}^{-1}$)
CC	1.62 $^{+0.05}_{-0.05}$ (stat) $^{+0.06}_{-0.07}$ (syst)
NC	4.82 $^{+0.16}_{-0.16}$ (stat) $^{+0.30}_{-0.19}$ (syst)
ES	2.63 $^{+0.22}_{-0.22}$ (stat) $^{+0.24}_{-0.19}$ (syst)

Table 10.3: Absolute neutrino fluxes for the CC, ES, and NC signals for an constrained ^8B energy shape fit out to a radius of 550cm and above an energy threshold of 4MeV.

10.2 ^8B Energy Shape Unconstrained Fit Results

While the ^8B energy shape constrained fit gives an overall smaller uncertainty in the extracted neutrino fluxes, the extracted fluxes are not physical since neutrinos go through spectral distortion as they pass through the sun. Therefore a more realistic measurement of the total flux is through the unconstrained signal extraction. The unconstrained neutrino signal is extracted in each 0.5MeV bin between 4MeV and 13MeV for the CC and ES neutrino signals. To get the total CC and ES unconstrained flux the extracted number of CC and ES events are summed from each of the 0.5MeV bins. Table 10.4 shows the total number of fitted neutrino signal events from the unconstrained fit. The statistical uncertainty on the extracted numbers does not change much compared to the constrained fit however the systematic uncertainties on the CC and ES neutrino events are higher for the unconstrained fit. For the NC signal the systematic uncertainty is similar to the constrained fit since the energy shape of the NC signal is still constrained in the unconstrained fit.

Signal	550cm volume
CC	$2565 \pm 3.2 \%$ (stat) $_{-16.1}^{+11.5} \%$ (syst)
NC	$2912 \pm 3.3 \%$ (stat) $_{-6.7}^{+5.9} \%$ (syst)
ES	$479 \pm 8.1 \%$ (stat) $_{-11.3}^{+10.6} \%$ (syst)

Table 10.4: Extracted number of CC, ES, and NC events after performing a ^8B energy shape unconstrained fit on the salt neutrino data. Shown are the extracted number for an analysis volume of 550cm. The uncertainties on the numbers are given as a percent.

Table 10.5 summarizes the absolute fluxes from the three neutrino signals derived from the unconstrained fit. Both the energy and unconstrained fits results are in agreement with the previously published result in [1]. The previously published

energy constrained fit fluxes are 1.72 for CC, 4.81 for NC, and 2.34 for ES. The unconstrained fit results were 1.68 for CC, 4.94 for NC, and 2.35 for ES. The numbers are in terms of $10^6\text{cm}^{-2}\text{sec}^{-1}$.

Signal	Flux ($\times 10^6\text{cm}^{-2}\text{sec}^{-1}$)	
CC	1.58 $^{+0.05}_{-0.05}$ (stat)	$^{+0.18}_{-0.25}$ (syst)
NC	4.84 $^{+0.16}_{-0.16}$ (stat)	$^{+0.29}_{-0.32}$ (syst)
ES	2.73 $^{+0.22}_{-0.22}$ (stat)	$^{+0.29}_{-0.31}$ (syst)

Table 10.5: Absolute neutrino fluxes for the CC, ES, and NC signals for an unconstrained ^8B energy shape fit out to a radius of 550cm and above an energy threshold of 4MeV.

The extracted neutrino fluxes for a signal extraction out to a radius of 576cm are given in table 10.6. The larger systematic uncertainty on the CC flux for the 576cm fit is due to the increase in external backgrounds at higher radius.

Signal	Flux ($\times 10^6\text{cm}^{-2}\text{sec}^{-1}$)	
CC	1.58 $^{+0.08}_{-0.08}$ (stat)	$^{+0.20}_{-0.32}$ (syst)
NC	5.23 $^{+0.15}_{-0.15}$ (stat)	$^{+0.22}_{-0.48}$ (syst)
ES	2.75 $^{+0.23}_{-0.23}$ (stat)	$^{+0.25}_{-0.26}$ (syst)

Table 10.6: Absolute neutrino fluxes for the CC, ES, and NC signals for an unconstrained ^8B energy shape fit out to a radius of 576cm and above an energy threshold of 4MeV.

10.2.1 CC flux with an Energy Dependent Fiducial Volume

We can improve the precision of the CC flux measurement by employing the energy dependent fiducial volume method, where for a given energy threshold a radial region is chosen to maximize the signal to background ratio. For a lower energy threshold a

smaller volume is chosen to remove background events from external radioactivity. At a higher threshold, the volume can be increased. The CC flux has been determined at various radial and energy thresholds and then a weighted average is taken to get a combined flux. The radial regions used are outlined by panel (a) of figure 10.2, and are summarized in table 10.7. The CC flux determined from the energy dependent fiducial volume method has a significantly lower uncertainty than the CC flux determined from the previous analysis above 5.5MeV. Taking a weighted average

Radius (cm)	Energy range (MeV)
476	4.0-5.0
536	5.0-6.0
550	6.0-8.0
576	8.0-13.0

Table 10.7: Radial regions used for CC flux extraction for various energy bins. The radial regions are chosen to give the best CC signal to radioactive background ratio for the given energy bins.

of the CC flux from all the radial-energy regions gives

$$\Phi_{CC} = 1.60_{-0.04}^{+0.04} \text{ (stat)} \text{ }_{-0.06}^{+0.06} \text{ (syst)} \times 10^6 \text{cm}^{-2} \text{sec}^{-1}.$$

The neutrino mixing angle is directly related to the electron neutrino survival probability. Therefore it is useful to calculate the CC/NC flux ratio, which is the ratio of the electron type neutrino flux to the flux of all active neutrinos. Equation 10-2 gives the CC/NC flux ratio calculated for the unconstrained fit above 4MeV and for the fit above 5.5MeV done in [1]. The CC/NC ratios derived here are in agreement with those published.

$$\frac{\Phi_{CC}}{\Phi_{NC}} (4\text{MeV}) = 0.331_{-0.014}^{+0.014} \text{ (stat)} \text{ }_{-0.025}^{+0.024} \text{ (syst)}, \quad (10-1)$$

$$\frac{\Phi_{CC}}{\Phi_{NC}} (5.5\text{MeV}) = 0.340^{+0.023}_{-0.023} (\text{stat})^{+0.029}_{-0.031} (\text{syst}). \quad (10-2)$$

Table 10.8 compares the uncertainties on the extracted fluxes for the 4MeV analysis done here with the 5.5MeV threshold analysis from [1]. Table 10.9 compares the

	4MeV uncertainty (%)	5.5MeV uncertainty (%)
Φ_{CC}	+4.6 -4.4	+5.9 -6.4
Φ_{NC}	+6.8 -7.4	+8.9 -8.2
Φ_{ES}	+12.3 -12.6	+11.3 -11.3

Table 10.8: Uncertainties on the extracted neutrino fluxes for the 4MeV analysis done here and for the analysis done in [1].

uncertainties on the CC/NC flux ratios for the analysis done here and for the previous 5.5MeV threshold analysis.

	uncertainty on CC/NC (%)
4MeV analysis	+8.4 -8.7
5.5MeV analysis	+10.9 -11.4

Table 10.9: Total uncertainties on the CC/NC flux ratios for the 4MeV analysis and the analysis done in [1].

10.2.2 Comparison with the Standard Solar Model

The most recent theoretical calculation of the SSM ^8B neutrino flux from the late John Bahcall was $5.79(1\pm 0.23)$ [2]. Even though this number is considerably higher than the measured NC flux summarized in tables 10.5, 10.6 and 10.3, the measured values fall within the large 23% theoretical uncertainty.

10.3 The CC Energy Spectrum

The extracted CC energy spectrum above an outgoing electron energy of 4MeV is very interesting in terms of testing the predicted effect of the MSW mechanism on the neutrino energy spectrum. The MSW effect predicts an upturn in the neutrino survival probability at energies lower than the already published SNO energy threshold of 5.5MeV. The upturn is even more defined at energies below 4MeV but the SNO radioactive background levels overwhelm the neutrino signal at lower energies. Future neutrino experiments plan to detect the pep and pp neutrinos to probe the transition region between MSW and vacuum oscillations. Figure 2.2 in chapter 2 shows the expected electron neutrino survival probability as function of energy predicted by the MSW effect. There is a strong upturn in the survival probability at energies below the already published analysis threshold. The CC energy spectrum presented in this thesis is extracted down to an energy threshold of 4MeV. There is no apparent upturn observed in the extracted spectrum. It has been proposed that one of the ways to explain the lack of the upturn in the survival probability is through non standard neutrino-matter interactions (NSI). These non-standard interactions could possibly take the form of neutrinos interacting with quarks and not just electrons as they pass through matter. This would result in a different MSW type effect where the neutrino mixing is dependent on the chemical composition of the medium and not just the electron density [17]. Figure 10.1 shows the survival probabilities for the best-fit point for the standard LMA solution, labeled LMA-1 in the figure, and for the LMA solution including non-standard interactions, labeled LMA-0. The curves represent the survival probabilities averaged over production region inside the sun for the ^8B and pep components of the neutrino fluxes. While the standard LMA-1

solution shows an upturn in the survival probability at energies below the SNO energy range the non-standard LMA-0 solution shows a dip in the survival probability in this region.

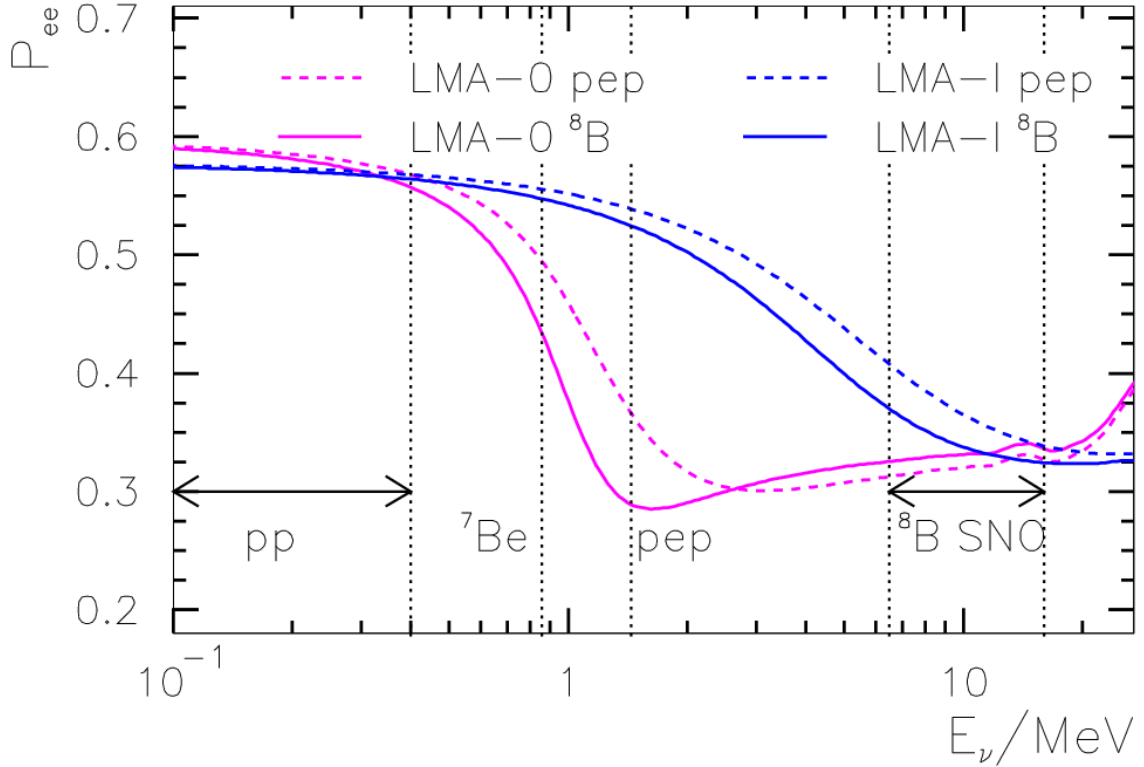


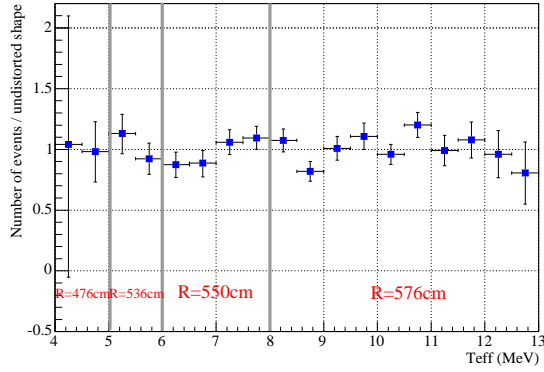
Figure 10.1: Electron neutrino survival probabilities for the best fit LMA-0 and LMA-1 points. The LMA-0 solutions represents the MSW effect with non-standard interactions included. LMA-1 is the standard MSW effect solution.

10.3.1 Fit to the Charge Current Energy Spectrum

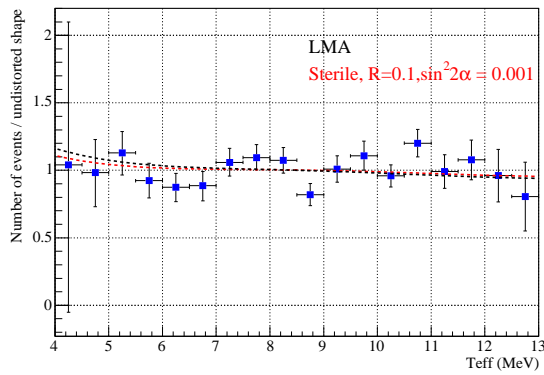
Another possible mechanism that might cancel the upturn predicted by the MSW effect is that the active neutrinos can oscillate into a non-interacting sterile neutrino. The sterile neutrino mixing was described in section 2.2.1. The SNO salt and pure

D₂O phase data was fitted to a neutrino survival probability determined from introducing a small sterile mixing angle [16]. The fit was shown in figure 2.3 and is for the previously published SNO energy threshold of 5.5MeV. For the analysis in this thesis, a similar fit was done for the salt phase data down to an energy threshold of 4MeV. The extracted CC energy spectra were combined from the fits at various radial acceptance regions, shown in 9.13, to get the extracted number of CC events for every 0.5MeV bin with the lowest possible uncertainty. At the largest radial acceptance region of 576cm for example, the extracted number of CC events in the lowest energy bin of 4 to 4.5MeV would have the smallest statistical uncertainty but the largest systematic uncertainty due to the contamination of external radioactive backgrounds. The extracted number of CC events in each energy bin were chosen from a radial region that minimized the combined statistical and systematic uncertainty for that given energy bin. The combined CC energy spectrum was then divided by the predicted CC energy spectrum assuming no neutrino oscillations. If there is no spectral distortion then the resultant curve would be a flat line. The MSW effect predicts an upturn in this curve at lower energies. Figure 10.2 shows the ratio of the extracted number of CC events in every 0.5MeV energy bin between 4 and 14MeV to the number predicted by an undistorted ⁸B energy spectrum. Indicated in the figure are also the radial cuts used for the various energy regions. The extracted data is compared to the SNO best fit LMA solution of $\Delta m^2 = 8.0 \times 10^{-5}$ and $\theta = 33.9$ degrees. It is also fitted to the LMA solution with a small sterile mixing angle of $\sin^2(2\alpha) = 0.001$ and a ratio of the sterile mass squared difference to the active neutrino mass squared difference of $R_\Delta = 0.1$. Both curves fit well to the data, with the sterile mixing survival probability giving a slightly better fit. For the LMA fit the χ^2 is 18.9 for 17 degrees of freedom and for the sterile fit it is 17.6 for 17 degrees

of freedom. This is not significant enough to disprove the pure LMA solution or to support sterile neutrino mixing.



(a)



(b)

Figure 10.2: The ratio of the extracted CC energy spectrum to the ^8B energy spectrum with no neutrino oscillations. Panel (a) indicates the radial regions used to get the lowest uncertainties on the extracted CC flux for the various energy bins. Panel (b) shows the data points from panel (a) fitted to the survival probability predicted by the standard LMA solution to the MSW effect and to the predicted survival probability if a small sterile mixing angle is included to the LMA solution.

Chapter 11

Conclusion

The neutrino data from the salt phase of SNO has been analyzed. As part of the salt phase analysis the detection efficiency for neutrons produced by the NC neutrino interaction has been determined. The detection efficiency was determined through a calibration program where a ^{252}Cf source was deployed at various radial positions throughout the D_2O volume. For a 5.5MeV energy threshold and a fiducial volume of 550cm the neutron detection efficiency has been determined to be $(40.7 \pm 0.5_{-0.8}^{+0.9})\%$. This is a factor of ~ 3 higher than the pure D_2O phase detection efficiency measurement.

The CC, NC, and ES neutrino signals in SNO have been extracted down to a kinetic energy threshold of 4MeV. The previously published results are for an energy threshold of 5.5MeV. In going lower in energy threshold, the internal and external radioactive backgrounds become significant. To account for the radioactive backgrounds the backgrounds are extracted along with the neutrino signals in a maximum likelihood signal extraction. To minimize uncertainties on the extracted CC flux an energy dependent fiducial volume is used that maximizes the CC signal to radioactive

background ratio. The absolute neutrino fluxes above an energy threshold of 4MeV are

Signal	Flux ($\times 10^6 \text{cm}^{-2} \text{sec}^{-1}$)	
CC	1.60 $^{+0.04}_{-0.04}$ (stat)	$^{+0.06}_{-0.06}$ (syst)
NC	4.84 $^{+0.16}_{-0.16}$ (stat)	$^{+0.29}_{-0.32}$ (syst)
ES	2.75 $^{+0.23}_{-0.23}$ (stat)	$^{+0.25}_{-0.26}$ (syst)

These values are in agreement with the fluxes published in [1] for a 5.5MeV energy threshold. The NC flux, which is a measure of total active neutrino flux from the sun, is in agreement with the latest SSM prediction of $5.79(1\pm 0.23)$ [2]. The uncertainties on the extracted NC and CC fluxes are smaller than the published results. The uncertainties compared to the published results are given below.

	uncertainties presented here (%)	uncertainties from [1] (%)
Φ_{CC}	$^{+4.6}_{-4.4}$	$^{+5.9}_{-6.4}$
Φ_{NC}	$^{+6.8}_{-7.4}$	$^{+8.9}_{-8.2}$
Φ_{ES}	$^{+12.3}_{-12.6}$	$^{+11.3}_{-11.3}$

The ratios of electron type neutrino flux to the total active neutrino flux for the results presented here and for the published results are

$$\frac{\Phi_{CC}}{\Phi_{NC}} (4\text{MeV}) = 0.331 \text{ } ^{+0.014}_{-0.014} \text{ (stat)} \text{ } ^{+0.024}_{-0.025} \text{ (syst)},$$

$$\frac{\Phi_{CC}}{\Phi_{NC}} (5.5\text{MeV}) = 0.340 \text{ } ^{+0.023}_{-0.023} \text{ (stat)} \text{ } ^{+0.029}_{-0.031} \text{ (syst)}.$$

Again, in agreement with the the previously published values. A direct comparison of the total uncertainty on the CC/NC ratio derived here with the published ratio is shown below.

	uncertainty on CC/NC (%)
4MeV analysis	+8.4 -8.7
5.5MeV analysis	+10.9 -11.4

The CC energy spectrum has been extracted down to a kinetic energy of 4MeV and compared to the LMA prediction for spectral distortion. To minimize uncertainties on the extracted spectrum an energy dependent radial region was used. This was done to minimize the external radioactive background to signal ratio in each energy bin. Due to the large uncertainties in the extracted CC spectrum at the low energy bins the predicted LMA distortion was not observed. The extracted CC spectrum may however exclude some non-standard neutrino interaction theories which predict a large spectral distortion.

Bibliography

- [1] SNO Collaboration. Electron energy spectra, fluxes, and day-night asymmetries of ^8B solar neutrinos from the 391-day salt phase SNO data set. *Phys. Rev. C*, 72(055502), 2005.
- [2] John N. Bahcall and M. H. Pinsonneault. *Phys. Rev. Lett.*, 92:121301, 2004.
- [3] John N. Bahcall. *Neutrino Astrophysics*. Cambridge University Press, Cambridge, 1989.
- [4] B. T. Cleveland et al. *Astrophys. J.*, 496:505–526, 1998.
- [5] John N. Bahcall, M. H. Pinsonneault, and Sarbani Basu. *Astrophys. J.*, 555:990–1012, 2001.
- [6] B. Pontecorvo. *Sov. Phys. JETP*, 6:172, 1958.
- [7] Samoil M. Bilenky and B. Pontecorvo. *Phys. Rept.*, 41:225–261, 1978.
- [8] L. Wolfenstein. *Phys. Rev.*, D17:2369, 1978.
- [9] S.P. Mikheyev and A. Yu. Smirnov. *Nuovo Cimento*, 9C(17), 1986.
- [10] Y. Fukuda et al. *Phys. Rev. Lett.*, 81:1562–1567, 1998.

- [11] SNO Collaboration. Measurement of charged current interactions produced by ^8B solar neutrinos at the Sudbury Neutrino Observatory. *Phys. Rev. Lett.*, 87(071301), 2001.
- [12] SNO Collaboration. Direct evidence for neutrino flavor transformation from neutral-current interactions in the Sudbury Neutrino Observatory. *Phys. Rev. Lett.*, 89(011301), 2002.
- [13] SNO Collaboration. Measurement of the total active ^8B solar neutrino flux at the Sudbury Neutrino Observatory with enhanced neutral current sensitivity. *Phys. Rev. Lett.*, 92(181301), 2004.
- [14] Simon Peter Rosen and James M. Gelb. *Phys. Rev.*, D34:969, 1986.
- [15] A. J. Baltz and J. Weneser. *Phys. Rev.*, D37:3364, 1988.
- [16] P. C. de Holanda and A. Yu. Smirnov. *Phys. Rev.*, D69:113002, 2004.
- [17] Alexander Friedland, Cecilia Lunardini, and Carlos Pena-Garay. *Phys. Lett.*, B594:347, 2004.
- [18] J. Boger et al. *Nucl. Instrum. Meth.*, A449:172–207, 2000.
- [19] B.G. Nickel and J.J. Simpson. The efficiency of neutrons in the SNO detector. SNO Internal Report, 2000.
- [20] S. Croft. *Nucl. Instrum. Meth.*, A281:103, 1989.
- [21] M. Dragowski and A Hime. Neutron response and efficiency for the pure D_2O phase. SNO internal report, 2001.

- [22] B.G. Nickel and H. Labranche. Time series analysis of the AmBe data. SNO Internal Report, 2003.
- [23] T.C. Anderson et al. *Nucl. Instrum. Meth.*, A501:399–417, 2003.
- [24] The SNO low energy background group. Low energy background in the salt phase of the SNO experiment. SNO Internal Report, 2003.
- [25] M. Boulay, J. Formaggio, and A. Hallin et al. Other background sources in the salt phase of SNO. SNO Internal Report, 2003.
- [26] Hamish Robertson. Coincidence data from (α,n) reactions in the D₂O and salt phases. SNO Internal Report, 2003.
- [27] Mark G. Boulay. External neutrons. SNO Internal Report, 2003.
- [28] C.E. Ortiz et al. Shape of the ⁸B alpha and neutrino spectra. *Phys. Rev. Lett.*, 85(2909), 2000.
- [29] M. Butler, J.W. Chen, and X. Kong. Neutrino-deuteron scattering in effective field theory at next-to-next-to-leading order. *Phys. Rev. C*, 63(035501), 2001.
- [30] Mark Boulay. *Direct Evidence for the Weak Flavour Mixing with the Sudbury Neutrino Observatory*. PhD thesis, Queens' University, Kingston, Ontario, Canada, 2001.
- [31] Louis Lyons. *Statistics for Nuclear and Particle Physics*. Cambridge University Press, Cambridge, 1992.

- [32] Christopher James Jillings. *The Electron Scattering Reaction in the Sudbury Neutrino Observatory*. PhD thesis, Queens' University, Kingston, Ontario, Canada, 1999.